# FINITE-TIME EULER SINGULARITIES: A LAGRANGIAN PERSPECTIVE

DISSERTATION

zur
Erlangung des Grades eines
»Doktors der Naturwissenschaften«
in der Fakultät für Physik und Astronomie
der Ruhr-Universität Bochum

von
TOBIAS GRAFKE

aus
WUPPERTAL

BOCHUM 2012

# Contents

# 1. Introduction

Modern physics concerns itself with intricate, overwhelming problems: Grand unification and string theory, Higgs bosons and the origin of mass or dark matter and the formation of galaxies. All these topics have in common being far from everyday experience and residing at energy- and time-scales beyond intuition. On the other hand, physics immediately surrounding us, especially phenomena of tangible experience, are commonly believed to be reasonably free of physical mystery and of little interest to modern physics.

Classical fluid dynamics remains an astonishing exception from this rule. This is quite surprising, since its vast applications concern humanity since its dawn and the mathematical groundwork has been laid centuries ago. Ultimately a consequence of the underlying molecular interaction, continuous fluid dynamics arises as emergent behavior in a wide range of situations and are able to describe many physical phenomena on all length scales: combustion and turbulent mixing, aviation, oceanic flows, weather prediction, climate change, solar activity and space weather, planet formation, space nebulae or galaxy formation. Beyond technical applications, the underlying model equations are a paramount example for the complexity of dynamics in nonlinear partial differential equations, with the most prominent example of the *incompressible Navier-Stokes equations*. For now more than two centuries, these equations have withstood the minds of mathematicians and physicists alike: The derivation of the nature of turbulence from the equations, as well as the global existence of smooth solutions is not known to date. The huge mathematical difficulties concerning the latter problem were recognized by its elevation to the status of "Millennium Prize Problem" by the Clay Mathematics Institute (see the official problem description by Fefferman [35], or review articles e.g. by Doering [32], Ladyzhenskaya [69]). A proof of existence of global regular solutions to the Navier-Stokes equation is believed to entail the development of completely new methods for the analysis of partial differential equations. The absence of mathematical certainty for the Navier-Stokes equations may seem to leave the physicist in a somewhat embarrassing position: The equation is known and well tested in application, but the existence of solutions is unclear in relevant cases.

Yet, the actual impact of a supposed breakdown of solutions for the Navier-Stokes equations on physics of fluids is smaller than one might expect and appears like a mere technical detail on second thought. Singularities in the Navier-Stokes equation would, if existent, appear on very small scales. Obvi-

ously, continuum mechanics do not hold on these smallest scales and the breakdown of the model equation would appear in a regime in which the model does not describe reality anyhow. Furthermore, the nature of supposed singularities for the Navier-Stokes equation is proven to be unphysical in nature, as it requires the existence of infinite momentum. Without external forcing, from smooth initial conditions and in the presence of friction, the occurrence of infinite momentum is impossible to justify physically. The impact of singularities is additionally limited by the fact that the space-time dimension of the singular region is proven to be less than one for the Navier-Stokes equations [12].

In the inviscid limit, the situation is quite the opposite. The *incompressible Euler equations* for ideal fluids appear to be of little physical significance, since friction is the dominating process on small scales in most applications. The ignorance regarding existence of global solutions is even larger for the inviscid case: The notion of weak solutions, which are well established for the Navier-Stokes equations since Leray [71], is unknown for the three-dimensional Euler equations. Nevertheless, the formation of finite-time Euler singularities significantly concerns our understanding of (viscid) fluid dynamics. Euler singularities, if existent, would coincide with the development of large gradients in the velocity field. Since no friction is limiting the increase in velocity gradients, infinite momentum is not mandatory for a blowup of the Euler equations. The inviscid limit is, therefore, not only a mere description of ideal fluids, but explores the possibility of inherent dynamical processes beyond friction, that limit the transition to smaller and smaller scales. This has immediate implications on the existence of a cut-off velocity in high Reynolds-number Navier-Stokes flows, leading to the slightly exaggerated question, quoting Constantin [25]: "Do we need Schrödinger's equations to calculate the flow around a moving car? Or to predict tomorrow's weather?" For that reason, the problem of singularities for the Euler equations is of far greater importance to the physical understanding of fluids than the analogous problem for the Navier-Stokes equations.

A similar argument is valid for turbulence. Turbulent flows are omnipresent. Turbulence may even be seen as the generic state of incompressible fluids. Nevertheless, analytic understanding of turbulence has yet to bridge the gap between the partial differential equation and the statistical properties obtained from experiments or numerical simulations. Today's phenomenological description of turbulence (e.g. Frisch [36], She and Lévêque [87]), which is built on the basis of the celebrated theory by Kolmogorov [64, 65, 66], contains as a central point that, in the limit of vanishing viscosity, energy dissipation has to stay finite. This behavior could be explained by the formation of finite-time Euler singularities, as implied by Onsager's conjecture [79]. For three-dimensional incompressible flow, non-conservation of energy might be caused not only by viscosity but by missing regularity in the velocity field. Energy dissipation might occur, if the Hölder continuity exponent is smaller than $1/3$ for the velocity field. This con-

jecture was later proven in terms of Besov spaces instead of Hölder continuity by Cheskidov et al. [15], Constantin et al. [27]. As a consequence, a mathematical description of turbulence might be possible in terms of weak solutions for the Euler equations, if smooth solutions gain enough roughness in finite time. Therefore, insight into the formation of finite-time singularities for the Euler equations could uncover a mechanism essential for the understanding of viscous turbulence.

The search for finite-time singularities of the Euler equations has resulted in extensive literature, with many analytical results being relatively young. Especially the advent of scientific computing has given research a new direction: Reports of numerical evidence supporting or denying the existence of finite-time singularities for the Euler equations are numerous (see e.g. Gibbon [39] for a compiled list).

As a now classical result, the blowup criterion of Beale et al. [3] connects the existence of solutions for the incompressible Euler equations in three dimensions to the critical accumulation of vorticity. More recently, geometric analysis of the flow [28, 29] has helped increasing insight into the process of vorticity growth. Among these geometric blowup criteria, theorems developed by Deng et al. [30] may be seen as the first to be suitable for verification by direct numerical simulations. Exactly this was accomplished and will be presented in this work.

The overall idea is stated as follows: Given the results of analytical considerations and the experience gained from numerical simulation of the Euler equations, certain scenarios are known to be compatible with the analytic requirements of a finite-time blowup, namely the global notion of self-similar collapse to a point and the local process of vorticity accumulation by vorticity-strain coupling. It has been tried in the past to construct explicit initial conditions exploiting these scenarios to obtain numerical evidence for or against a finite-time singularity, with surprisingly inconsistent results. The major reason for this ambiguity is the critical dependence on extrapolation, which renders the identification of singular versus near-singular behavior next to impossible by numerical means. The hopes are high that the situation is less vague when considering geometric properties of the flow, as mentioned above. This work will present the application of such geometric criteria to numerical data to sharpen the distinction between singular and near-singular flow evolution.

## 1.1. Outline

This work is organized as follows:

Physical motivation and basic properties of the Euler equations are given in chapter 2. This includes the presentation of the basic interaction of vorticity and strain, conserved quantities and definition of terms necessary for the geometric

analysis of Euler flows, such as the notion of vortex lines and their behavior.

Chapter 3 gives an overview of the numerical algorithms used throughout this work. The framework *racoon* is introduced, with emphasis on its ability to utilize adaptively refined meshes and its high scalability on massively parallel computers. The numerical scheme for integrating the Euler equations is presented and compared against competing discretizations. This defines the groundwork for conducting the presented results for simulations of the Euler equations with high resolutions.

A presentation of analytic results regarding the formation of finite-time Euler singularities is given in chapter 4. Well-known methods for the analysis of PDEs are used to put into perspective the classical result of Bealo-Kato-Majda. Based on these results, geometric blowup criteria are introduced and the geometric analysis of the flow is illustrated. The focus here is on the stretching of vortex lines and its connection to accumulation of vorticity, as well as the Lagrangian evolution of vortex line segments. This chapter defines the analytical criteria that will be tested numerically in the following chapter.

Chapter 5 deals with the numerical simulation of possible finite-time Euler singularities. First, scenarios for the formation of singularities are introduced and necessary interactions are presented. Using these results, promising initial conditions for Euler flows are justified and compared, resulting in a candidate for subsequent simulations. The simulations are presented and analyzed in regard to the geometrical blowup criteria. These results will serve as evidence against the formation of a finite-time blowup of the considered class of flows.

In chapter 6, the obtained results will be summarized and a conclusion will be given.

# 2. The Euler equations

As defined by Batchelor [2], fluid dynamics deals with the behavior of liquids and gases in motion. Assuming incompressibility, the distinction between these two groups lies merely in the numerical value of quantities, most importantly the mass density. The difference in their dynamical behavior is therefore not of fundamental nature from the theorist's point of view. It is thus common to refer to both groups with the general term *fluid*.

The dynamic evolution of fluids can be understood as a direct consequence of fundamental conservation laws without putting emphasis on the individual substance of the fluid. This approach will be taken in section 2.1 to give a summarized motivation for the *Euler equations* (and to some extent for the *Navier-Stokes equations*). In addition to this heuristic point of view, one can also perceive a quantity of matter in fluidic state as a collection of individual particles. The usual approach then is to consider the first few moments of a kinetic description (like the *Boltzmann equation*) and passing to the continuous limit with some additional assumptions to arrive at the *Euler-* or *Navier-Stokes equations*.

Even though every fluid is composed of interacting molecules, and their dynamics ultimately are a consequence of their mutual collisions and reaction to outer forces, the continuous description offers a good approximation to the measured behavior (and in many cases is the only viable solution). Nevertheless, the underlying assumption of continuity has to be kept in mind and the model equation may no longer approximate nature as soon as the assumption is no longer met. This is of particular importance when considering the physical consequences of singular or near-singular evolution of the model equations.

## 2.1. Physical Motivation

In the continuous approach we consider the fluid's variables to be scalar- or vector-valued fields in a $d$-dimensional region of space (the domain) $\Omega \subset \mathbb{R}^d$. For this thesis, $d$ takes the values of 2 or 3, with $d = 3$ being the relevant case. Let $\mathbf{u}(\mathbf{x}, t)$ be the fluid velocity, $\rho(\mathbf{x}, t)$ the density and $p(\mathbf{x}, t)$ the pressure field. Now consider the fluid contained in an infinitesimal fluid element $dV$ at time $t$ located at $\mathbf{x} \in \Omega$. It has the mass $dm = \rho(\mathbf{x}, t)dV$ and the momentum $d\left(m\mathbf{u}(\mathbf{x}, t)\right)$.
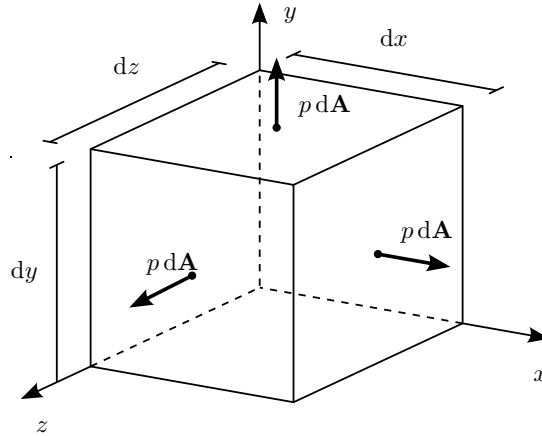
**Figure 2.1.**: An infinitesimal fluid element of Volume $dV = dxdydz$. The net force on the element is given as the pressure difference in normal direction across the volume, $d\mathbf{F} = \nabla p\, dV$

As the system evolves, we want to track the evolution of these quantities in time. The change of a quantity along a fluid elements' path is calculated via the *convective* or *material* derivative

$$\frac{D}{Dt} = \frac{\partial}{\partial t} + \mathbf{u}(\mathbf{x}, t) \cdot \nabla \ . \tag{2.1}$$

The equations of motion for a fluid are a consequence of two fundamental conservation laws: The conservation of mass and the conservation of momentum. For conservation of mass we require that the mass of a fluid element is fixed in time,

$$\frac{D\,dm}{Dt} = 0 \ . \tag{2.2}$$

Without further assumptions, the volume of the fluid element may change in time:

$$\frac{D\,dV}{Dt} = (\nabla \cdot \mathbf{u})dV \ . \tag{2.3}$$

Taking these two in combination, we get the evolution equation for the fluid density as

$$\frac{D\rho}{Dt} = \frac{D}{Dt}\frac{dm}{dV} = -\frac{dm}{(dV)^2}\frac{D\,dV}{Dt} = -\rho\nabla \cdot \mathbf{u} \tag{2.4}$$

which in turn leads to the *continuity equation*

$$\frac{\partial \rho}{\partial t} + \nabla \cdot (\rho\mathbf{u}) = 0 \ . \tag{2.5}$$

The conservation of momentum, or Newton's second law, states that the total change of momentum is equal to the net applied force $d\mathbf{F}$, which in turn consists

of the pressure difference across the volume of the fluid element in inward normal direction, $-\nabla p \mathrm{d}V$ (see figure 2.1), and a possible external force $\mathbf{f}$:

$$\frac{D\mathrm{d}(m\mathbf{u})}{Dt} = \mathrm{d}F = -\nabla p \mathrm{d}V + \mathbf{f} \ . \tag{2.6}$$

In total we arrive at the *Euler equations*

$$\frac{\partial \mathbf{u}}{\partial t} + \mathbf{u} \cdot \nabla \mathbf{u} = -\frac{1}{\rho}\nabla p + \mathbf{f} \ . \tag{2.7}$$

The Euler equations (2.7) in conjunction with the continuity equation (2.5) provide a total of $d + 1$ evolution equations for $d + 2$ unknowns; what is still needed is a connection between the pressure $p$ and the fluid density $\rho$. For the compressible case, several possibilities are practical, ranging from simple assumptions such as $p \sim \rho$ (isothermal case) to an additional evolution equation for the temperature or internal energy. In the incompressible case, however, the velocity field $\mathbf{u}$ fulfills the additional constraint

$$\nabla \cdot \mathbf{u} = 0 \ . \tag{2.8}$$

This constraint is a good approximation to nature as long as the maximum velocity of the flow is far below the speed of sound in the fluid, and in fact is equivalent to the case of infinite speed of sound. Since the speed of sound is the upper bound for the velocity at which information of changes in the physical quantities are allowed to travel through the fluid, the simplification in (2.8) results in an instantaneous global reaction of the fluid to local changes. This infinitely fast propagation of information, as will be seen later, is realized by the way the pressure is modeled.

Combining the incompressibility constraint (2.8) with the continuity equation (2.5), we arrive at

$$\frac{\partial \rho}{\partial t} + \mathbf{u} \cdot \nabla \rho = 0 \ . \tag{2.9}$$

Thus, in the incompressible case, the initial density $\rho_0(\mathbf{x}) = \rho(\mathbf{x}, 0)$ is advected with the flow. In other words the density of a fluid element does no longer change in time. For an initially constant density $\rho_0(\mathbf{x}) = \text{const.}$ the fluid density no longer is an unknown and, without loss of generality, may be set to unity. The Euler equations then simplify to

$$\frac{\partial \mathbf{u}}{\partial t} + \mathbf{u} \cdot \nabla \mathbf{u} + \nabla p = 0 \tag{2.10}$$

in the absence of external forcing. In the course of this work, only the incompressible Euler equation of type (2.10) without external forcing will be considered. For the sake of simplicity, this equation will be called *Euler equation*, without additional specifiers such as "incompressible" or "force-free".

Despite the fact that equation (2.10) appears to consist of $d + 1$ unknowns, namely the velocity field $\mathbf{u}$ and the pressure $p$, the incompressibility constraint (2.8) actually determines the way the pressure behaves. This can be seen by taking the divergence of the Euler equations (2.7) and using the incompressibility constraint:

$$\Delta p = -\nabla \cdot (\mathbf{u} \cdot \nabla \mathbf{u}) \ . \tag{2.11}$$

For each instant in time the pressure is determined via a Poisson equation depending only on the present velocity field. Because of this elliptic connection, the Euler equations of the form (2.10) in conjunction with the incompressibility constraint (2.8) may be seen as a non-local evolution equation for the velocity field alone. Getting rid of pressure and density via the assumption of incompressibility has in turn resulted in non-locality of the evolution equation.

To arrive at a mathematically completely posed set of equation one has to provide equations (2.10) and (2.8) with appropriate boundary conditions. Throughout this thesis I will restrict this choice to the easiest alternatives of the whole space $\mathbb{R}^d$ or the $d$-dimensional torus $T^d$.

In addition, the *incompressible Navier-Stokes equation* is obtained by adding a friction term to the equation:

$$\frac{\partial \mathbf{u}}{\partial t} + \mathbf{u} \cdot \nabla \mathbf{u} + \nabla p = \nu \Delta \mathbf{u} \ , \tag{2.12}$$

where $\nu$ is the kinematic viscosity.

## 2.2. Properties of the Euler equations

The heuristic derivation of the Euler equations above gives an idea of the physical background of fluids in motion. It is necessary for a mathematical treatment of the equations, however, to introduce more rigorous definitions of fluid quantities and demonstrate some important connections between them.

### 2.2.1. Vorticity and strain

A revealing way to reformulate the incompressible Euler equations is in terms of the *fluid vorticity* $\boldsymbol{\omega} = \nabla \times \mathbf{u}$. By taking the curl of the Euler equation (2.10),

$$\frac{\partial \boldsymbol{\omega}}{\partial t} + \mathbf{u} \cdot \nabla \boldsymbol{\omega} = \boldsymbol{\omega} \cdot \nabla \mathbf{u} \ , \tag{2.13}$$

the pressure term vanishes and we arrive at the *vorticity formulation* of the Euler equations, which is an evolution equation for the vorticity vector field $\boldsymbol{\omega}(\mathbf{x}, t)$.

Equation (2.13) can be rewritten in terms of the convective derivative,

$$\frac{D\boldsymbol{\omega}}{Dt} = \boldsymbol{\omega} \cdot \nabla \mathbf{u} \,, \tag{2.14}$$

which emphasizes the fact that the vorticity formulation is an advection equation for the vorticity, with an additional term on the right hand side. This additional term, the *vortex stretching term*, is responsible for possible self-amplification processes and marks the very center of the fundamental difficulty of the 3-dimensional Euler equations, as will be discussed in more detail in chapters 4 and 5.

On the other hand, equation (2.14) highlights the radical difference between the cases $d = 2$ and $d = 3$. In the two-dimensional case, the right hand side of (2.14) disappears, as the velocity gradient is element of the tangent space while the vorticity is orthogonal to it in every point. Thus, in 2D, we arrive at

$$\frac{D\boldsymbol{\omega}}{Dt} = 0 \,. \tag{2.15}$$

For 2D flows the vorticity is just advected with the flow, vorticity is neither created nor destroyed via the flow dynamics. In particular, and in anticipation of the question for finite-time singularities, the maximum of the vorticity is constant in time. Even more drastic, in 2 dimensions every $L^p$-norm of the vorticity is conserved: By multiplying equation (2.15) by $\omega^{p-1}$, $p > 1$ and integrating, we get

$$\int_\Omega \omega^{p-1} \frac{\partial \omega}{\partial t} \, \mathrm{d}V + \int_\Omega \omega^{p-1} \mathbf{u} \cdot \nabla \omega \, \mathrm{d}V = 0$$

$$\Rightarrow \qquad \frac{\partial}{\partial t} \int_\Omega \omega^p \, \mathrm{d}V + \int_\Omega \mathbf{u} \cdot \nabla \omega^p \, \mathrm{d}V = 0$$

$$\Rightarrow \qquad \frac{\partial}{\partial t} \|\omega\|_{L^p(\Omega)}^p - \int_\Omega (\nabla \cdot \mathbf{u}) \, \omega^p \, \mathrm{d}V = 0$$

$$\Rightarrow \qquad \frac{\partial}{\partial t} \|\omega\|_{L^p(\Omega)} = 0 \,.$$

This connection turns out to be an easy and elegant way to get insight into how "tame" 2-dimensional Euler flows are in contrast to the 3-dimensional case.

Since in the 3-dimensional case vortex dynamics turn out to be more complicated, it is advantageous to establish further relations between the velocity gradient and the vorticity. First, note that the $3 \times 3$-Matrix $\nabla \mathbf{u}$ can be split in a symmetric part $S$ and an antisymmetric part $H$, $\nabla \mathbf{u} = S + H$, with

$$S = \frac{1}{2}(\nabla \mathbf{u} + \nabla \mathbf{u}^T), \tag{2.16}$$

$$H = \frac{1}{2}(\nabla \mathbf{u} - \nabla \mathbf{u}^T) \ . \tag{2.17}$$

$S$ is called the *strain tensor* or *deformation matrix*, whereas $H$ is the *rotation matrix*. The name of the latter already suggests its relationship to the vorticity, which precisely is given by

$$H\mathbf{v} = \frac{1}{2}\boldsymbol{\omega} \times \mathbf{v}, \qquad \forall\, \mathbf{v} \in \mathbb{R}^3 \ . \tag{2.18}$$

This connection is easily shown,

$$
\begin{aligned}
\frac{1}{2}(\boldsymbol{\omega} \times \mathbf{v})_k &= \frac{1}{2}\epsilon_{ijk}\epsilon_{mni}(\partial_m u_n)v_j \\
&= \frac{1}{2}(\delta_{jm}\delta_{kn} - \delta_{km}\delta_{jn})(\partial_m u_n)v_j \\
&= \frac{1}{2}(\partial_j u_k - \partial_k u_j)v_j \\
&= (Hv)_k \ ,
\end{aligned}
$$

using summation convention.

Since $S$ is symmetric by definition, there is a matrix $A \in \mathrm{SO}(3)$ such that $S$ becomes a diagonal matrix,

$$ASA^T = \mathrm{diag}(\lambda_1, \lambda_2, \lambda_3) \ , \tag{2.19}$$

where the $\lambda_i$ are the three eigenvalues of $S$. The incompressibility constraint ensures $\nabla \cdot \mathbf{u} = \mathrm{tr}(S) = \lambda_1 + \lambda_2 + \lambda_3 = 0$.

To formulate evolution equations for both $S$ and $H$, we take the gradient of the Euler equations (2.10):

$$\frac{D(\nabla \mathbf{u})}{Dt} + (\nabla \mathbf{u})^2 + P = 0 \ , \tag{2.20}$$

where $P$ is the pressure Hessian. Since $\nabla \mathbf{u} = S + H$, and

$$(\nabla \mathbf{u})^2 = \underbrace{(S^2 + H^2)}_{\text{symm.}} + \underbrace{(SH + HS)}_{\text{antisymm.}} \ , \tag{2.21}$$

we can divide equation (2.20) into its symmetric and antisymmetric part to arrive at the evolution equations for $S$ and $H$:

$$\frac{DS}{Dt} + S^2 + H^2 + P = 0 \tag{2.22}$$

$$\frac{DH}{Dt} + SH + HS = 0 \ . \tag{2.23}$$

It is possible to recover the velocity field from the vorticity field by applying the *Biot-Savart law* known from electrodynamics:

$$\mathbf{u}(\mathbf{x}) = \frac{1}{4\pi} \int \frac{1}{|\mathbf{x} - \mathbf{x}'|^3} \left( \mathbf{x} - \mathbf{x}' \right) \times \boldsymbol{\omega}(\mathbf{x}') \mathrm{d}\mathbf{x}' \ . \tag{2.24}$$

The integration over the whole domain in equation (2.24) again underlines the non-local nature of the incompressibility condition. The pressure term of the Euler equations (2.10) is eliminated in the vorticity formulation (2.13), but its non-locality is implicitly contained in the Biot-Savart law.

Since the strain is defined as symmetrized gradient of the velocity, the Biot-Savart law allows for the formulation of strain in terms of the vorticity. Differentiating (2.24) yields

$$\frac{\partial u_i(\mathbf{x})}{\partial x_j} = \frac{3}{4\pi} \int \frac{\epsilon_{ilk} y_j y_l}{|\mathbf{y}|^5} \omega_k(\mathbf{x}') \mathrm{d}\mathbf{x}' \ , \tag{2.25}$$

where $\mathbf{y} = (\mathbf{x} - \mathbf{x}')$ and using summation convention. Symmetrizing equation (2.25) results in

$$S_{ij} = \frac{3}{8\pi} \int \left( \epsilon_{ilk} y_j + \epsilon_{jlk} y_i \right) \frac{y_l \omega_k(\mathbf{x}')}{|\mathbf{y}|^5} \mathrm{d}\mathbf{x}' \ . \tag{2.26}$$

By means of equation (2.26) it is then possible to reformulate the Euler equations as an integro-differential equation in the vorticity $\boldsymbol{\omega}$ alone. Even though this is impractical for numerical simulations, it is of high educational value since it captures the dynamic interaction between vorticity and strain. It will therefore be reviewed to study possible scenarios for finite-time singularities in the Euler equations in chapter 4.

### 2.2.2. Particle trajectories and the flow map

The Euler equations in the form of (2.8) and (2.10) or in the vorticity formulation (2.13) are given in terms of scalar- or vector-valued fields defined in the whole domain $\Omega$. The physical location, described by the location vector $\mathbf{x} \in \Omega$, is in itself constant in time and may be thought of as a fixed frame of reference for the underlying fluid motion. This point of view is called the *Eulerian* viewpoint.

In contrast to this, it is possible (and often instructive) to follow the evolution of a fluid element within the fluid, or, in other words, to follow the motion of a particle which is advected with the flow. This point of view is called the *Lagrangian* viewpoint. At its core lies the *flow map* or *particle trajectory map* $\mathbf{X}(\boldsymbol{\alpha}, t) : \Omega \times \mathbb{R}^+ \to \Omega$,

$$\frac{d\mathbf{X}}{dt}(\boldsymbol{\alpha}, t) = \mathbf{u}(\mathbf{X}(\boldsymbol{\alpha}, t), t) \ , \qquad \mathbf{X}(\boldsymbol{\alpha}, 0) = \boldsymbol{\alpha} \ , \tag{2.27}$$

which describes the position of each fluid element at time $t$ originating from $\boldsymbol{\alpha}$.

The flow map $\mathbf{X}$ and its Jacobian $J(\boldsymbol{\alpha}, t) = \det(\nabla_{\boldsymbol{\alpha}} \mathbf{X}(\boldsymbol{\alpha}, t))$ allow for a reformulation of the incompressibility condition (2.8). It is easy to prove (see e.g. [72]) that the following statements are equivalent:

(i) $\nabla \cdot \mathbf{u} = 0$,

(ii) $J(\boldsymbol{\alpha}, t) = 1$,

(iii) $\forall U \subset \Omega, t \geq 0 : \ \mathrm{vol}(\mathbf{X}(U, t)) = \mathrm{vol}(U)$.

Especially (ii) may be used to derive connections in conjunction with the transformation formula.

Using the flow map to track the evolution of an arbitrary smooth vector field $\mathbf{h}(x, t)$ yields another useful relationship, which will be of importance on several occasions later on. If and only if

$$\mathbf{h}(\mathbf{X}(\boldsymbol{\alpha}, t), t) = \nabla_{\boldsymbol{\alpha}} \mathbf{X}(\boldsymbol{\alpha}, t) \mathbf{h}(\boldsymbol{\alpha}, 0) \tag{2.28}$$

then

$$\frac{D\mathbf{h}}{Dt} = \mathbf{h} \cdot \nabla \mathbf{u} \, . \tag{2.29}$$

This is seen as follows. First, the definition of the flow map (2.27) provides:

$$\frac{d\mathbf{X}}{dt}(\boldsymbol{\alpha}, t) = \mathbf{u}(\mathbf{X}(\boldsymbol{\alpha}, t), t)$$

$$\Rightarrow \qquad \frac{d}{dt} \nabla_{\boldsymbol{\alpha}} \mathbf{X}(\boldsymbol{\alpha}, t) = (\nabla \mathbf{u}) \nabla_{\boldsymbol{\alpha}} \mathbf{X}(\boldsymbol{\alpha}, t)$$

$$\Rightarrow \qquad \frac{d}{dt} \nabla_{\boldsymbol{\alpha}} \mathbf{X}(\boldsymbol{\alpha}, t) \mathbf{h}(\boldsymbol{\alpha}, 0) = (\nabla \mathbf{u}) \nabla_{\boldsymbol{\alpha}} \mathbf{X}(\boldsymbol{\alpha}, t) \mathbf{h}(\boldsymbol{\alpha}, 0) \, .$$



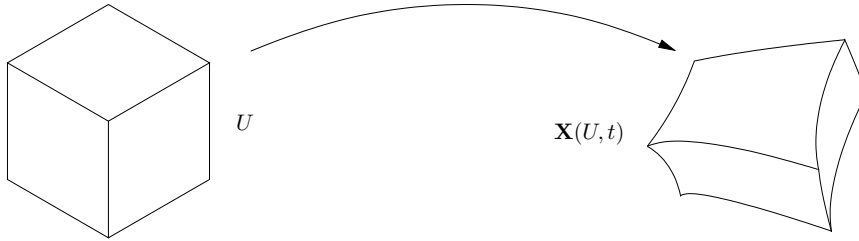$U$ $\qquad$ $\mathbf{X}(U, t)$

**Figure 2.2.**: Incompressibility condition in terms of the flow map. An infinitesimal volume element $U \subset \Omega$ may be deformed violently by the flow, but its image at later time, $\mathbf{X}(U, t)$ nevertheless retains the same volume.

On the other hand, equation (2.29) immediately reveals

$$\frac{d}{dt}\mathbf{h}(\mathbf{X}(\boldsymbol{\alpha},t),t) = \mathbf{u}\cdot\nabla\mathbf{h}(\mathbf{X}(\boldsymbol{\alpha},t),t) + \frac{\partial}{\partial t}\mathbf{h}(\mathbf{X}(\boldsymbol{\alpha},t),t)$$
$$= \mathbf{u}\cdot\nabla\mathbf{h}(\mathbf{X}(\boldsymbol{\alpha},t),t) + \Big(\mathbf{h}(\mathbf{X}(\boldsymbol{\alpha},t),t)\cdot\nabla\mathbf{u} - \mathbf{u}\cdot\nabla\mathbf{h}(\mathbf{X}(\boldsymbol{\alpha},t),t)\Big)$$
$$= (\nabla\mathbf{u})\mathbf{h}(\mathbf{X}(\boldsymbol{\alpha},t),t)\ .$$

Now, since both $\mathbf{h}(\mathbf{X}(\boldsymbol{\alpha},t),t)$ and $\nabla_{\boldsymbol{\alpha}}\mathbf{X}(\boldsymbol{\alpha},t)\mathbf{h}(\boldsymbol{\alpha},0)$ satisfy the same ODE with identical initial conditions $\mathbf{h}(\boldsymbol{\alpha},0)$ they must be equal for all times. I will later on refer to this law as the *transport formula*.

### 2.2.3. Conserved quantities

As argued above the Euler equations may be seen as a direct consequence of two conservation laws, namely the conservation of mass and the conservation of momentum. Yet a flow obeying the incompressible Euler equations exhibits conserved quantities beyond those two.

The *kinetic energy* of a flow is defined as

$$E_{\text{kin}} = \int_{\Omega}\frac{1}{2}|\mathbf{u}|^2\mathrm{d}^d x = \frac{1}{2}\|\mathbf{u}\|_{L^2(\Omega)}^2\ . \tag{2.30}$$

It holds that

$$\frac{dE_{\text{kin}}}{dt} = \int_{\Omega}\mathbf{u}\cdot\frac{\partial\mathbf{u}}{\partial t}\mathrm{d}^d x$$
$$= \int_{\Omega}\mathbf{u}\cdot(\mathbf{u}\cdot\nabla\mathbf{u} + \nabla p)\,\mathrm{d}^d x$$
$$= -\int_{\partial\Omega}\left(\frac{1}{2}|\mathbf{u}|^2 + p\right)\mathbf{u}\cdot\mathrm{d}\mathbf{A}\ ,$$

where in the last line both the incompressibility constraint and Gauss' theorem are used. Since the surface integral vanishes for the aforementioned boundary conditions (and even stationary rigid boundary conditions $\mathbf{u}\cdot\mathbf{n} = 0$ on $\partial\Omega$ for that matter), we arrive at the *conservation of kinetic energy*,

$$\frac{dE_{\text{kin}}}{dt} = 0\ . \tag{2.31}$$

Let furthermore $A(t=0)$ be a bounded, open, smooth surface, and $C(t=0)$ its smooth, oriented boundary, such that both evolve with the flow,

$$A(t) = \mathbf{X}(A(0),t),\qquad C(t) = \mathbf{X}(C(0),t)\ . \tag{2.32}$$
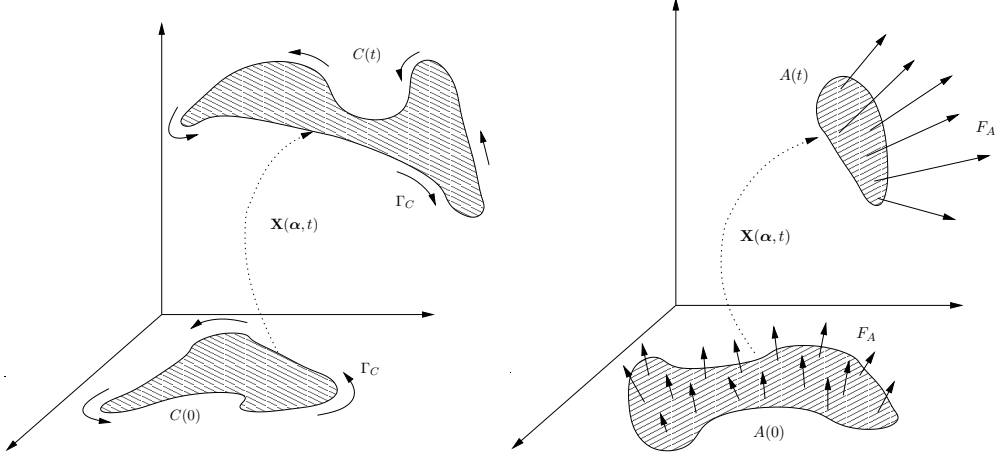
**Figure 2.3.**: The circulation $\Gamma$ of the velocity field along a curve $C(t)$ advected with the flow is conserved in time (**left**), as well as the flux of vorticity through the enclosed surface $A(t)$ (**right**).

Then the *circulation* along $C(t)$,

$$\Gamma_{C(t)} = \oint_{C(t)} \mathbf{u} \cdot \mathrm{d}\mathbf{s} \,, \tag{2.33}$$

is a conserved quantity,

$$\frac{D\Gamma_{C(t)}}{Dt} = 0 \,. \tag{2.34}$$

Equation (2.34) is often called *Kelvin's circulation theorem* (compare figure 2.3). To prove it, consider a line element $\mathrm{d}\mathbf{s}$ of $C(t)$. It is readily seen from the transport formula (2.29) that $\mathrm{d}\mathbf{s}$ obeys

$$\frac{D\mathrm{d}\mathbf{s}}{Dt} = \mathrm{d}\mathbf{s} \cdot \nabla\mathbf{u} \,. \tag{2.35}$$

Now
$$\begin{aligned}
\frac{D\Gamma_{C(t)}}{Dt} &= \frac{D}{Dt} \oint_{C(t)} \mathbf{u} \cdot \mathrm{d}\mathbf{s} \\
&= \oint_{C(t)} \left( \frac{D}{Dt}\mathbf{u} \cdot \mathrm{d}\mathbf{s} + \mathbf{u} \cdot (\mathrm{d}\mathbf{s} \cdot \nabla\mathbf{u}) \right) \\
&= \int_{A(t)} (\nabla \times (-\nabla p)) \cdot \mathrm{d}\mathbf{s} + \frac{1}{2} \int_{A(t)} (\nabla \times \nabla |\mathbf{u}|^2) \cdot \mathrm{d}\mathbf{s} \\
&= 0 \,.
\end{aligned}$$
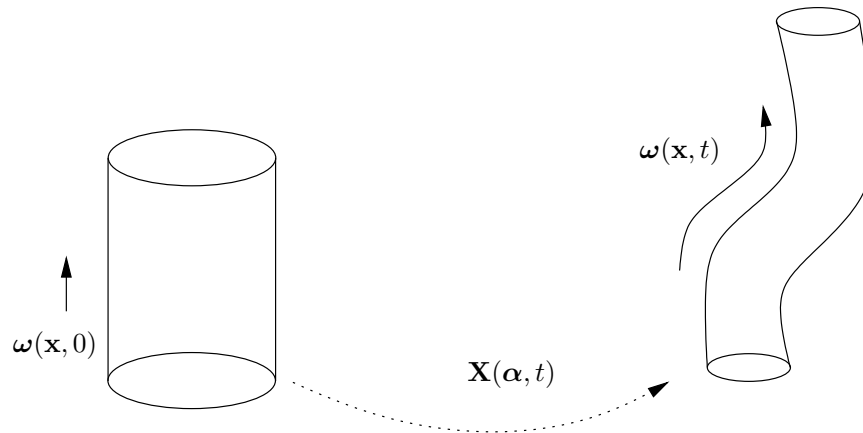
**Figure 2.4.**: The vortex stretching mechanism: If in some region the vorticity $\boldsymbol{\omega}$ is aligned parallel to the vortex stretching term $S\boldsymbol{\omega}$, then the vorticity is amplified. Due to conservation of vorticity flux the tube's diameter shrinks.

As immediate consequence, the vorticity flux through a Lagrangian surface

$$F_{A(t)} = \int\limits_{A(t)} \boldsymbol{\omega} \cdot \mathrm{d}\mathbf{s} \tag{2.36}$$

is conserved, too. This law, depicted in figure 2.3 (right), is sometimes called *Helmholtz' vortex theorem*.

### 2.2.4. Vortex dynamics, vortex lines and vortex stretching

Crucial to the understanding of the dynamics of the Euler equations is the evolution of the vorticity. As pointed out above, considerations concerning the vorticity easily suffice to rule out possible singular behavior of 2-dimensional flows (even if the rigorous proof is more intricate, e.g. given by Judovič [49] for weak solutions and by Kato [50] for classical solutions), whereas the whole complexity of 3-dimensional flows is best discernible when analyzing again the characteristics of the vorticity. And, famously beginning with the theorem of Beale et al. [3], much of today's research of inviscid fluid dynamics is focused on vortex dynamics, vorticity amplification mechanisms and vortex line geometry.

An insight into the process of vorticity amplification in a fluid element traveling with the flow is obtained by analyzing the vortex stretching term, as depicted in figure 2.4. Recalling the vorticity formulation (2.14) of the Euler equations,

and inserting the definition of the strain tensor we get

$$\begin{aligned}
\frac{D\boldsymbol{\omega}}{Dt} &= \boldsymbol{\omega} \cdot \nabla \mathbf{u} \\
&= \boldsymbol{\omega} \cdot (H + S) \\
&= S\boldsymbol{\omega} \, ,
\end{aligned} \tag{2.37}$$

since $H\boldsymbol{\omega} = \frac{1}{2}\boldsymbol{\omega} \times \boldsymbol{\omega} = 0$. As has already been pointed out, $S$ is symmetric, hence its eigenvalues $\lambda_i$ are real and the corresponding eigenvectors $\mathbf{v}_i$ are orthogonal. Without loss of generality we set $\lambda_1 \geq \lambda_2 \geq \lambda_3$. Define the *direction of vorticity* by

$$\boldsymbol{\xi}(\mathbf{x}, t) = \frac{\boldsymbol{\omega}(\mathbf{x}, t)}{|\boldsymbol{\omega}(\mathbf{x}, t)|} \, . \tag{2.38}$$

Now, the vortex stretching is most violent when $\boldsymbol{\xi}$ is aligned with the eigenvector $\mathbf{v}_1$ to the largest eigenvalue $\lambda_1$. In the worst case scenario of exact alignment and coupled growth, the vortex stretching term may become quadratic in $\boldsymbol{\omega}$, leading to an infinite amplification of vorticity in finite time. Whether such a scenario is prevented by inherent mechanisms of the Euler equations is not known. In chapter 5 scenarios are presented that are explicitly constructed having this amplification mechanism in mind.

Let us quantify the amplification of vorticity by introducing the *vorticity amplification factor* $\alpha(x)$, such that

$$\frac{D}{Dt}|\boldsymbol{\omega}| = \alpha|\boldsymbol{\omega}| \, . \tag{2.39}$$

Then, $\alpha$ is the projection of the vortex stretching term onto the direction of vorticity,

$$\alpha = (S\boldsymbol{\xi}) \cdot \boldsymbol{\xi} \, . \tag{2.40}$$

Proof:

$$\begin{aligned}
\frac{D}{Dt}|\boldsymbol{\omega}| &= \frac{\boldsymbol{\omega}}{|\boldsymbol{\omega}|} \cdot \frac{D}{Dt}\boldsymbol{\omega} \\
&= (S\boldsymbol{\omega}) \cdot \boldsymbol{\xi} \\
&= [(S\boldsymbol{\xi}) \cdot \boldsymbol{\xi}] \, |\boldsymbol{\omega}| \, .
\end{aligned}$$

This perspective may be contrasted by a strictly Lagrangian viewpoint of vortex dynamics. The fundamental connection to be named here is the *vorticity transport formula* (more details are given by e.g. Chorin and Marsden [21]). Following directly from the the vorticity formulation (2.14) in conjunction with the general transport formula (2.28) with $\mathbf{h}(\mathbf{x}, t) = \boldsymbol{\omega}(\mathbf{x}, t)$, the vorticity transport formula reads

$$\boldsymbol{\omega}(\mathbf{X}(\boldsymbol{\alpha}, t), t) = \nabla_{\boldsymbol{\alpha}}\mathbf{X}(\boldsymbol{\alpha}, t)\boldsymbol{\omega}(\boldsymbol{\alpha}, 0) \, . \tag{2.41}$$
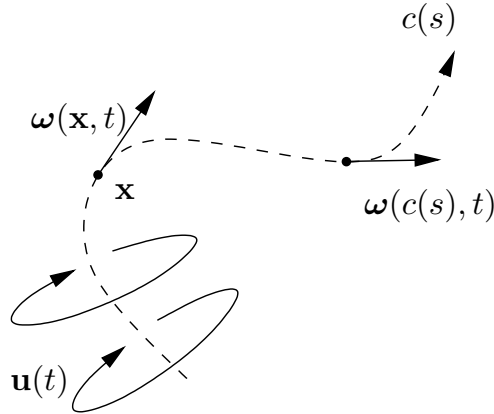
**Figure 2.5.**: Sketch of a vortex line. A vortex line is in every point tangent to the vorticity. Vortex lines are advected with the flow.

Since in two dimensions the term $\nabla_{\boldsymbol{\alpha}}\mathbf{X}(\boldsymbol{\alpha}, t)$ leaves the only non-vanishing component of the vorticity $\boldsymbol{\omega} = (0, 0, \omega_z)$ intact, we arrive at

$$\boldsymbol{\omega}(\mathbf{X}(\boldsymbol{\alpha}, t), t) = \boldsymbol{\omega}(\boldsymbol{\alpha}, 0) \ . \tag{2.42}$$

This derivation results in the Lagrangian equivalent of the already mentioned equation (2.15): In two dimensions, the vorticity is advected with the flow

For three space dimensions, equation (2.41) allows for complex behavior, which is best viewed in a geometric context. We therefore introduce the definition of the terms "vortex line" and "vortex tube". These will again be of importance in section 4.2 for the formulation of finite-time blowup criteria.

A *vortex line* at the time $t$ starting at the point $\mathbf{x}$ is a curve $c : \mathbb{R} \to \Omega$ with

$$\dot{c}(s) = \boldsymbol{\omega}(c(s), t), \qquad c(0) = \mathbf{x} \ , \tag{2.43}$$

which is an integral curve along the vorticity vector field. As long as the vorticity is Lipschitz continuous, the Picard-Lindelöf theorem implies unique existence of the vortex line.

With the help of the vorticity transport formula (2.41) it is easy to prove that vortex lines move with the flow (i.e. two points on the same vortex line that are advected with the flow stay on the same vortex line indefinitely). This is done by verifying that the Lagrangian image of the curve at later times, $\mathbf{X}(c(s), t)$, still is tangential to the vorticity vector field in all its points. Using the chain rule,

$$\frac{\partial}{\partial s}\mathbf{X}(c(s), t) = \nabla_{\boldsymbol{\alpha}}\mathbf{X}(c(s), t)\dot{c}(s) \tag{2.44}$$
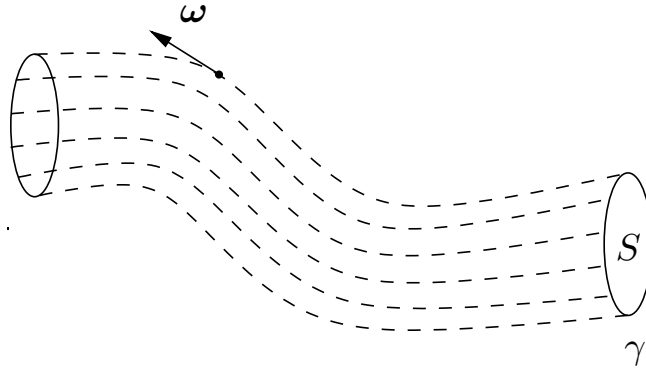
**Figure 2.6.**: Sketch of a vortex tube. A vortex tube is composed of vortex lines starting at a surface $S$ that is nowhere tangent to the vorticity.

$$= \nabla_{\boldsymbol{\alpha}} \mathbf{X}(c(s), t) \boldsymbol{\omega}_0(c(s)) \ . \tag{2.45}$$

Apply the vorticity transport equation (2.41) to arrive at

$$\frac{\partial}{\partial s} \mathbf{X}(c(s), t) = \boldsymbol{\omega}(\mathbf{X}(c(s), t), t) \ , \tag{2.46}$$

which shows that the Lagrangian image of the vortex line still is a valid vortex line in all points.

A *vortex tube*, as sketched in figure 2.6, is the collection of all vortex lines starting in each point of a surface $S$ that is in no point tangent to the vorticity vector field. With the same argument as above, a vortex tube is transported in the flow.

As a simple consequence of the solenoidality of the vorticity vector field, the flux of vorticity through different cross-sections of the tube is identical by Gauss' law. The thinning of a vortex tube in a region always coincides with an increase of vorticity in that region. Or, anticipating possible blowup scenarios: For the vorticity to grow indefinitely in a point, the surrounding vortex tube has to collapse to zero thickness. It is not known, whether this can happen in finite time. As depicted in figure 2.4, a possible mechanism for the collapse of vortex tubes could be the vortex stretching term.

The connections and definitions given in this chapter will serve as a basis for the understanding of the possible formation of singularities in the Euler equations. They will be used to derive blowup criteria in chapter 4 which can be verified by numerical simulations.

# 3. Numerics

All numerical simulations throughout this thesis were conducted using the newly developed framework *racoon III* (refined adaptive computations with object-oriented numerics). As the goal of this thesis implies the need for high resolution simulations of the Euler equation, a considerable amount of work had to be put into the development of new components for the framework or the extension of existing ones. The choice of numerical algorithms for the problems at hand have a crucial impact on the overall performance and accuracy of the simulations. In the following sections I will, therefore, lay out the relevant modules of the framework, with a focus on the consequences of several aspects of incompressible fluid dynamics and the search for finite-time singularities on various design choices.

First, a brief introduction into the core features of the framework *racoon III* will be given in section 3.1. The focus here is on the interplay between adaptively refined meshes, massively parallel computing and their implications on the integration of the Euler equations.

In section 3.2, the discretization and numerical scheme for integrating the Euler equations will be presented. A comparison between competing methods will be made with emphasis on their applicability to the hunt for finite-time singularities and the observation of geometric flow properties.

As part of the simulation of the Euler equations, the incompressibility condition necessarily involves the solution of a Poisson equation, which will be treated with the multigrid algorithm. Specific ramifications of adaptively refined grids on the solution of the elliptical problem will be discussed in section 3.3.

A key aspect of this thesis is the geometry of Lagrangian vortex line segments and geometric criteria for identifying finite-time singularities of the Euler equations. Section 3.4 will briefly present the diagnostic tools utilized to monitor the Lagrangian and geometric properties of the considered flows.

Section 3.5 deals with the implications of conducting simulations on parallel machines with thousands of cores. Here, I will give a short overview over the scaling properties of *racoon III* and the extensions implemented to increase the parallel performance.

# 3.1. Numerical framework

The basis of all simulations presented in this work is the newly developed framework *racoon III*. Its key feature is the integration of partial differential equations on adaptive grids on massively parallel distributed computers. It allows for various integration and reconstruction schemes, staggered grids, modules to solve elliptic problems and provides several diagnostic tools like passive tracer particles or vector field integral curves at runtime. It is based on *racoon* [33].

As *racoon III* is object-oriented, the implementation of the differential equation in question takes place when deriving a problem-specific implementation from an abstract problem-class. Several callback functions, invoked by the main loop on each node and the time-integration scheme, allow for data manipulation, output and diagnostics. Also, the problem class is the only place where the actual physical equations are located. It is, thus, easy to change the problem formulation without the need of rewriting code distributed over several files. Furthermore, the integration scheme, the interpolation method or other purely numeric modules can be replaced without altering the physical equations.

## 3.1.1. Static grid and the block structure

The computational domain is covered by a Cartesian grid in memory. The values at each grid point represent the value of a physical quantity at the center, face, edge or corner of a cell, or the spatial average of this field across the cell (see figure 3.1).

Data distribution across the processes is realized by using *blocks* of fixed size $n$ (typically from 8 to 64 cells in each direction) arranged on different *levels $L$*, representing the degree of refinement. The $0^{\text{th}}$ level consists of only one block, stretching across the whole computational domain, while the subsequent levels bisect the parent blocks in each dimension, resulting in an logical octree with $2^{L \cdot d}$ blocks on level $L$ ($d$ being the dimension of the domain). This leads to a total of $(n \cdot 2^L)^d$ grid points in total.

Each block is surrounded with at least two *boundary cells* or *ghost cells*, as pictured in figure 3.1, to ensure that each cell has two valid neighbors throughout the computation. This is necessary for numerous computational steps such as derivatives via finite differences or error smoothing. These "ghost cells" overlap with the neighboring block and mirror its data. When necessary, all boundary cells are synchronized via an exchange with their neighbors.

## 3.1.2. Adaptive mesh refinement

A key feature of *racoon III* is its ability to refine the grid adaptively. Many problems in fluid dynamics and finite-time singularity simulations in particular
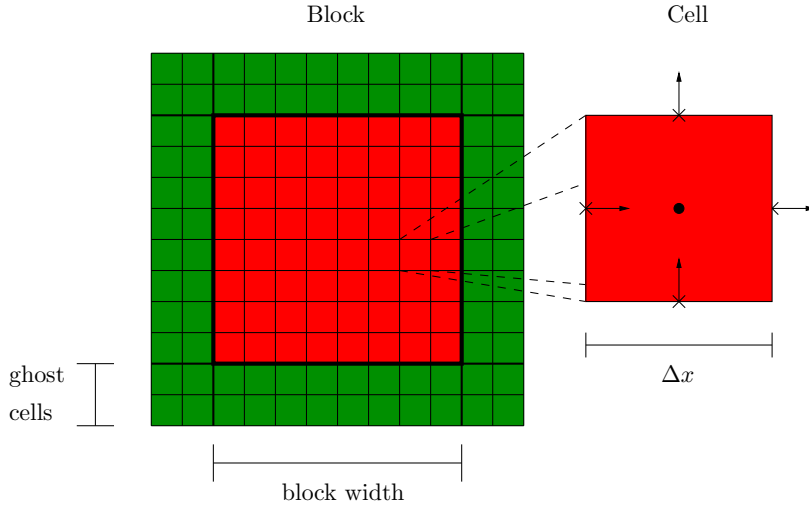
**Figure 3.1.**: A block in *racoon III* has a fixed number of inner cells (red, here 8x8), surrounded by boundary cells (green) that hold copies of the data of neighboring cells. Every cell can store a value for each field, located either in the center, at the boundaries, at the edges or at the vertices of the cell.

feature structures localized in space, while huge fractions of the domain remain devoid of action. In such a scenario, for a given amount of computer memory, a fixed mesh would under-resolve the crucial parts while wasting resources on the less important ones. Most Euler blowup scenarios feature extremely localized structures with steep gradients. Therefore, adaptive mesh refinement (AMR) is of utmost importance for the work conducted in this thesis. Many design choices in *racoon III* were explicitly made to facilitate adaptive mesh refinement.

Adaptive mesh refinement increases the locally available resolution, but comes at the cost of additional computational overhead. It complicates the framework in several ways. Most importantly, it restricts the choice of numerical schemes to comparatively simple low order finite difference or finite volume variants. A direct comparison to high accuracy pseudo-spectral simulation was made by Grafke et al. [41] for the case of Euler equations. It was found that a resolution approximately 1.3 times higher is needed to reach a comparable accuracy for the adaptively refined code.

At the coarse-fine interfaces of refined grids, the framework relies on interpolation to fill the corresponding ghost-cells with valid data. This may introduce additional errors, especially if the number of derivatives acting upon the interpolated quantities is high. For the numerical scheme used throughout this work, special arrangements have been made to minimize the influence of this error. This will be presented in section 3.2.2.

### 3.1.3. Refinement criteria

To decide which regions are to be refined, a certain criterion is tested periodically for each block. The criterion depends, for example, on the fields, their derivatives or a more complicated formula. If the block is flagged as being under-resolved, it is bisected into $2^d$ child blocks that are redistributed among the available nodes. The resolution of the parent block is thus effectively doubled. The opposite happens for blocks that are over-resolved: $2^d$ blocks are merged into one, the resolution at this location is halved. With this procedure, the grid is constantly changing and adapting to the simulation, allowing high resolution at critical locations but not wasting any resources for the rest.
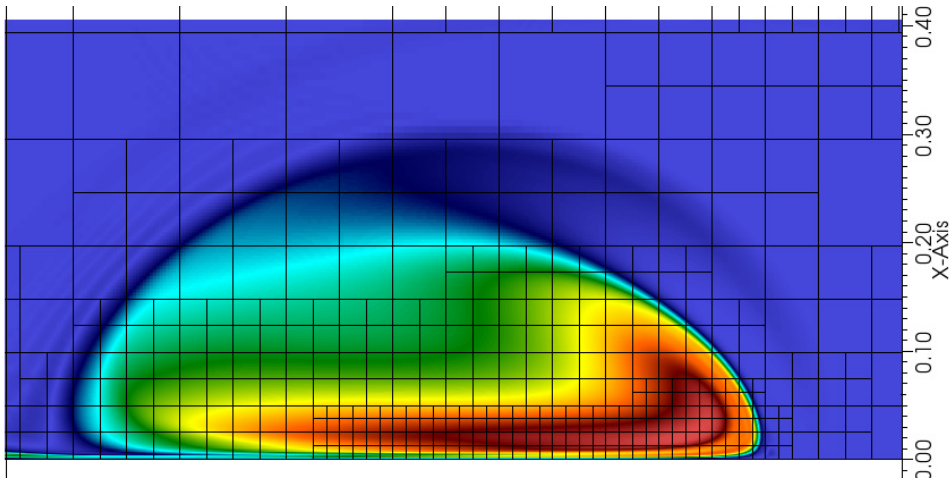


**Figure 3.2.**: Refinement criterion for the simulation of the Euler equations with *racoon III*. Regions with a large value for $\|\nabla\mathbf{u}\|$ are resolved higher. Each square represents a block with $16^3$ cells. Shown is the absolute vorticity for a cross-section of one vortex tube.

For the purposes of this work, different refinement criteria were considered:

(i) The absolute value of the vorticity, $|\boldsymbol{\omega}(\mathbf{x}, t)|$,

(ii) the norm of the gradient of velocity, $\|\nabla\mathbf{u}(\mathbf{x}, t)\|$,

(iii) a direct measurement of the discretization error by comparing finite differences at different mesh sizes (e.g. $\Delta x$ vs. $2\Delta x$, Richardson-Extrapolation),

(iv) one of the above criteria to some exponent $p$, to sharpen or smoothen the effects of mesh refinement.

(v) A fixed (non-adaptive) mesh refinement based on the known evolution of the flow from previous simulations.

For the production runs presented in this thesis, either a combination of (ii) and (iv) (as shown in figure 3.2) was used, or a fixed mesh refinement (v) was chosen. The former produces sharp adaptively refined grids which follow the structures of the flow but may become complicated in time, while the latter allows for faster and more robust refined meshes without the need for frequent remeshing and redistribution.

### 3.1.4. Dynamic load balancing and the Hilbert curve
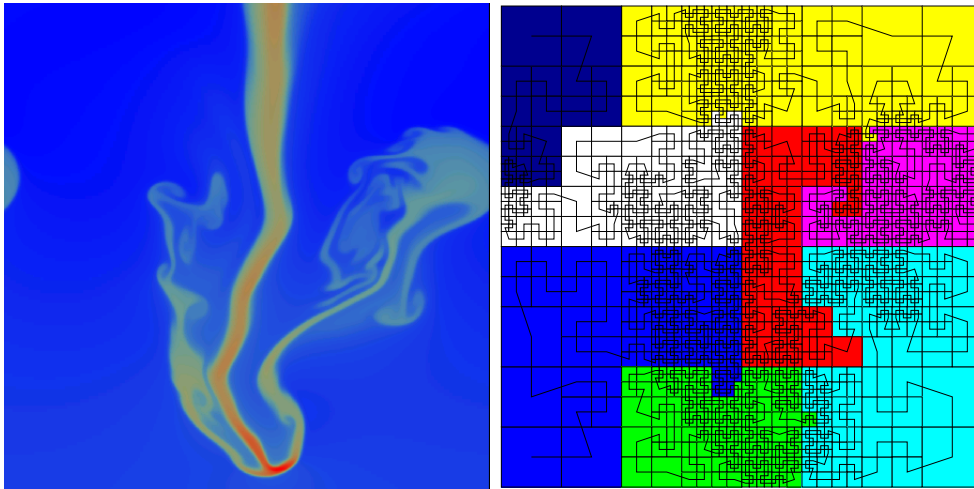


**Figure 3.3.**: Adaptive mesh refinement and dynamic load balancing. The workload is distributed among different processors along a space-filling Hilbert curve.

Since communication between different nodes is the smallest bottleneck due to limited bandwidth and high latency, it is advantageous to arrange the blocks in a way that physically close blocks are located on the same node. Even if this seems to be pretty straight-forward for normal grids, it poses a larger problem for adaptive grids with different resolutions. In *racoon III*, blocks are distributed along a space-filling Hilbert curve, as sketched in figure 3.3.

This ensures that proximate blocks are located on the same node even if the grid is not fixed. Currently *racoon III* uses a slightly different approach, using independent Hilbert curves for each level, since inter-level communication is the most frequent type of communication for common problems. Every time the grid changes when adapting to the current situation, the Hilbert curve is recalculated, as is the workload for each node. If an imbalance is detected, the blocks are redistributed along the curve, each node getting the same amount of blocks (if possible).

### 3.1.5. Time integration

Consider a discretized partial differential equation of the form

$$\partial_t y(\mathbf{x}, t) = f(t, y), \tag{3.1}$$

where $f$ is a differential operator, consisting of spatial derivatives. To integrate a partial differential equation of form (3.1) in time, a strong stability preserving Runge-Kutta integrator according to [88] is used. Written in its general form, the time integration in $s$ steps is carried out via

$$y_{n+1} = y_n + \Delta t \sum_{i=1}^{s} b_i k_i,$$

where

$$k_i = f(t_n + c_i \Delta t, y_n + \sum_{j=1}^{i-1} a_{ij} \Delta t k_j).$$

The constants $a_{ij}$, $b_i$ and $c_i$ specify the particular method and order of the scheme. For *racoon III*, this method is implemented up to third order.

The time stepping $\Delta t$ is estimated periodically and problem-depending by invoking a virtual method that calculates the maximal integration step for each block independently and takes the minimum for the next time steps, adhering the Courant-Friedrichs-Lewy (CFL) condition,

$$\Delta t \leq c_{\text{cfl}} \frac{\Delta x}{v_{\text{max}}},$$

where $c_{\text{cfl}}$ is a real constant and $v_{\text{max}}$ the maximum speed for the advancement of information. For reasons of simplicity grid-adaptive time stepping is not supported in *racoon III*, and $\Delta x$ refers to the grid spacing of the highest resolved block in AMR simulations.

## 3.2. Numerical Schemes

The simulation of the three-dimensional Euler equations allows for a wide range of numerical schemes to be applied. Not only is there a freedom of choice for the underlying equation (e.g. the formulation in velocity as presented in equation (2.10) or the formulation in vorticity like equation (2.13)), but also in the applied numerical algorithms and the collocation of physical quantities in the cell. Especially the non-local nature of the pressure or the incompressibility condition may be enforced in different ways.

## 3.2.1. Discretization

Since the problem at hand benefits considerably from utilizing locally refined meshes, a finite difference approach is both the most flexible and efficient choice in *racoon III*. Disadvantages from low spatial order are by far compensated by the locally increased resolution. Nevertheless, a finite-difference approach leaves the freedom to choose the discretization and the underlying equation. For this thesis, several distinct schemes were implemented and compared against each other: The Harlow-Welch scheme, the staggered vector-potential scheme and the CWENO vector-potential scheme. These schemes will be introduced and weighed against each other in the following paragraphs.

**Harlow-Welch**

The scheme of Harlow and Welch [46], or MAC-scheme, was introduced to simulate the two-dimensional Navier-Stokes equations with free surfaces. It was the first scheme featuring a staggered grid for the velocity field components to implement an *exact projection* to enforce the incompressibility condition.

In particular, as depicted in figure 3.4 (left), the Harlow-Welch scheme defines the pressure in the center of a grid cell, while the velocity components are located at the center of the cell faces. This is motivated by the fact that the resulting Poisson equation for the elliptic part, both for the Navier-Stokes and the Euler equations, couples all pressure unknowns. An unstaggered alignment, in contrast, decomposes into several (uncoupled) subgrids. Since the solution of the Poisson equation is only determined up to a constant, and this constant may differ for each subgrid, spurious oscillations may be introduced in the unstaggered discretization. It is therefore reasonable to locate velocity and pressure for the three-dimensional Euler equations in the same way as introduced by Harlow and Welch.

Numerous authors have applied these staggered grid or projection methods to the Navier-Stokes or Euler equations (see e.g. [17, 18]), usually by first advancing the velocity field via the nonlinearity,

$$\tilde{\mathbf{u}} \leftarrow \mathbf{u}^n + \Delta t \mathbf{u}^n \cdot \nabla \mathbf{u}^n \,, \tag{3.2}$$

without obeying the incompressibility condition and subsequently executing a projection of the velocity to its solenoidal part,

$$\mathbf{u}^{n+1} \leftarrow \mathrm{P}\tilde{\mathbf{u}} \,, \tag{3.3}$$

where P is the Leray-projection operator (see e.g. [26]). By defining the discrete divergence operator $D$ and discrete gradient operator $G$ such that

$$D\mathbf{u}_{(i,j,k)} = \frac{u_{x\,(i+1,j,k)} - u_{x\,(i,j,k)}}{\Delta x} + \frac{u_{y\,(i,j+1,k)} - u_{y\,(i,j,k)}}{\Delta y} + \frac{u_{z\,(i,j,k+1)} - u_{z\,(i,j,k)}}{\Delta z}$$

$$\tag{3.4}$$

$$G\Phi_{(i,j,k)} = \left( \frac{\Phi_{(i,j,k)} - \Phi_{(i-1,j,k)}}{\Delta x}, \frac{\Phi_{(i,j,k)} - \Phi_{(i,j-1,k)}}{\Delta y}, \frac{\Phi_{(i,j,k)} - \Phi_{(i,j,k-1)}}{\Delta z} \right), \quad (3.5)$$

the Hodge-decomposition for every discrete vector field **u**,

$$\mathbf{u} = \mathbf{u}^D + G(\Phi) \text{ with } D\mathbf{u}^D = 0 \tag{3.6}$$

is unique (for given boundary conditions) and the Leray-projection fulfills

$$D\left(\mathrm{P}\mathbf{u}\right) = 0 \tag{3.7}$$

exactly up to truncation error. This exact projection justifies the staggered arrangement of the physical quantities. Furthermore, it is optimal in efficiency, since it involves the solution of only one Poisson equation (as opposed to three in the methods presented below).

A higher order variation of this scheme was introduced by Bell et al. [5] and an improvement for adaptively refined grids was done by e.g. Minion [75], even though for just two dimensions.

An additional advantage of schemes of this kind is their ability for a conservative formulation of the hydrodynamical equation. With a special reformulation of the operators $D$ and $G$ at the coarse-fine interfaces (as shown in section 3.3.2), these properties are even portable to adaptively refined grids.
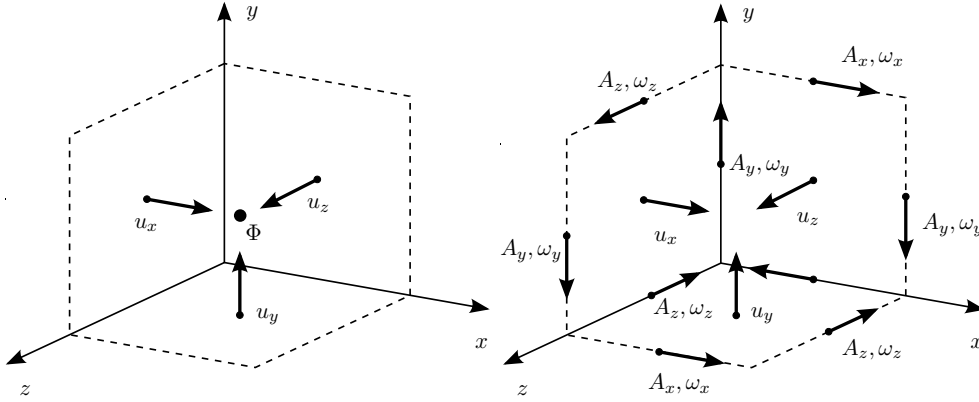


**Figure 3.4.**: **Left:** Staggered arrangement of velocity **u** and pressure correction field $\Phi$ in the grid cells for the Harlow-Welch scheme. **Right:** Staggered arrangement of vector potential **A**, velocity **u** and vorticity $\boldsymbol{\omega}$ in the grid cells for the staggered vector potential scheme.

Nevertheless, a significant disadvantage limits the use of the Harlow-Welch projection schemes for the purposes considered in this work: Most of the criteria for analyzing possible blowup scenarios for the incompressible Euler equations (see section 4.1) require the evaluation of the vorticity $\boldsymbol{\omega}$, its direction, or even

its derivative (e.g. $\nabla \xi$, vortex line curvature $\kappa$, $\nabla \cdot \xi$). Since in the considered case the velocity $\mathbf{u}$ is the primary variable and derivatives are only second order exact, these quantities would be unavailable. This effectively rules out the Harlow-Welch projection methods for analysis via Lagrangian and geometric criteria with adaptive mesh refinement.

**Staggered grid vector-potential**

Instead of integrating the Euler equations of the form (2.10) in time, it is reasonable to take the vorticity evolution equation (2.13) as a basis for a numerical scheme. In doing this, the main difficulty of the previous projection schemes is circumvented: The primary variable of integration is now the vorticity $\boldsymbol{\omega}$ instead of the velocity $\mathbf{u}$. There is considerable freedom in the exact form of the nonlinear term:

$$\partial_t \boldsymbol{\omega} = -\nabla \times (\mathbf{u} \cdot \nabla \mathbf{u}) \tag{3.8}$$
$$= \boldsymbol{\omega} \cdot \nabla \mathbf{u} - \mathbf{u} \cdot \nabla \boldsymbol{\omega} \tag{3.9}$$
$$= S \boldsymbol{\omega} - \mathbf{u} \cdot \nabla \boldsymbol{\omega} \tag{3.10}$$
$$= \nabla \times (\mathbf{u} \times \boldsymbol{\omega}) \tag{3.11}$$

All forms coincide in that they eliminate the pressure term from the equation. The non-local (in space) nature of the incompressibility condition is instead shifted to the calculation of the velocity field from the vorticity. A way to accomplish this is the introduction of a vector potential $\mathbf{A}(\mathbf{x}, t)$ for the velocity, with

$$\nabla \times \mathbf{A}(\mathbf{x}, t) = \mathbf{u}(\mathbf{x}, t), \tag{3.12}$$

which is determined by the solution of three Poisson equations,

$$\Delta \mathbf{A}(\mathbf{x}, t) = -\boldsymbol{\omega}(\mathbf{x}, t). \tag{3.13}$$

The emerging gauge freedom of the vector potential is usually resolved by taking the Coulomb-gauge,

$$\nabla \cdot \mathbf{A}(\mathbf{x}, t) = 0, \tag{3.14}$$

with corresponding boundary conditions.

Even though solving equation (3.13) requires three times the computational cost of just calculating the projection (3.3), all inter-grid communication and interpolation is done in the vorticity, which is a necessary condition for the numerical treatment of geometric blowup criteria.

Collocation of the physical quantities $\mathbf{A}$, $\mathbf{u}$, $\boldsymbol{\omega}$ is still arbitrary. For the *staggered grid vector potential* formulation, the arrangement is chosen as depicted in figure 3.4 (right): The vector potential $\mathbf{A}$ and the vorticity $\boldsymbol{\omega}$ are located on
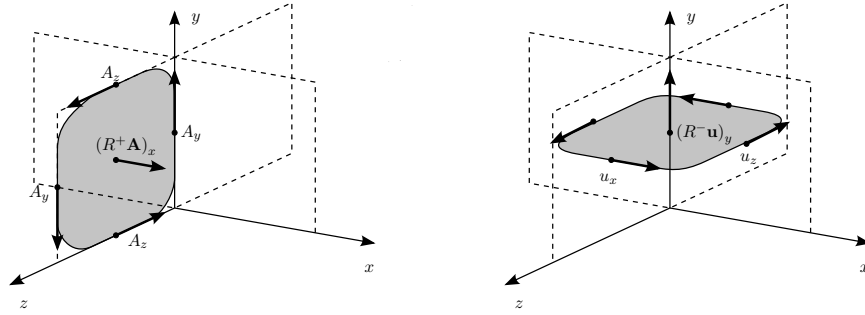
**Figure 3.5.**: Collocation of the physical quantities for the staggered vector potential scheme permits the definition of staggered rotation operators $R^+$ (**left**) and $R^-$ (**right**)

the edges of each cell, the velocity $\mathbf{u}$ on the face center. Now, define two discrete curl-operators $R^+$ and $R^-$ via

$$\left(R^+\mathbf{v}\right)_{x(i,j,k)} = \frac{v_{z(i,j+1,k)} - v_{z(i,j,k)}}{\Delta y} - \frac{v_{y(i,j,k+1)} - v_{y(i,j,k)}}{\Delta z} \tag{3.15}$$

$$\left(R^-\mathbf{v}\right)_{x(i,j,k)} = \frac{v_{z(i,j,k)} - v_{z(i,j-1,k)}}{\Delta y} - \frac{v_{y(i,j,k)} - v_{y(i,j,k-1)}}{\Delta z} \tag{3.16}$$

and permutations of $x, y, z$ (compare figure 3.5).

These definitions render the discrete calculation of the velocity from the vector potential, $\mathbf{u} = R^+\mathbf{A}$, and the vorticity from the velocity, $\boldsymbol{\omega} = R^-\mathbf{u}$, exact in a way that it fulfills the incompressibility condition $D\mathbf{u} = 0$ up to the truncation error (with $D$ defined as above). Therefore, oscillations and grid decoupling (checkerboard instability), as well as unnecessary interpolation, are minimized.

This formulation is advantageous for finite difference schemes, as long as the grid is regular. For adaptively refined grids, the situation is somewhat more complex: The control volume for a quantity on the edge of a cell located at a coarse-fine interface has a considerably more intricate shape. For complex grid arrangements in three space dimensions, an impractical number of special cases has to be considered, further increased by the different collocation of the separate components of each vector field. This is even more severe in the adaptive multigrid solver. In the case of adaptively refined simulations of the Euler equations, this proved to be a fatal shortcoming of this type of scheme, as the implementation becomes far too complex.

### CWENO vector-potential

Another way to discretize the vorticity formulation (2.13) is to arrange all physical quantities in a cell-centered fashion. This allows for the familiar use of the

multigrid algorithm on adaptive grids and does not introduce difficulties concerning the definition of control volumes at coarse-fine interfaces. Again, the vorticity $\boldsymbol{\omega}$ is the primary variable. Since the advantages of the sophisticated staggering of the staggered vector potential scheme is sacrificed in order to keep the adaptive mesh refinement tractable, the resulting cell-centered discretization may introduce spurious oscillations due to grid decoupling (checkerboard instability).

For the *CWENO vector-potential scheme* this disadvantage is overcome by instead integrating the equation

$$\partial_t \boldsymbol{\omega} = -\nabla \times \left( \nabla \left( \mathbf{u} \otimes \mathbf{u} \right) \right), \tag{3.17}$$

where "$\otimes$" denotes the dyadic product. The term $\nabla \left( \mathbf{u} \otimes \mathbf{u} \right)$ is calculated, inspired by finite volume schemes, with a Kurganov-Tadmor [68] scheme in combination with a CWENO-reconstruction [67] of the velocity $\mathbf{u}$ to the cell interfaces, which was already implemented in *racoon*. This permits a third-order accuracy in smooth regions and effectively reduces spurious oscillations in regions with steep gradients. As a result, grid decoupling is circumvented for the cell-centered formulation at the price of a slightly increased numerical dissipation in the presence of steep gradients. Numerical tests have shown that this effect is less severe for the considered case of the Euler equations than a stabilization with the help of artificial viscosity.

In total, the scheme, as presented, consists of several steps. Starting with an approximation to the vorticity $\boldsymbol{\omega}^n$ at time $t^n$,

1. calculate the vector potential $\mathbf{A}^n$ from the vorticity $\boldsymbol{\omega}^n$ via

$$\mathbf{A}^n \leftarrow -\Delta^{-1} \boldsymbol{\omega}^n, \tag{3.18}$$

   where the inverse Laplacian is computed via the refined mesh multigrid algorithm presented in section 3.3,

2. compute the velocity $\mathbf{u}^n$ from the vector potential $\mathbf{A}^n$,

$$\mathbf{u}^n \leftarrow \nabla \times \mathbf{A}^n, \tag{3.19}$$

3. compute the change of impulse in each cell via summation of the fluxes through each interface,

$$\mathbf{N}^n \leftarrow \nabla \left( \mathbf{u}^n \otimes \mathbf{u}^n \right) \tag{3.20}$$

   with the help of the CWENO-reconstruction,

4. apply the nonlinearity to get a new approximation for the vorticity $\boldsymbol{\omega}^{n+1}$,

$$\boldsymbol{\omega}^{n+1} \leftarrow \boldsymbol{\omega}^n - \Delta t \left( \nabla \times \mathbf{N}^n \right). \tag{3.21}$$

This sequence of steps comprises one Euler-forward step in time. It establishes the building block for one Runge-Kutta sub-step as presented in section 3.1.5 to achieve third order accuracy in time.

In comparison to the schemes presented before, this approach offers the advantage of featuring the vorticity as the primary variable, which is a necessary condition for advanced diagnostics of the vorticity field. In addition, it is readily transferable to adaptively refined meshes, an indispensable feature for the extremely localized nature of possibly singular configurations. It was therefore the scheme of choice for all production simulations presented in this thesis.

### 3.2.2. Overlap

As lined out in section 3.1.2, communication between blocks is realized with the use of ghost cells. The data stored in the ghost cells is used to calculate finite differences and has to be updated whenever the original data is modified. This update necessarily includes interpolation as soon as ghost cells overlap data of different resolution in an adaptively refined simulation. Since the above presented vector potential schemes require a huge number of differentiations of the vector potential, the requirements for the order of the ghost cell interpolation are quite severe.
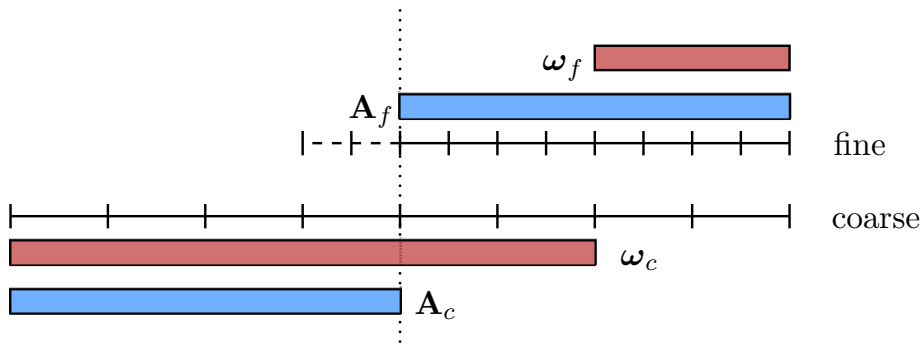


**Figure 3.6.**: Overlapping grids at coarse-fine interfaces of adaptively refined meshes. The vector potential is valid on the blue part of the grid, while the vorticity is trusted only in the region highlighted in red. Thus, no derivative has to be calculated for an interpolated quantity.

To counter this, a kind of *overlapping grids* was introduced at the coarse-fine interfaces of the adaptively refined grids. As shown in figure 3.6, the physical equation is integrated at all levels of resolution in parallel. At the coarse-fine interfaces of refined grids, different physical quantities have different areas of validity: The vector potential approximation is assumed to be correct on the blue marked cells while the updated vorticity is only trusted on the red marked

cells. By doing this, no derivative has to be calculated for an interpolated quantity.

After each sub-step, the original refined grid for the vorticity is recovered via interpolation. This means in conclusion that interpolated data is only considered in the computation as part of the right-hand-side of the Poisson equation. Combining this overlap with the CWENO vector potential scheme, the vorticity $\boldsymbol{\omega}$ is not only the primary variable in the time integration, but also is the only quantity to be interpolated in the course of the simulation. The interpolated values only enter the computation as source terms for the calculation of the vector potential. The overall scheme is therefore very robust against disturbance introduced by the varying grid spacing.

## 3.3. Multigrid on refined meshes

All schemes presented above need at some point the solution of the three-dimensional Poisson equation

$$\Delta\phi = \rho \tag{3.22}$$

on a domain $\Omega$, with a potential $\phi$ and a source term $\rho$. This was accomplished with a *multigrid* method, which is regarded as the fastest numerical method for the solution of elliptic partial differential equations in general. Even if a wide range of problems can be solved efficiently with the multigrid approach, only the Poisson equation is of any relevance to the vorticity- or staggered grid formulations. An implementation of the multigrid algorithm was written for the framework *racoon III*. Technical details will be explained in appendix B for equally spaced grids.

In the considered case, the grid is adaptively refined to match the underlying physical problem. One therefore has to extend the presented algorithm to such a more complex grid structure. At its core, the multigrid algorithm is capable of respecting such a grid structure by just smoothing, restricting and correcting the refined regions for incomplete levels and ignoring the non-refined parts. Nevertheless two notable problems remain. Their solutions will be presented in the following paragraphs.

### 3.3.1. Full approximation scheme

On all but the finest level the basic multigrid algorithm, as presented in appendix B, solves defect equations (B.4) instead of the original equation (B.1). Because of that, partially refined levels end up with an approximation to the error instead of an approximation to the potential. To overcome this technical difficulty, the *Full Approximation Scheme* (FAS) was used. Originally designed for nonlinear equations its purpose in this context lies in the fact that the data held on all

levels is the true potential $\phi$ instead of the defect $r$. Since for adaptively refined meshes the multigrid algorithm locally features coarser grids, the correct solution already is present for all different resolutions.

Details and a formal derivation of the full approximation scheme is given in section 5.3.4 of Trottenberg et al. [91]

### 3.3.2. Flux conservation across AMR interfaces

In finite volume formulation, the multigrid algorithm for refined meshes is not conservative across interfaces between coarse and fine grids. This introduces spurious sources terms on these interfaces, which results in a discontinuity in the gradient of the potential and consequentially in a non-vanishing divergence if the multigrid is used for e.g. a projection method. The following paragraph describes how this problem was overcome via a special reformulation in fluxes and a subsequent flux-fix after each smoothing step for the partially refined levels.

According to a (second order) finite volume formulation, physical quantities are interpreted as cell-averages, represented by values located at the center of each cell. The setup near a coarse-fine interface is as depicted in figure 3.7.
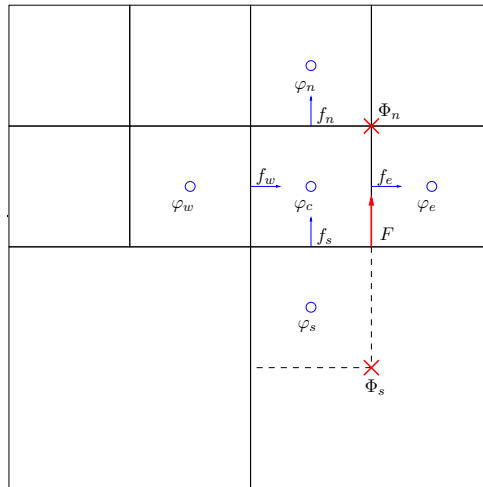


**Figure 3.7.**: A coarse-fine-interface with differing fluxes on the fine and coarse grid. Flux conservation dictates a Neumann boundary condition for the fine grid region to agree with the coarse grid fluxes through the interface.

Here, $\varphi_n$, $\varphi_s$, $\varphi_w$ and $\varphi_e$ are meant to be values of the potential located in the cell centers on the fine grid, placed around the cell containing $\varphi_c$. The fluxes through the interfaces on the fine grid, defined by

$$f(\mathbf{x}) = \nabla\phi(\mathbf{x}) \tag{3.23}$$

are located at the cell interfaces and denoted by $f_n$, $f_s$, $f_w$ and $f_e$, respectively. Uppercase letters $\Phi$ and $F$ are used for the same quantities on the coarse grid. To ensure conservativity, we need to have equal approximations to the flux on both grid levels,

$$f_s \stackrel{!}{=} F . \tag{3.24}$$

Since

$$F = \frac{1}{2\Delta y}(\Phi_n - \Phi_s) \tag{3.25}$$

$$f_s = \frac{1}{\Delta y}(\varphi_c - \varphi_s) \tag{3.26}$$

we get

$$\varphi_s = \varphi_c - \frac{1}{2}(\Phi_n - \Phi_s) \tag{3.27}$$

$$= \varphi_c - \Delta y F . \tag{3.28}$$

This may be seen as an equation determining the choice of the ghost-cell value $\varphi_s$ to obtain conservativity in fluxes across the coarse-fine interface, which is to be used instead of interpolation when filling the ghost-cells with data.

Since the ghost-cell value $\varphi_s$ depends on $\varphi_c$, it has to be reset (recalculated) each time $\varphi_c$ changes, i.e. after each smoothing iteration. If we store the coarse flux $F = \frac{1}{2\Delta y}(\Phi_n - \Phi_s)$ once, we just have to subtract the "net-flux" $\Delta y F$ from the center value. This treatment therefore results in Neumann-boundary conditions on the interior refined grid interfaces by forcing the fine grid fluxes to the value of the underlying coarse grid flux.

| Position | Order Dirichlet | Order Neumann |
|---|---|---|
| $L_\infty$ | 0.987 | 1.995 |
| Interface | 0.987 | 1.974 |
| Center | 1.990 | 2.060 |

**Table 3.1.**: Measured order for bilinear interpolation of Dirichlet boundaries in the ghost cells versus flux conservative interpolation of Neumann boundaries in the ghost cells.

A direct comparison of a multigrid implementation with Neumann boundary data in comparison to the standard treatment of Dirichlet boundary data in the ghost cells shows the necessity of this special treatment. With Dirichlet boundary data in the ghost cells, artificial source terms are introduced at the coarse-fine interfaces. As depicted in figure 3.8 for a test scenario, this can lead to discontinuities in the first derivative of the solution. When ensuring
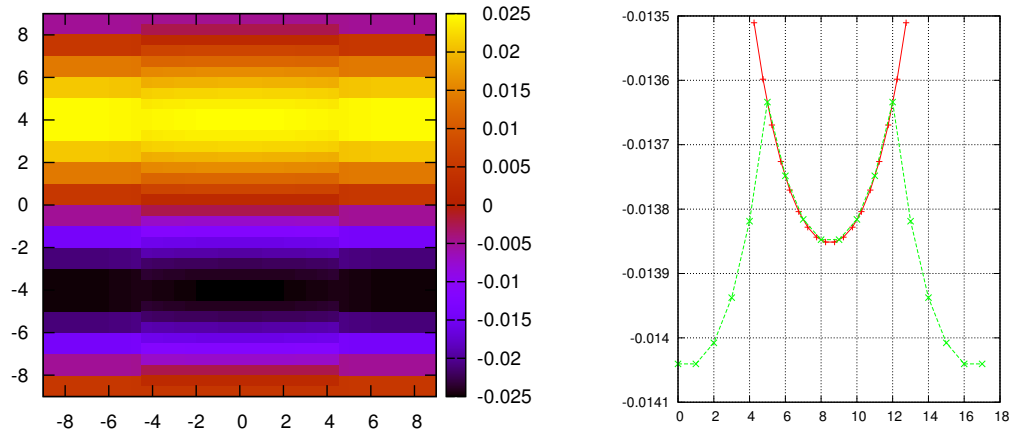
**Figure 3.8.**: Bilinear interpolation at coarse-fine interfaces for a test problem. The solution (**left**) exhibits artificial (unphysical) sources at the interfaces which lead to a discontinuity of the derivative across the interface, as visible in the cut in $x$-direction (**right**).
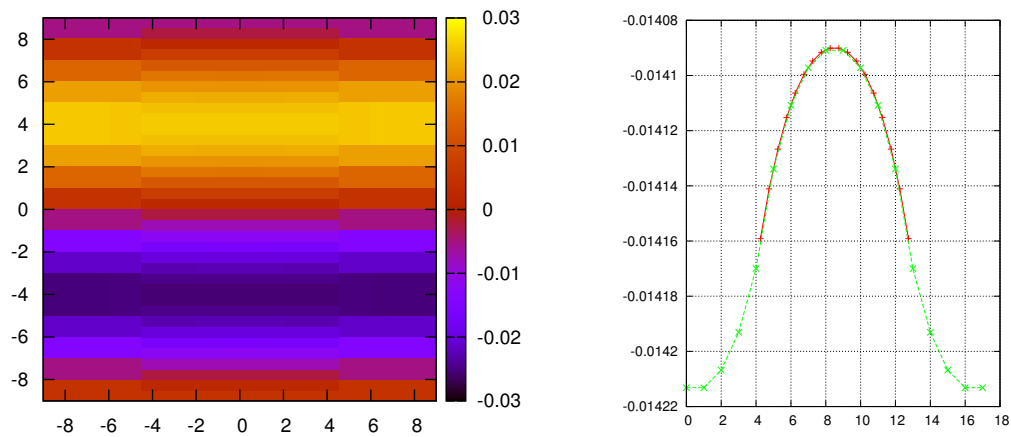


**Figure 3.9.**: Neumann conditions at coarse-fine interfaces for the same test problem. The artificial sources of the solution (**left**) at the interfaces have vanished, the derivative is continuous in the cut in $x$-direction (**right**).

flux-conservative interfaces, as visible in figure 3.9, the gradient of the potential remains smooth.

For a more quantitative comparison, the error in $L_\infty$-norm, the error at the interface and in the center of the fine region $\Omega_f$ are compared at different resolutions $n$ for both methods. The measured orders are listed in table 3.1. The spurious source terms at the interface lower the overall accuracy of the standard treatment to first order, while the flux conservative interpolation of the Neumann boundaries restores the overall accuracy to second order.

## 3.4. Diagnostics

A fundamental part of this thesis is the numerical analysis of Euler flows with regard to their geometrical properties. As will be presented in detail in chapters 4 and 5, this includes the calculation of the flow map $\mathbf{X}(\boldsymbol{\alpha}, t)$ to observe the Lagrangian evolution of physical quantities, such as pressure derivatives and the knowledge of the back-to-labels map $\mathbf{A}(\mathbf{x}, t)$ to compute the origin of Lagrangian fluid elements. Furthermore, several blowup criteria involve the integration of vortex lines (as introduced in section 2.2.4) and the computation of their geometric properties, such as their length or curvature.

Monitoring all these quantities on-the-fly in a simulation poses a challenge for the diagnostics. The following paragraphs will outline the technical and numerical details associated with the measurement of Lagrangian and geometric quantities.

### 3.4.1. Tracer particles

Knowledge of the flow map $\mathbf{X}(\boldsymbol{\alpha}, t)$ and its inverse $\mathbf{A}(\mathbf{x}, t)$ is gained in the numerical simulation with the help of passive tracer particles. These passive tracer particles $\mathbf{x}(t)$ obey the equation

$$\mathbf{x}(0) = \mathbf{x}_0 \tag{3.29}$$
$$\dot{\mathbf{x}}(t) = \mathbf{u}(\mathbf{x}(t), t) \tag{3.30}$$

without influencing the flow in any way. In *racoon III*, this is implemented using exactly the same integration method that is in use for the time integration of the field data (a third-order strong stability preserving Runge-Kutta by [88]). To ensure the correct coupling between the velocity field and the particle position, the particle positions are updated using the temporary field data from a Runge-Kutta sub-step. Interpolating the field data to the particle positions is achieved using a tri-linear interpolation.

The back-to-labels map $\mathbf{A}(\mathbf{x}, t)$ is implemented in a rather cost-intensive way: A precursory simulation is run with a huge number of tracer particles. Using
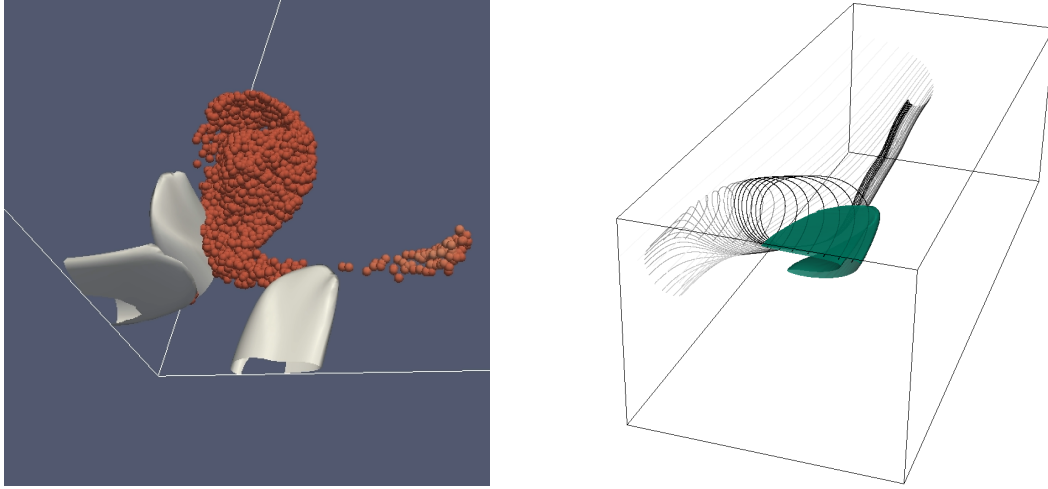
**Figure 3.10.**: Sketch of the geometric diagnostics introduced into *racoon III*. **Left:** Back-to-labels map. Origin of the fluid elements that will add up to a cuboid around the maximum vorticity at late time. **Right:** Lagrangian evolution of a vortex line at different times.

this dataset, positions at late times can be mapped back to their origin. In a subsequent production run with identical parameters, the fluid volume that will arrive at the target point at later times is known from the beginning. Figure 3.10 (left) depicts this strategy: Shown is every 10000th fluid particle that will arrive in a cuboid around the position of maximum vorticity at late times.

### 3.4.2. Field lines

The computation of vortex lines looks similar to the advection of tracer particles. As defined in section 2.2.4, a vortex line is a curve $c(s)$ that fulfills the equation

$$c(0) = \mathbf{x}_0 \tag{3.31}$$
$$\dot{c}(t) = \boldsymbol{\omega}(c(t), t) \,. \tag{3.32}$$

For applicability, the vorticity direction vector field $\boldsymbol{\xi}(c(t), t)$ can be used instead of the vorticity $\boldsymbol{\omega}(c(t), t)$ to obtain a curve $c(s)$ parametrized by arc length. The integration is carried out using a third-order Runge-Kutta integrator in space, interpolation to the field line is again tri-linear. Figure 3.10 (right) pictures the Lagrangian evolution of a vortex line for the vortex dodecapole flow for different times.

When having obtained a curve $c(s)$, its curvature could in principle be computed by

$$\kappa \mathbf{n} = \ddot{c}(s) \,. \tag{3.33}$$

This approach, while analytically correct, relies on the second derivative of the integral curve. This may be omitted by realizing

$$\kappa\mathbf{n} = \frac{\partial \dot{c}(s)}{\partial s} \tag{3.34}$$

$$= \frac{\partial \boldsymbol{\xi}}{\partial s} \tag{3.35}$$

$$= (\boldsymbol{\xi} \cdot \nabla)\boldsymbol{\xi} \, . \tag{3.36}$$

As a result, the curvature of vortex lines is available as a vector field in the whole domain. Its absolute value can be interpolated to the curve at any point to get an approximation to the vortex line curvature. As a side effect, quantities like the maximum curvature of all vortex lines are in reach without having to integrate any vortex line at all.

## 3.5. Parallelization and high performance computing

Due to the serious requirements in terms of resolution, the simulations conducted in the context of this work need a large amount of memory. To comply with this demand, the framework *racoon* allows for the usage of multiple interconnected machines in parallel. The employment of adaptively refined grids considerably complicates the process of parallelization, which is countered by the dynamic load balancing technique presented in section 3.1.4.

Yet, the massive number of processors that is necessary to reach ever higher resolutions is connected with a number of problems that exceed the scope of simple parallel programming, most notably the metadata problem, parallel data output, parallel scaling and the parallelization of the elliptic solver. The following sections will briefly comment on the encountered problems and the choice of solutions in *racoon* to fulfill the requirements of high performance computing.

### 3.5.1. Metadata and the hybrid approach

For small problems, parallel computing is achieved by having multiple cores act on the same memory (symmetric multiprocessor, SMP). In contrast to this, massively parallel computers consist of a large number of independent compute nodes (massively parallel processors, MPP) and rely on an interconnecting network for communication. Modern supercomputers usually combine SMP and MPP techniques by providing a large number of nodes with more than one core each.

Even though in the process of parallelization the bulk of computational data is split among the processors to be operated on in parallel, certain information

have to be stored by each process. The largest portion of this *metadata* contains information about the overall grid structure. For boundary exchanges, tracer particle communication and rebalancing on refinement, each processor relies on this data to determine the target process to communicate with. For parallel computing with hundreds of processors, this metadata is small ($\approx$ 1MB) compared to the actual field-data, but as the number of blocks increases, it grows to a considerable portion of the available system memory.

To counter this problem, *racoon III* was updated to employ a hybrid approach for the memory layout. Instead of spawning one process per core, only one process per node is generated. This process forks during the computationally expensive parts of the calculation to utilize all cores of the node. With this method, the metadata is stored only once per node instead of once per core and a larger overall number of blocks is possible.

## 3.5.2. Parallel I/O

When the number of independent processes exceeds several thousand, the input and output of field data becomes more complex. It is no longer a possibility that each process dumps his own fragment of the computational domain in a separate file. In most file-systems (even parallel ones), file creation is a serial process and the simultaneous creation of several thousand files may take several minutes. Furthermore, the handling of thousands of files in post-processing is a time consuming process.

In principle, the MPI-standard defines methods for parallel I/O operations. Yet, in *racoon*, the distribution of data across the memory is relatively complex due to the logical octree and the Hilbert-curve for load balancing. A straightforward implementation of MPIIO would rely on many separate collective calls for MPIIO and therefore not increase the performance. To find the optimal strategy, several different approaches for parallel I/O have been compared. This includes:

**PLAIN** Each process writes its data into a single, separate file. This was the previously used system in *racoon*.

**MPI_WRITE** Only one file is created for all processes. Each process writes its portion via `MPI_File_write` in parallel.

**MPI_WRITE_ALL** Again, only one file is created. The parallel writing is implemented via `MPI_File_write_all` as a collective operation.

**PSETS** Via "Psets", each I/O node, responsible for 512 compute nodes, creates a file. Output is realized in parallel across processes sharing the same I/O node.

With these competing methods for parallel I/O, tests have been conducted for different cases, to simulate production behavior:

1. Each process writes a large, continuous chunk of data (8MB per process). This emulates output of field data for a coherent distribution in memory.

2. Each process writes a small, continuous chunk of data (128 Byte). This test mimics the output of small diagnostic data like e.g. tracer particles.

3. Each process writes a large amount of data (16MB), but segmented into 16 or 256 parts. This approximates the behavior of *racoon*, since the field data is distributed among different blocks.

| #core | 2048 | 4096 | 8192 | 16384 |
|---|---|---|---|---|
| Duration (s) | | | | |
| PLAIN | 137.5 | 235.2 | 288 | 832 |
| HPC-IO | 100.9 | 57.6 | 50.3 | 37.5 |
| Bandwidth (MB/s) | | | | |
| PLAIN | 596.5 | 348.7 | 284.7 | 98.58 |
| HPC-IO | 812.9 | 1423.9 | 1630.6 | 2187.12 |

**Table 3.2.**: Hard scaling of parallel I/O for *racoon* in a production run with $1024^3$ grid points (82017MB of data). The improved parallel output method outperforms the old method by a factor of $\approx 20$.

| #core | 64 | 512 | 4096 | 16384 | 32768 |
|---|---|---|---|---|---|
| resolution | $256^3$ | $512^3$ | $1024^3$ | $1024^3$ | $2048^3$ |
| data (MB) | 1285 | 10252 | 82017 | 82017 | 655457 |
| Duration(s) | | | | | |
| PLAIN | 7.5 | 25 | 235.2 | 832 | − |
| HPC-IO | 6.6 | 16.5 | 57.6 | 37.5 | 169 |
| Bandwidth (MB/s) | | | | | |
| PLAIN | 171.3 | 410.08 | 348.7 | 98.58 | − |
| HPC-IO | 194.7 | 621.33 | 1423.9 | 2187.12 | 3869.3 |

**Table 3.3.**: Weak scaling of parallel I/O for *racoon* in a production run. Resolutions of $2048^3$ grid points are possible. The peak bandwidth was measured at $\approx 3.9$GB/s.

These tests were performed with 64 to 32768 cores (1 to 64 I/O nodes on JUGENE). The results can be summarized as follows:

- For large datasets, the PSET-method performs and scales well. Collective MPI_WRITE by far outperforms the non-collective variant. The PLAIN-method works surprisingly well.

- For small datasets, `PSET` and collective MPIIO still perform best. The `PLAIN`-method cannot compete due to the large overhead of creating a huge number of files synchronously.

- For fragmented data, both collective and standard MPIIO performs poorly, due to large overhead of calling the MPI-routines. The `PSET` performs well again.

Using these results, the high performance I/O for *racoon III* was designed. Even though the `PSET`-methods work best in all test cases, its implementation would mean significant programming effort. Furthermore, its implementation is machine specific and available only for IBM BlueGene machines. The alternative solution therefore was to buffer the data before the output operation and then output it as a continuous block via collective MPIIO. The increase in performance for production runs is depicted in tables 3.2 and 3.3. Instead of a decrease in bandwidth for a larger number of cores, the output now scales close to optimal. For 16384 cores, a speedup of factor 22 is achieved. Higher numbers of processors, which were unreachable before, now scale well. A peak bandwidth of 3.9 GB/s is reached.

### 3.5.3. Scaling

Combining the above mentioned improvements for parallel computing, the overall scaling for *racoon* is depicted in figure 3.11. It is measured on the BlueGene/P machine at Forschungszentrum Jülich with a total number of 294912 cores. For a combination of weak and hard scaling, the performance is close to linear up to 262144 cores, the maximum number tested. Note, however, that this scaling is just valid for hyperbolic problems. Extensions for the elliptic part and their impact on parallel scaling are discussed in the following section.

### 3.5.4. Parallelization and multigrid

Special care has to be taken when parallelizing elliptical solvers in the context of the framework *racoon*. The elliptical problems encountered when simulating the Euler equations (velocity projection or calculation of the vector potential) are more difficult to parallelize than the hyperbolic advection term due to their inherent non-local nature. For each timestep, information travels only fractions of the grid spacing in the advection step, but through the whole domain when enforcing the incompressibility. This behavior is necessarily reflected by the demands on communication between processes in massively parallel simulations.

A central part of the multigrid algorithm presented in section 3.3 is the exchange of information between different grid levels. Since, due to arbitrary load balancing on adaptively refined grids, blocks of different levels may be stored
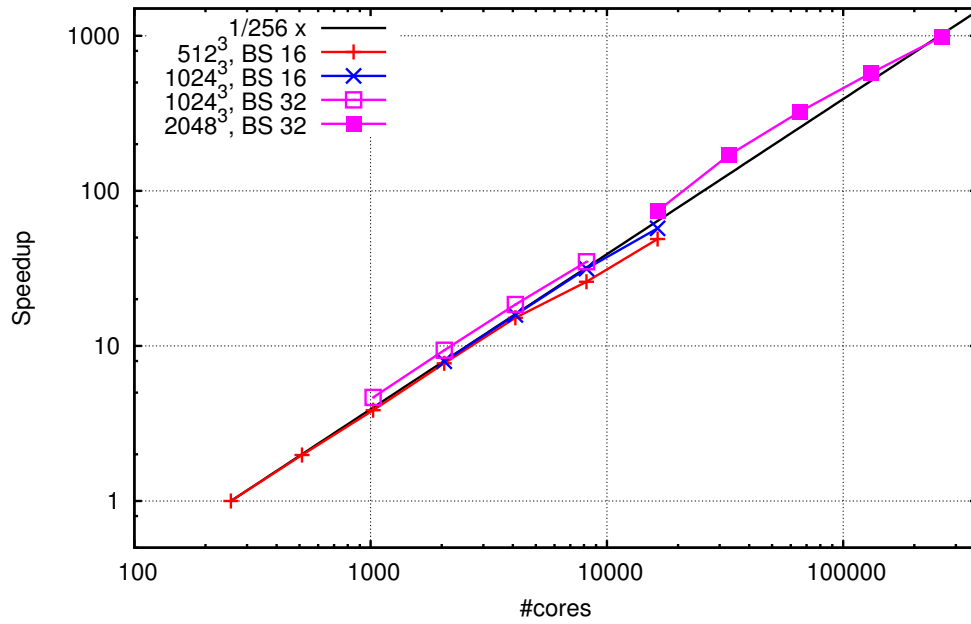
**Figure 3.11.**: Mixed weak and hard scaling for the framework *racoon* for a hyperbolic test problem. The scaling is close to linear for up to 262144 cores.
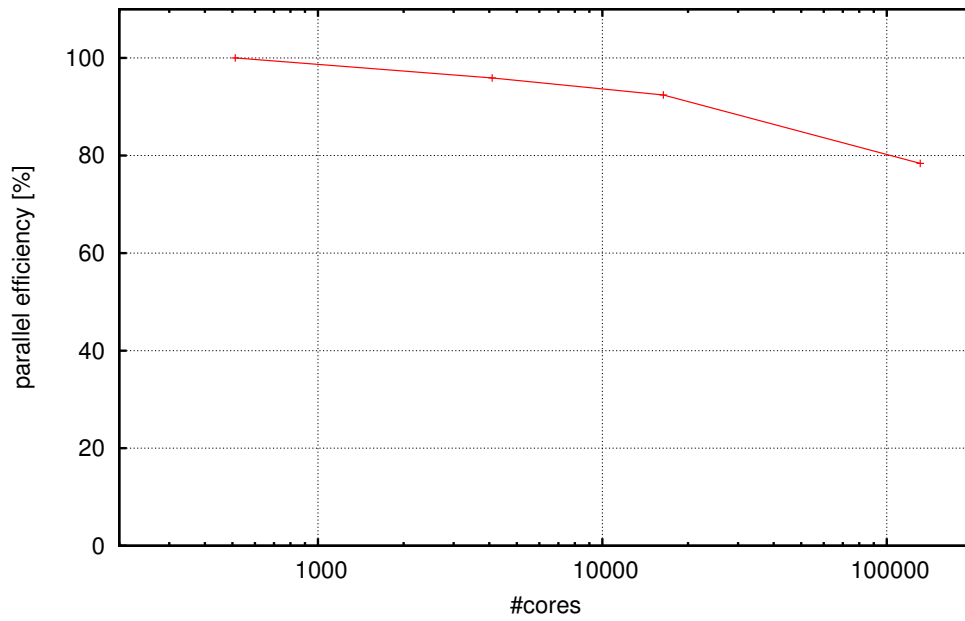


**Figure 3.12.**: Parallel efficiency of the redesigned multigrid algorithm for *racoon III*. Satisfying efficiency is reached with up to 131072 cores with a constant load per core.

on different processes, inter-grid communication may occur in the prolongation and restriction phases of the algorithm. Quite in the contrast to the hyperbolic part, this implies exchange of entire block volumes instead of just boundary data.

Furthermore, in the current implementation of multigrid in *racoon*, the coarsest level is formed by the coarsest block, spanning the entire domain. On this block (usually $16^3$ grid cells), the Poisson equation is solved via Gauss-Seidel iterations. Since only one process gets to handle the coarsest block, this part of the algorithm does not parallelize (with the exception of the SMP as part of the hybrid approach presented in the previous section). This could be countered by decreasing the blocksize, yet smaller blocksizes result in a higher block count, which in turn increases the metadata. Hence, a careful adjustment of the blocksize has to be made, which will result in suboptimal scaling properties in comparison to the purely hyperbolic case.

Figure 3.12 shows the scaling behavior of *racoon III* with multigrid algorithm, obtained with the IBM BlueGene/P of Forschungszentrum Jülich. The scaling is satisfying up to at least 131072 cores, even though efficiency begins to drop at the highest tested number of processes.

## 3.6. Conclusion

A considerable amount of programming was necessary to modify the presented framework to be fit to perform massively parallel high resolution simulations of the Euler equation. This includes numerical issues such as a discretization and a scheme which allow for the efficient use of adaptively refined grids without sacrificing accuracy in the primary variable, or the modification of the multigrid algorithm to produce reliable results on refined meshes. New diagnostics had to be developed, in particular Lagrangian tracer particles to measure the flow map, as well as vortex line integration and the computation of their curvature, length and line integral quantities. Furthermore, technical issues had to be solved, most notably the extreme demands posed by the massively parallel computation, concerning both scalability issues as well as parallel output. Especially the resulting parallel adaptive multigrid algorithm shows an impressive performance.

The resulting program for integrating the Euler equations has been used for every production simulation presented in this work. It was run on the IBM BlueGene/P machine "JUGENE" of Forschungszentrum Jülich made available through project HBO35

# 4. Analysis of Finite-time Singularities

In chapter 2, the Euler equations were defined and their physical properties were discussed. This chapter is devoted to the question: Given initial conditions $\mathbf{u}_0(\mathbf{x})$ of some regularity, does there exist a unique regular solution $\mathbf{u}(\mathbf{x}, t)$ to the Euler equations for all times, or does the solution become singular in finite time? Up to now, this question is not answered. Nevertheless, there has been a lot of progress in identifying the mechanisms that may lead to a finite-time singularity. From this knowledge, criteria are developed to expose necessary conditions for the formation of a singularity. Some of these will be presented in this chapter, with a focus on criteria whose assumptions are verifiable by numerical computations.

First, in section 4.1, mathematical preliminaries are given for analyzing Euler flows. Analytical results regarding criteria for the formation of finite-time singularities are presented and fundamental concepts such as the notion of energy estimates are introduced. From here, classical results like the well-known Beale-Kato-Majda criterion for vorticity accumulation are a small step.

Section 4.2 focuses on Lagrangian and geometric criteria, which provide analytical results regarding the blowup of the Euler equations with the help of geometrical properties of the flow. This mainly focuses on the regularity of the direction of vortex lines, the breakdown of their curvature or their smooth alignment. The assumptions of these criteria are analyzed with respect to their applicability to numerical simulations.

## 4.1. Existence of Solutions

### 4.1.1. Energy methods

A classic approach to obtaining estimates for partial differential equations is via *energy methods*. Energy methods derive their name from the a priori bound on $\|\mathbf{u}\|_{L^2}$, which is equivalent to the conservation of kinetic energy introduced in section 2.2.3. In a similar way, by defining other Sobolev-norms of the velocity or compound objects, other a priori estimates are gained which may be used to serve as starting points for further proofs.

Energy methods can be used to prove the existence of global solutions for the two dimensional Euler equations (established by Kato [50]) as well as the local in time existence of solutions for the three-dimensional Euler equations (e.g. [34] in Eulerian formulation, [51] in Lagrangian formulation, [24] in active vector formulation). This is done for example by first proving the existence of approximate solutions via a mollification procedure and proving adequate energy estimates for these solutions, then passing to the limit of solutions to the actual, non-approximate equation. The convergence to a limiting solution is possible at least on the time interval $[0, T]$, where $T$ depends on the initial conditions only. More precisely, following [72], the resulting statement is:

*For initial conditions* $\mathbf{u}_0 \in H^m$, $\nabla \cdot \mathbf{u}_0 = 0$, $m \geq \frac{7}{2}$, *there exists a time $T$ with the rough upper bound*

$$T \leq \frac{1}{c\|\mathbf{u}_0\|_{H^m}} \,, \tag{4.1}$$

*such that there exists a unique solution to the Euler equations*

$$\mathbf{u} \in C([0, T]; C^2(\mathbb{R}^3)) \cap C^1([0, T]; C(\mathbb{R}^3)) \,. \tag{4.2}$$

Further control over the $H^m$-norm of the velocity would then allow the continuation in time of the above solution. Most of the blowup criteria presented in the following sections are based on this result.

Now, suppose that for a given initial condition the existence of a smooth solution global in time is known. Energy methods can then be used to prove the uniqueness of this solution. This is done by considering two different solutions $\mathbf{u}_1$ and $\mathbf{u}_2$ and taking the $L^2$-norm of the difference of their evolution equations. The resulting energy identity can be bounded via Grönwall's lemma to obtain an upper bound on $\|\mathbf{u}_2 - \mathbf{u}_1\|_{L^2}$ in time. This bound is equal to zero if the initial difference $\| (\mathbf{u}_2 - \mathbf{u}_1)|_{t=0} \|_{L^2}$ is zero and the solution remains smooth. Therefore, globally smooth solutions to the Euler equation are unique.

## 4.1.2. Beale-Kato-Majda criterion

By means of the energy methods presented in section 4.1.1 it can be shown that the three-dimensional Euler equations possess unique strong solutions $\mathbf{u} \in C([0, T]; C^2(\mathbb{R}^3)) \cap C^1([0, T]; C(\mathbb{R}^3))$ locally in time for given initial conditions,

$$\mathbf{u}_0 \in \{\mathbf{u} \in H^m \,|\, \nabla \cdot \mathbf{u} = 0\}, \tag{4.3}$$

for $m \geq \frac{7}{2}$ and may be continued in time provided that the $H^m$-norm of the velocity remains bounded.

An important turning point in the history of analysis for the three-dimensional Euler equations was the proof of a connection between smooth global solutions

and the accumulation of vorticity by Beale et al. [3]. This was achieved by linking the supremum of the $H^m$-norm of the velocity on a time interval $[0, T]$ to an a priori bound on the $L^1([0, T], L^\infty(\mathbb{R}^3))$-norm of vorticity and deducing global in time existence of smooth solutions. More specific, the theorem states:

**Beale-Kato-Majda (BKM):** *If for any $T > 0$ there exists a constant $C$ such that the vorticity $\boldsymbol{\omega} = \nabla \times \mathbf{u}$ fulfills*

$$\int_0^T \|\boldsymbol{\omega}(\cdot, t)\|_{L^\infty} \mathrm{d}t \leq C, \tag{4.4}$$

*then $\mathbf{u}$ is a strong global solution to the three-dimensional Euler equations.*

*If on the other hand $T$ is the maximal time of existence of a strong solution to the Euler equations, then*

$$\int_0^T \|\boldsymbol{\omega}(\cdot, t)\|_{L^\infty} \mathrm{d}t = \infty. \tag{4.5}$$

For the three-dimensional Euler equations, this criterion is one of the sharpest results known. A similar result has been proven concerning the blowup of the strain rate instead of the vorticity by Ponce [85].

As these results give a clear distinction, at least in principle, between a singular development and a mere fast accumulation of vorticity, it has been applied a lot in the context of numerical simulations of the Euler equations. In practice this means: A measured growth of the maximum vorticity in time of

$$\|\boldsymbol{\omega}(\cdot, t)\|_{L^\infty} \approx \frac{1}{(T - t)^\gamma}, \tag{4.6}$$

for a supposed blowup time $T$ and some exponent $\gamma$ specifying the growth rate leads to a finite-time singularity at time $t = T$ only if $\gamma \geq 1$. For $\gamma < 1$ the observed accumulation of vorticity has to be a numerical artifact. The critical case, $\gamma = 1$, seems to be the common case in most numerical simulations.

Given the evolution of the maximum vorticity in time, $\Omega(t) = \|\boldsymbol{\omega}(\cdot, t)\|_{L^\infty}$, acquired from a numerical simulation, and making the assumption $\gamma = 1$, a plot of $1/\Omega(t)$ against time $t$ can be compared to a line and extrapolated. The zero-crossing of the line gives an estimate for the time $T$ of the blowup. Curves of $1/\Omega(t)$ that agree well with this behavior have been taken as numerical evidence for a finite-time singularity (e.g. Bell and Marcus [4], Grauer et al. [43], Kerr [52], Orlandi and Carnevale [80]).

It is well established in literature (see e.g. Gibbon [39] for an overview) that both a huge amount of resolution of the region of maximum vorticity as well as a simulation up to very close to the singular time are necessary to distinguish

between a critical accumulation and just a "very fast" accumulation of $\Omega(t)$. Because of that, much care is required when applying this theorem to numerical simulations.

## 4.2. Geometric and Lagrangian blowup criteria

The above presented results for the development of a finite-time Euler singularity have in common that they focus on global features (such as certain norms of the velocity or the vorticity fields) or on point-wise Eulerian features (such as $\Omega(t)$) of the flow. This comes at the disadvantage of neglecting the structures and physical mechanisms of the flow evolution. A strategy to overcome such shortcomings was established by focusing more on geometrical properties and flow structures, such as vortex tubes or vortex lines. Starting with the works of Constantin [23], Constantin et al. [28], Cordoba and Fefferman [29], some of these "geometric" criteria (e.g. [30, 38, 40]) have reached a phase where they allow direct verification of their assumptions with the help of numerical simulations.

The following section will introduce these developments, starting with results concerning the regularity of the direction of vorticity and the twisting and bending of vortex tubes. Special focus is placed on the criteria presented by Deng et al. [30, 31], as the assumptions are in close reach for numerical simulations. They examine the Lagrangian evolution of vortex line segments and formulate a combined bound on velocity blowup and vortex segment collapse.

### 4.2.1. Classical geometric blowup criteria

One of the consequences of the BKM theorem introduced in section 4.1.2 is the trivial consequence that no blowup can occur for the two dimensional Euler equations. Since the vorticity $\boldsymbol{\omega}(\mathbf{x}, t)$ is bounded by the initial conditions $\|\boldsymbol{\omega}_0\|_{L^\infty}$ for all times, a critical accumulation such as needed in (4.5) is impossible.

This is a direct consequence of the vorticity pointing out of the plane of motion, therefore having the vortex-stretching term $\boldsymbol{\omega} \cdot \nabla \mathbf{u}$ vanish everywhere. This may be interpreted as a motivation to focus on the behavior of the direction of vorticity, $\boldsymbol{\xi} = \boldsymbol{\omega}/|\boldsymbol{\omega}|$ in the three-dimensional case. For 2D, $\boldsymbol{\xi}$ is a constant in space and time (modulo sign). In 3D, the consequences of the regularity of $\boldsymbol{\xi}$ on the growth-rate of vorticity and ultimately of the applicability of BKM can be precisely stated.

**Smoothly directed vorticity**

For the Euler equations, this was introduced by Constantin et al. [28]. They state, roughly, that for a smoothly directed vorticity in an $O(1)$-region there may be no blowup in finite time as long as the velocity remains finite in this region.

More specific, for a solution to the Euler equation that remains smooth for all $0 \leq t < T$ consider a set $W_0 \subset \mathbb{R}^3$ of points of non-vanishing vorticity and its Lagrangian image

$$W_t = \{\mathbf{X}(q, t) | q \in W_0\}. \tag{4.7}$$

This region is said to be *smoothly directed*, if there is a $\rho > 0$ and $0 < r < \frac{\rho}{2}$ such that

- the direction of vorticity is well behaved around the considered region,

$$\lim_{t \to T} \sup_{q \in W_0} \int_0^t \|\nabla \boldsymbol{\xi}(\cdot, t)\|_{L^\infty(B_{4\rho}(\mathbf{X}(q,t)))} \mathrm{d}t < \infty, \tag{4.8}$$

- the region is large enough to capture the local intensification of vorticity,

$$\sup_{B_{3r}(W_t)} |\boldsymbol{\omega}(\mathbf{x}, t)| \leq m \sup_{B_r(W_t)} |\boldsymbol{\omega}(\mathbf{x}, t)| \tag{4.9}$$

for $m \geq 0$ constant and

- the velocity is bounded around the considered region,

$$\sup_{B_{4\rho}(W_t)} |\mathbf{u}(\mathbf{x}, t)| \leq U \tag{4.10}$$

for $U \geq 0$ constant.

In a smoothly directed region, the vorticity remains bounded in time and no blowup can exist.

Even though this criterion takes into account the local structure of the flow and follows the evolution of vortex lines, the (global) bound on the velocity makes this theorem hard to apply in practice. Numerical simulations of the Euler equations give no evidence for the velocity to be uniformly bounded in time.

**Twisting and bending of vortex tubes**

This restriction on the velocity field is weakened in a similar criterion by Cordoba and Fefferman [29]. They consider vortex tubes, as introduced in section 2.2.4, with some properties concerning their regularity and a surrounding $O(1)$ region

$Q$ of the flow. From this it is possible to deduce, with the help of a milder assumption on the surrounding velocity, that the vortex tube cannot reach zero thickness in finite time. In detail they state:

**Cordoba-Fefferman:** *Let $W_t \subset Q$ be a regular tube that moves with the flow. If*

$$\int_0^T \sup_{x \in Q} |\mathbf{u}(\mathbf{x}, t)| \mathrm{d}t < \infty \tag{4.11}$$

*then the tube cannot shrink to zero thickness,*

$$\liminf_{t \to T} \mathrm{Vol}(W_t) > 0. \tag{4.12}$$

Even though the velocity field is no longer required to be uniformly bounded in time, the notion of "regular tube" of $O(1)$ length is too restricting, compared to the experiences of numerical simulations.

## 4.2.2. Regularity of vorticity direction along a vortex line

It has been shown in section 2.2.4 that for the three-dimensional Euler equations vortex lines, defined as integral curves of the vorticity direction field, are transported with the flow. As a consequence, two points $x$ and $y$ on the same vortex line $c(s)$ stay on the same vortex line for all times.

It was furthermore shown, as a direct implication of the solenoidality of the vorticity vector field, that the vorticity flux through a vortex tube is the same for each cross-section.

These two arguments may be combined to get a differential notion of the connection between the vorticity at two different points on the same vortex line. Starting at the solenoidality of $\boldsymbol{\omega}$,

$$0 = \nabla \cdot \boldsymbol{\omega} = \nabla \cdot (\boldsymbol{\xi} \, |\boldsymbol{\omega}|) \tag{4.13}$$
$$= (\boldsymbol{\xi} \cdot \nabla)|\boldsymbol{\omega}| + |\boldsymbol{\omega}|(\nabla \cdot \boldsymbol{\xi}) \tag{4.14}$$

which results in

$$(\boldsymbol{\xi} \cdot \nabla)|\boldsymbol{\omega}| = -|\boldsymbol{\omega}|(\nabla \cdot \boldsymbol{\xi}) \, . \tag{4.15}$$

Since for a vortex line $c(s)$ it holds by definition that $\dot{c}(s) = \boldsymbol{\xi}(c(s))$, we have $\boldsymbol{\xi} \cdot \nabla \equiv \partial/\partial s$, where $\partial/\partial s$ is the partial derivative in direction of the vortex line. Thus, we arrive at the ODE for $|\boldsymbol{\omega}|$ along a vortex line:

$$\frac{\partial |\boldsymbol{\omega}|}{\partial s} = -|\boldsymbol{\omega}|(\nabla \cdot \boldsymbol{\xi}) \tag{4.16}$$

which yields, upon integration,

$$|\boldsymbol{\omega}(\mathbf{y}(t),t)| = |\boldsymbol{\omega}(\mathbf{x}(t),t)| \exp\left(-\int_{\mathbf{x}(t)}^{\mathbf{y}(t)} \nabla \cdot \boldsymbol{\xi} \mathrm{d}s\right). \qquad (4.17)$$

Paraphrased, this means: The vorticity at two different points on the same vortex line is connected by the amount of converging or diverging of neighboring vortex lines along their interconnecting path. The more violent vortex lines converge around a vortex line, the faster the vorticity grows along that line.

This finding was connected with BKM by Deng et al. [30] to formulate a geometric blowup criterion. It is obvious from equation (4.17) that the maximum vorticity $\Omega(t)$ at a given time $t$ can be estimated by the vorticity on its vortex line, as long as $\nabla \cdot \boldsymbol{\xi}$ remains finite. In detail this means:

**Deng-Hou-Yu theorem 1:** *Let $\mathbf{x}(t)$ be a family of points such that for some $c_0 > 0$ it holds $|\omega(\mathbf{x}(t),t)| > c_0\Omega(t)$. Assume that for all $t \in [0,T)$ there is another point $\mathbf{y}(t)$ on the same vortex line as $\mathbf{x}(t)$, such that the direction of vorticity $\boldsymbol{\xi}(\mathbf{x},t) = \omega(\mathbf{x},t)/|\omega(\mathbf{x},t)|$ along the vortex line $c(s)$ between $\mathbf{x}(t)$ and $\mathbf{y}(t)$ is well-defined. If we further assume that*

$$\left| \int_{\mathbf{x}(t)}^{\mathbf{y}(t)} (\nabla \cdot \boldsymbol{\xi})(c(s),t) \, \mathrm{d}s \right| \leq C \qquad (4.18)$$

*for some absolute constant $C$, and*

$$\int_0^T |\omega(\mathbf{y}(t),t)| \, \mathrm{d}t < \infty; , \qquad (4.19)$$

*then there will be no blowup up to time $T$.*

It is immediately clear how this criterion can be applied to numerical simulations. If the maximum vorticity $\Omega(t)$ exhibits fast growth in time for which it is hard to decide whether it is a finite-time blowup compatible with BKM, instead one could monitor the vorticity outside the critical region, but on the same vortex line. If it remains well bounded, and $\nabla \cdot \boldsymbol{\xi}$ along the vortex line does not scale critically in time, it is safe to deduce a non-critical growth of $\Omega(t)$.

A reasoning along these lines was brought forth in [30] to exclude a finite-time singularity for Kida-Pelz initial conditions. This argument was tested and put in doubt on the basis of numerical simulations presented in this thesis in section 5.4.4. Still, the insight provided by the theorem could successfully be used to distinguish between different scenarios of finite-time blowups.

### 4.2.3. Vortex line stretching and vorticity accumulation

Vortex stretching was recognized in section 2.2.4 as the mechanism responsible for the accumulation of vorticity. Revisited from a geometric point of view, vortex lines are transported with the flow, yet twist and turn due to vortex stretching. Since in the absence of dissipation vortex lines are unable to reconnect, the topological properties of vortex lines are fixed. A complex flow will therefore entangle, stretch and twist vortex lines in a non-trivial way.

The geometric equivalent of the vortex stretching term is the increase in length for a Lagrangian vortex line. It is possible to quantify this stretching and establish a sound connection to the vorticity dynamics of the flow. This in turn can then be used to reformulate blowup criteria in terms of geometric constraints on Lagrangian vortex lines. This section is meant to give an overview over this procedure to lay the foundations of the second theorem of Deng et al. [30].

Consider a vortex line segment $L_0$ at time $t = 0$ and its Lagrangian image $L_t = \mathbf{X}(L_0, t)$. Let $\beta$, $s$ be the arc length parameters of $L_t$ at times 0 and $t$. Also, note that for a point $\alpha$ on $L_0$

$$\boldsymbol{\xi}(\mathbf{X}(\alpha, t), t) = \frac{\partial \mathbf{X}(\alpha, t)}{\partial s} \tag{4.20}$$

for any time $t$ and in particular

$$\boldsymbol{\xi}_0(\alpha) = \frac{\partial \alpha}{\partial \beta} \tag{4.21}$$

at $t = 0$.

Now, starting at the vorticity transport formula (2.41), the evolution of the absolute vorticity at a Lagrangian fluid element becomes

$$
\begin{aligned}
|\boldsymbol{\omega}(\mathbf{X}(\alpha, t), t)| &= \boldsymbol{\xi}(\mathbf{X}(\alpha, t), t) \cdot \boldsymbol{\omega}(\mathbf{X}(\alpha, t), t) \\
&= \boldsymbol{\xi}(\mathbf{X}(\alpha, t), t) \cdot \nabla_\alpha \mathbf{X}(\alpha, t) \cdot \boldsymbol{\xi}_0(\alpha) |\boldsymbol{\omega}_0(\alpha)| \\
&= \frac{\partial \mathbf{X}(\alpha, t)}{\partial s} \cdot \nabla_\alpha \mathbf{X}(\alpha, t) \cdot \frac{\partial \alpha}{\partial \beta} |\boldsymbol{\omega}_0(\alpha)| \\
&= \frac{\partial \mathbf{X}(\alpha, t)}{\partial s} \cdot \frac{\partial \mathbf{X}(\alpha, t)}{\partial \beta} |\boldsymbol{\omega}_0(\alpha)| \\
&= \left( \frac{\partial \mathbf{X}(\alpha, t)}{\partial s} \cdot \frac{\partial \mathbf{X}(\alpha, t)}{\partial s} \right) \frac{\partial s}{\partial \beta} |\boldsymbol{\omega}_0(\alpha)| \\
&= \frac{\partial s}{\partial \beta} |\boldsymbol{\omega}_0(\alpha)|
\end{aligned}
$$

which results in

$$\frac{\partial s}{\partial \beta} = \frac{|\boldsymbol{\omega}(\mathbf{X}(\alpha, t), t)|}{|\boldsymbol{\omega}_0(\alpha)|} \, , \tag{4.22}$$

meaning that the local stretching of the length of a vortex line segment that is transported with the flow is equivalent to the growth of vorticity at the corresponding transported fluid element.

This result can be transformed into a bound for the length of a vortex line by the vorticity along this line. Denote with $l(t)$ the length of the vortex line segment $L_t$ at time $t$ and define with

$$\Omega_L(t) := \|\boldsymbol{\omega}(\cdot, t)\|_{L^\infty(L_t)} \tag{4.23}$$

the maximum vorticity on the vortex line segment. Furthermore, let

$$M(t) := \max(\|\nabla \cdot \boldsymbol{\xi}\|_{L^\infty(L_t)}, \|\kappa\|_{L^\infty(l_t)}) \tag{4.24}$$

be the quantity of vortex line convergence $\nabla \cdot \boldsymbol{\xi}$ and vortex line curvature $\kappa$, and define $\lambda(L_t) := M(t)l(t)$. Then, the relative increase of the length of the vortex line segment in a time interval, $l(t)/l(0)$, is bounded as

$$e^{-\lambda(L_t)} \frac{\Omega_l(t)}{\Omega_l(0)} \leq \frac{l(t)}{l(0)} \leq e^{\lambda(L_0)} \frac{\Omega_l(t)}{\Omega_l(0)} . \tag{4.25}$$

Proof:

(i)

$$
\begin{aligned}
l(t) &= \int\limits_{\beta_1}^{\beta_2} s_\beta \mathrm{d}\beta = \int\limits_{\beta_1}^{\beta_2} \left| \frac{\boldsymbol{\omega}(\mathbf{X}(\alpha, t), t)}{\boldsymbol{\omega}_0(\alpha)} \right| \mathrm{d}\beta \\
&\leq \int\limits_{\beta_1}^{\beta_2} \frac{\Omega_l(t)}{e^{-\lambda(L_0)}\Omega_l(0)} \mathrm{d}\beta = e^{\lambda(L_0)} \frac{\Omega_l(t)}{\Omega_l(0)} l(0) .
\end{aligned}
$$

(ii)

$$
\begin{aligned}
l(t) &= \int\limits_{\beta_1}^{\beta_2} s_\beta \mathrm{d}\beta = \int\limits_{\beta_1}^{\beta_2} \left| \frac{\boldsymbol{\omega}(\mathbf{X}(\alpha, t), t)}{\boldsymbol{\omega}_0(\alpha)} \right| \mathrm{d}\beta \\
&\geq \int\limits_{\beta_1}^{\beta_2} \frac{e^{-\lambda(L_t)}\Omega_l(t)}{\Omega_l(0)} \mathrm{d}\beta = e^{-\lambda(L_t)} \frac{\Omega_l(t)}{\Omega_l(0)} l(0) .
\end{aligned}
$$

In a slightly weaker form, equation (4.25) was presented in [30] as "lemma 3" as part of a formal proof for a non-blowup criterion. Yet it may be viewed in its own right: The relative increase in length along a time-interval is bounded by
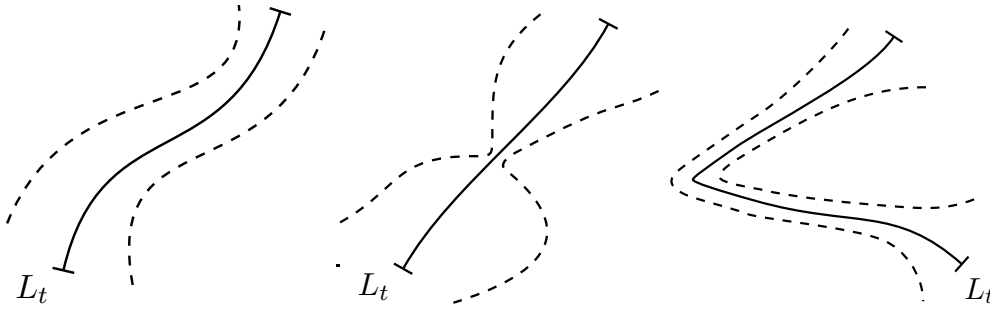
**Figure 4.1.**: Characterizing vortex line geometry in terms of $\lambda(L_t)$. A slightly curved vortex line with approximately parallel neighboring vortex lines (**left**) exhibits small $\lambda(L_t)$. Vortex lines with tightening neighboring vortex lines (**center**) or vortex lines with high curvature, in comparison to their length (**right**) have high $\lambda(L_t)$.

the vorticity increase and a factor $\exp(\pm\lambda(L_t))$. Thus, $\lambda(L_t)$ is a dimensionless number, characterizing the geometric "tameness" of the vortex line filament.

As depicted in figure 4.1, a vortex line segment has a huge $\lambda(L_t)$, if its maximum curvature is large, relative to its length (the segment is "kinked" instead of "curved"), or if the surrounding vortex lines collapse to the considered segment in at least a point (the surrounding is "tightening" instead of "parallel"). A relatively unbent vortex line segment with approximately parallel neighboring vortex lines possesses a low value of $\lambda(L_t)$. This quantifies the constricted notion of "relatively straight" and "smoothly directed" given in [28] in a sharper way.

### 4.2.4. Lagrangian evolution of vortex line segments

Roughly following [30, 31], combining the above results with the Lagrangian vorticity amplification equation (2.39) allows for a connection of the stretching process to the Lagrangian accumulation of vorticity. Since $\partial s/\partial\beta = s_\beta$ differs from $|\boldsymbol{\omega}(\mathbf{X}(\alpha,t),t)|$ just by a constant $|\boldsymbol{\omega}_0(\alpha)|$, accumulation of vorticity behaves exactly as increase in stretching:

$$\frac{D}{Dt}s_\beta = ((\boldsymbol{\xi}\cdot\nabla\mathbf{u})\cdot\boldsymbol{\xi})\,s_\beta\,. \tag{4.26}$$

The *curvature* $\kappa$ of the vortex line $L_t$ fulfills

$$\kappa\mathbf{n} = \frac{\partial\dot{L}_t(s)}{\partial s} = \frac{\partial\boldsymbol{\xi}}{\partial s} = (\boldsymbol{\xi}\cdot\nabla)\boldsymbol{\xi}\,, \tag{4.27}$$

with $\mathbf{n} = \ddot{L}_t/|\ddot{L}_t|$ being the unit normal vector of the vortex line. Then, the Lagrangian evolution of vortex line stretching becomes

$$\frac{D}{Dt}s_\beta = ((\boldsymbol{\xi}\cdot\nabla\mathbf{u})\cdot\boldsymbol{\xi})\,s_\beta$$

$$= \left( (\boldsymbol{\xi} \cdot \nabla)(\mathbf{u} \cdot \boldsymbol{\xi}) - \mathbf{u} \cdot (\boldsymbol{\xi} \cdot \nabla)\boldsymbol{\xi} \right) s_\beta$$
$$= \left( \frac{\partial}{\partial s}(\mathbf{u} \cdot \boldsymbol{\xi}) - \kappa(\mathbf{u} \cdot \mathbf{n}) \right) s_\beta \,,$$

which, using (4.27), leads to

$$\frac{D}{Dt}s_\beta = \frac{\partial}{\partial \beta}(\mathbf{u} \cdot \boldsymbol{\xi}) - \kappa(\mathbf{u} \cdot \mathbf{n})s_\beta \,. \tag{4.28}$$

At this point it becomes obvious how the process of vortex line stretching interacts with the velocity in two distinct ways: The velocity in direction of the vortex line elongates the segment by drawing it out, while a part of the velocity normal to the vortex line increases the segment's length by enlarging its curves.

Integrating (4.28) along the vortex line (from $\beta_1$ to $\beta_2$) yields

$$D_t(s(\beta_2, t) - s(\beta_1, t)) = (\mathbf{u} \cdot \boldsymbol{\xi})(\mathbf{X}(\beta_2, t), t) - (\mathbf{u} \cdot \boldsymbol{\xi})(\mathbf{X}(\beta_1, t), t)$$
$$- \int_{\beta_1}^{\beta_2} \kappa(\mathbf{u} \cdot \mathbf{n})(\mathbf{X}(\eta, t), t)s_\eta \mathrm{d}\eta \,,$$

and integrating over time (from 0 to $t$)

$$l(t) \le l(0) + \int_0^t \left[ (\mathbf{u} \cdot \boldsymbol{\xi})(X(\beta_1, \tau), \tau) - (\mathbf{u} \cdot \boldsymbol{\xi})(X(\beta_2, \tau), \tau) \right] \mathrm{d}\tau$$
$$- \int_0^t \lambda(\tau) \|\mathbf{u} \cdot \mathbf{n}\|_{L^\infty(L_\tau)} \mathrm{d}\tau \,,$$

which results in

$$l(t) \le l(0) + \int_0^t \left[ U_\xi(\tau) + \lambda(\tau) U_n(\tau) \right] \mathrm{d}\tau \,, \tag{4.29}$$

for

$$U_\xi(t) := \max_{\mathbf{x}, \mathbf{y} \in L_t} |(\mathbf{u} \cdot \boldsymbol{\xi})(\mathbf{x}, t) - (\mathbf{u} \cdot \boldsymbol{\xi})(\mathbf{y}, t)|$$
$$U_n(t) := \max_{L_t} |\mathbf{u} \cdot \mathbf{n}|$$

Instead of starting the above reasoning at time $t = 0$, the results are identical for a later time $0 < t_1 < t$. This result may be understood as an upper bound for vortex line stretching in terms of velocity and vortex line geometry.

In conjunction with the connection between length increase and vorticity amplification, given in equation (4.25), we arrive at

$$\Omega_l(t) \leq \Omega_l(0) e^{\lambda(L_t)} \left[ 1 + \frac{1}{l(0)} \int\limits_0^t (U_\xi(\tau) + \lambda(\tau) U_n(\tau)) \mathrm{d}\tau \right] \; .$$

This is an inequality for the control of growth rate of the vorticity by geometric flow properties. From this estimate, by combining it with BKM to distinguish critical from sub-critical vorticity growth, it is a short way to another non-blowup criterion:

**Deng-Hou-Yu theorem 2:** *Assume there is a family of vortex line segments $L_t$ and $T_0 \in [0, T)$, such that $L_{t_2} \subseteq \mathbf{X}(L_{t_1}, t_1, t_2)$ for all $T_0 < t_1 < t_2 < T$. We also assume that $\Omega(t)$ is monotonically increasing and $\|\omega(t)\|_{L^\infty(L_t)} \geq c_0 \Omega(t)$ for some $c_0 > 0$ when $t$ is sufficiently close to $T$. Furthermore, we assume that*

(i) *$U_\xi(t) + U_n(t)\lambda(L_t) \lesssim (T - t)^{-A}$ for some $A \in (0, 1)$*

(ii) *$\lambda(L_t) \leq C_0$,*

(iii) *$l(t) \gtrsim (T - t)^B$ for some $B < 1 - A$.*

*Then there will be no blowup in the 3D incompressible Euler flow up to time T.*

Here, $a(t) \lesssim b(t)$ means there exists a constant $c \in \mathbb{R}$ such that $|a(t)| < c |b(t)|$ (and accordingly for $a(t) \gtrsim b(5)$). The remainder of the proof is given in [30].

It should be noted that theorem 2 again includes assumptions on the dimensionless number $\lambda(L_t)$, which was already encountered when analyzing the process of vortex stretching in section 4.2.3. Especially assumption (ii) poses a uniform bound in time for $\lambda(L_t)$. This translates to words as the process of "zooming in" to the location of maximum vorticity in order to keep the considered vortex line segment relatively straight in comparison to its length. The assumed accompanying collapse in length to keep $\lambda(L_t)$ bounded is then linked in its growth rate to the blowup of the velocity components.

As a side note, the precise way of the coupling between the collapse of the length scale by $(T - t)^B$ and the increase in velocity as $1/(T - t)^A$ can be anticipated by resorting to the scaling arguments brought forward in the context of self-similar solutions. The Euler equations dictate, as derived in section 5.1.2, that a self-similar collapse to a point has to obey

$$\mathbf{u}(\mathbf{x}, t) = \frac{1}{(T - t)^{\frac{h}{h+1}}} \mathbf{U} \left( \frac{\mathbf{x}}{(T - t)^{\frac{1}{h+1}}} \right) \; , \tag{4.30}$$

for some $h \in \mathbb{R}$ and $U : \mathbb{R}^3 \to \mathbb{R}^3$. For $A = h/(h + 1)$ and $B = 1/(h + 1)$ this is exactly the critical scaling behavior of theorem 2.

It is worth mentioning that the above presented criterion, even though it is obviously inspired by the classical geometric criteria introduced in section 4.2.1, still differs in crucial aspects. The posed assumptions are purely local and restricted to the geometry of a single critical vortex line filament. Assumptions on the velocity do not, in contrast to Constantin et al. [28], impose a uniform bound (which is not observed in simulations), but allow for a finite-time blowup of velocity, strictly connected in its growth rate to the geometrical evolution of the filament. The vortex line segment itself is not assumed to be of $O(1)$ length (as in Cordoba and Fefferman [29]) or be contained in an $O(1)$-region (which, again, was not observed in simulations). These aspects in combination render it a promising theorem to be directly tested by numerical simulations. Exactly this will be done in chapter 5.

### 4.2.5. Pressure and symmetries

A rather unusual way of analyzing a finite-time blowup of the Euler equations was derived by Ng and Bhattacharjee [78]. It exclusively concerns the Euler equations for a specific set of symmetries and on a limited subset of the physical domain. Nevertheless it will be presented here since all assumptions, however specific, are actually met for the cases examined in the context of this work.

Suppose a flow with high symmetry, such that

$$v(x, y, z) = \sum_{l,m,n} a_{lmn} \sin(lx) \cos(my) \cos(nz) \tag{4.31}$$

$$\mathbf{u}(x, y, z) = (u_x, u_y, u_z)^T = (v(x, y, z), v(y, z, x), v(z, x, y)) \,. \tag{4.32}$$

This symmetry is called the Kida-Pelz symmetry (Boratav and Pelz [7], Kida [59]) and implies that the normal component of the velocity at the Cartesian planes is anti-symmetric and the tangential components are symmetric. The symmetries are preserved by the Euler equations. Flows with this symmetry will be presented in detail in section 5.2.4.

Now, consider the flow on the line $y = z = 0$. It follows from the constraints of the symmetries at the Cartesian planes that the vorticity $\boldsymbol{\omega}$ completely vanishes and $u_y = u_z = 0$ on this line. The $x$-component of velocity fulfills

$$u_x(x, 0, 0) = v(x, 0, 0) = \sum_{l,m,n} a_{lmn} \sin(lx). \tag{4.33}$$

Due to the symmetry, it is now possible to simplify the evolution in time of the $x$-derivative of $u_x$, $\alpha = \partial_x u_x$, by considering the $x$-derivative of the $x$-component of the Euler equations (2.10):

$$\partial_t \alpha + \sum_i \partial_x (u_i \partial_i u_x) = \partial_{xx} p$$

$$\partial_t \alpha + \sum_i \left(\partial_x u_i\right)\left(\partial_i u_x\right) + \sum_i u_i \partial_i \partial_x u_x = \partial_{xx} p$$

$$D_t \alpha + \alpha^2 = \partial_{xx} p.$$

This partial differential equation for $\alpha$ leads to a finite-time singularity if the sign of $\partial_{xx} p$ is positive. In particular, this leads to the conclusion:

**Ng-Bhattacharjee:** *If for a flow obeying the Kida-Pelz symmetries there exists a Lagrangian fluid element on the Cartesian axis $y = z = 0$, such that*

$$\partial_{xx} p > 0 \tag{4.34}$$

*for all time following this fluid element, then the $x$-derivative of the $x$-component of the velocity, $\partial_x u_x$, will blow up in final time.*

In the original version of [78] this theorem was discarded in favor of a reformulation in terms of the fourth derivative of pressure $\partial_{xxxx} p$ in the origin, as a Lagrangian analysis of the pressure derivative seemed rather complicated. As the numerics presented in this work are capable of tracking Lagrangian quantities, this argument no longer applies and the original version of the theorem as presented above is utilized for numerical simulations in section 5.4.3.

# 5. Simulation of Finite-time Singularities

From the advent of the digital age and with the raise of scientific computing, computational fluid dynamics has been an active topic and has tremendously increased our understanding of the behavior of fluid flow. Since the limited knowledge on nonlinear partial differential equations in many cases does not permit for analytic solutions to be found (with the Navier-Stokes and Euler equations among the most famous examples), it seems very natural to rely on numerical experiments to develop intuition on fluid evolution and vorticity-depletion or -amplification processes. Of course, no purely numerical approach to the problem of existence and uniqueness of solutions to the Euler equations can be found. Nevertheless, experience gained in numerical simulations may be used as a hint for critical quantities or be used to observe promising directions to tackle the problem analytically. Especially the verification of assumptions of analytical blowup criteria can be achieved via numerical means. This will be done in the course of this chapter.

First, referring to the analytical restrictions on possible finite-time Euler singularities given in the previous chapter, typical possible scenarios for a blowup are introduced in section 5.1. This involves the presentation of necessary interactions such as vorticity-strain coupling and the discussion of self-similar flows of various types.

An overview over the attempts to realize these scenarios in practice as initial conditions for Euler flows is given in section 5.2. Here, some notable initial conditions are introduced and discussed, regarding their intent in design and their behavior in numerical simulations. At this point, the choice for the initial conditions of this work will be justified and put in perspective.

Subsequently in section 5.3, the evolution of the flow is presented for the considered initial conditions. This includes an illustration of the formation of typical structures and the analysis of the flow regarding the scenarios for the development of a finite-time singularity that were presented earlier.

Results for the conducted numerical simulations regarding the previously introduced blowup criteria are presented in section 5.4. Here, the focus is on the Lagrangian and geometric criteria. It will be shown by means of the conducted numerical simulations that the assumptions for these geometric non-blowup criteria are met. This poses an evidence against the formation of a finite-time

singularity for the considered initial conditions.

## 5.1. Scenarios for finite-time singularities

It has been established in the previous chapter that a singularity of the Euler equations in finite time necessitates rapid accumulation of vorticity. This section denominates scenarios which facilitate such a critical growth, divided into local and global aspects. Locally, vorticity-strain coupling is identified as the mechanism for nonlinear amplification in finite time. Globally, the notion and possibility of self-similar or locally self-similar collapse to a point is introduced. These aspects will serve as a basis for the construction of initial conditions suitable for the possible formation of a finite-time singularity.

### 5.1.1. Vorticity-strain coupling

Recalling equation (2.37) from section 2.2.4, the Lagrangian evolution of vorticity reads

$$\frac{D\boldsymbol{\omega}}{Dt} = S\boldsymbol{\omega} \; ,$$

where $S$ is the strain, $S = 1/2 \left( \nabla \mathbf{u} + \nabla \mathbf{u}^T \right)$. Due to the incompressibility condition (2.8) the trace of $S$ vanishes and due to the symmetry of $S$ its eigenvalues $\lambda_i$ are real and the corresponding eigenvectors $\mathbf{v}_i$ are orthogonal. Thus $\lambda_1$, the biggest eigenvalue, fulfills $\lambda_1 > 0$ in regions with non-vanishing strain.

If we change into the local coordinate system given by the $\mathbf{v}_i$ (primes denoting variables in the changed coordinates), $S'$ is diagonal and $\omega'_1$ is amplified with $\lambda_1 \omega'_1$. Assuming a strain proportional to the vorticity, $\lambda_1 \sim \omega'_1$, results in

$$\frac{D\omega'_1}{D_t} = {\omega'_1}^2 \; .$$

This leads to a finite-time singularity of the form $\boldsymbol{\omega} \sim (T-t)^{-1}$, conforming with the critical growth rate for the BKM criterion presented in section 4.1.2. This proportionality of the strain to the vorticity is crucial. If the strain rate is constant instead, the growth in vorticity is merely exponential. Several cases have been suggested in which this mechanism may take place.

For an isolated vortex to create a strain of proper coupling to its vorticity, its curvature must approach infinity (see section 5.2.3). The geometric criteria presented in section 4.2 may be interpreted as a sharpening of this statement: For a critical vorticity-strain coupling to be induced by an isolated vortex line, it must either kink or tighten fast enough to be compatible with theorem 2 in section 4.2.4.

Besides "self-stretching"-scenarios, it is possible for neighboring vortices to induce an axial strain sufficient in the above sense. Reflectional symmetries in the flow may provide this behavior [52, 86], as the "mirror images" impose the axial strain on the fundamental vortex tube, even though the above restriction on the curvature still exist. This may be overcome by introducing rotational symmetries, as done by Boratav and Pelz [6] and discussed by Pelz [82]. It can be shown that this class of flows introduces a strain-vorticity coupling that is positive even for vanishing curvature. Scenarios of these classes will be discussed in section 5.2.4.

It should be noted that, contrary to expectations, the vorticity-strain coupling does not readily appear in nature. One would expect a tendency of the vorticity to align itself to the eigenvector of the strain tensor with the largest eigenvalue all by itself, since the parallel component is amplified, while the orthogonal components are damped or stay nearly constant. Nevertheless, for viscid turbulent flows, quite a different behavior is observed both in numerical simulations and experiments: The vorticity is most likely to align to the intermediate eigenvector of the strain tensor (Ashurst et al. [1], Chevillard and Meneveau [16], Meneveau [74]). One can therefore expect that functional vorticity-strain coupling is inherently unstable. The process has to be designed "artificially" by choosing suitable initial conditions.

A more precise notion of the process of vorticity alignment in turbulent flows is given by Hamlington, Schumacher, and Dahm [45]. They distinguish, evaluating equation (2.26) numerically, between strain induced *locally* by the immediate neighborhood and *globally* by long-range interaction. For turbulent flows, they observe a most likely alignment of the vorticity to the most positive eigenvector of the global strain. Taking into account also the local strain restores the alignment of vorticity to the intermediate eigenvector. For the successful emergence of a finite-time singularity of the Euler equations in a point-wise sense, vorticity-strain coupling should be induced by the local strain. In principle, this could be numerically verified by applying the technique from [45] to Euler blowup simulations.

## 5.1.2. Self-similar and locally self-similar blowup

As a global scenario for a finite-time singularity, self-similar solutions are particularly favored by physicists. The question of the existence of self-similar solutions for the Euler equations has its origin in the identical question for the Navier-Stokes equations first posed by Leray [71]. Self-similar solutions are solutions in $\mathbb{R}^3$ of the form

$$\mathbf{u}(\mathbf{x}, t) = \frac{1}{\sqrt{2a(T-t)}} \mathbf{U} \left( \frac{x}{\sqrt{2a(T-t)}} \right) , \qquad (5.1)$$

where $a > 0$ constant, $T \in \mathbb{R}$ and $U : \mathbb{R}^3 \to \mathbb{R}^3$. If a function $\mathbf{U}(\mathbf{x}) \neq 0$ could be found, such that $\mathbf{u}$ of equation (5.1) is a solution to the Navier-Stokes equations, it would lead to a finite-time singularity at time $t = T$. Inserting equation (5.1) back into the Navier-Stokes equation yields

$$a\mathbf{U} + a(\mathbf{y} \cdot \nabla)\mathbf{U} + (\mathbf{U} \cdot \nabla)\mathbf{U} + \nabla P = 0$$
$$\nabla \cdot \mathbf{U} = 0 \, , \tag{5.2}$$

with $\mathbf{y} \in \mathbb{R}^3$. It can easily be seen using standard embedding theorems that by assuming finite kinetic energy and natural energy dissipation we have $\mathbf{U} \in L^3(\mathbb{R}^3)$. In this setup, the question raised by Leray was answered negatively by Nečas et al. [77] and Tsai [92]: If $\mathbf{U} \in L^p(\mathbb{R}^3)$, $p > 3$, fulfills equation (5.2) then $\mathbf{U} = 0$, which rules out a globally self-similar blowup of the Navier-Stokes equations.

## Globally self-similar blowup for the Euler equation

Due to the absence of energy dissipation the situation is slightly more difficult in the Euler case. Here, the constraints posed by scaling are less severe, leading to a larger class of possible self-similar scenarios. In addition, without energy dissipation, the vital argument of the maximum principle [77, 92] is not transferable to the Euler case. The question has to be tackled from a different direction, leading to slightly modified prerequisites for the formal proof.

Consider a rescaling of a solution for the Euler equations,

$$\mathbf{x} = \lambda \, \mathbf{x}' \, , \qquad\qquad \mathbf{u} = \lambda^{-h} \, \mathbf{u}' \, , \tag{5.3}$$

$\lambda > 0$, $h \in \mathbb{R}$. With a simple scaling argument we deduce:

$$t = \lambda^{h+1} t' \, , \qquad\qquad p = \lambda^{-2h} p' \, . \tag{5.4}$$

This means: If $(\mathbf{u}, p)$ is a solution to the Euler equations, then

$$\mathbf{u}'(\mathbf{x}', t') = \lambda^h \, \mathbf{u}(\lambda \mathbf{x}', \lambda^{h+1} t') \, ,$$
$$p'(\mathbf{x}', t') = \lambda^{2h} \, p(\lambda \mathbf{x}', \lambda^{h+1} t') \tag{5.5}$$

is also a solution for arbitrary $\lambda > 0$, $h \in \mathbb{R}$, $h \neq -1$.

For constructing a self-similar solution, the scaling parameter $\lambda$ has to approach zero in finite time in a way that is consistent with a blowup of the Euler equations. Following the requirement of the Beale-Kato-Majda criterion (compare 4.1.2), we therefore want the vorticity, which scales like

$$\boldsymbol{\omega} = \lambda^{h+1} \, \boldsymbol{\omega}' \tag{5.6}$$

to behave in time like

$$\boldsymbol{\omega}(t) \approx \frac{1}{T-t} \boldsymbol{\omega}_0 \tag{5.7}$$

for some $\boldsymbol{\omega}_0$ and the assumed singular time $T \in \mathbb{R}$. This leads to

$$\lambda = (T - t)^{-\frac{1}{h+1}} \ . \tag{5.8}$$

Applying this scaling to construct a self-similar solution to the Euler equations yields

$$\mathbf{u}(\mathbf{x}, t) = \frac{1}{(T - t)^{\frac{h}{h+1}}} \mathbf{U} \left( \frac{\mathbf{x}}{(T - t)^{\frac{1}{h+1}}} \right) \ . \tag{5.9}$$

Note that for $h = 1$ this corresponds to Leray's self-similar solutions (5.1). This class of solutions may be considered as the self-similar solutions to the Euler equations which exhibit a finite-time blowup.

Reinserting equation (5.9) into the Euler equation leads to

$$\frac{h}{h+1} \mathbf{U} + \frac{1}{h+1} (\mathbf{x} \cdot \nabla) \mathbf{U} + (\mathbf{U} \cdot \nabla) \mathbf{U} + \nabla P = 0$$
$$\nabla \cdot \mathbf{U} = 0 \ . \tag{5.10}$$

This is the analogon to equation (5.2) for the Euler equations. Finding a nontrivial solution $\mathbf{U}$ to equation (5.10) is equivalent to finding a finite-time blowup solution to the Euler equation.

This possibility has recently been disproved by Chae [13] and Chae and Shvydkoy [14]. Their reasoning does not make use of energy estimates in combination with scaling properties but directly disproves the existence of a nontrivial vorticity field of the above self-similarity class. If the initial vorticity $\boldsymbol{\omega}_0$ decays sufficiently fast for large $\mathbf{x}$,

$$\exists \, p_1 > 0 \text{ such that } \boldsymbol{\omega}_0 \in L^p(\mathbb{R}^3) \ \forall \, p \in (0, p_1), \tag{5.11}$$

then every vorticity field of the form

$$\boldsymbol{\omega}(\mathbf{x}, t) = a(t) \, \boldsymbol{\omega}_0(b(t) \mathbf{x}) \tag{5.12}$$

that is a solution of the Euler equations up to time $T$, with $a(t)$, $b(t)$ arbitrary real-valued functions must have $b(t) = 1$. Roughly following Chae [13], this can be seen as follows:

The vorticity amplification factor $\alpha(\mathbf{x}, t)$ (see equation 2.40) can be bounded by $\|\nabla \mathbf{u}(\cdot, t)\|_{L^\infty}$ via a simple estimate. Upon integration, the Lagrangian evolution of the absolute value of vorticity, equation (2.39), yields the estimate

$$|\boldsymbol{\omega}_0(\mathbf{X}^{-1}(\mathbf{x}, t))| \exp\left(-\int_0^t \|\nabla\mathbf{u}(\cdot, \tau)\|_{L^\infty} \mathrm{d}\tau\right) \leq a(t)|\boldsymbol{\omega}_0(b(t)\mathbf{x})| \tag{5.13}$$

$$\leq |\boldsymbol{\omega}_0(\mathbf{X}^{-1}(\mathbf{x}, t))| \exp\left(\int_0^t \|\nabla\mathbf{u}(\cdot, \tau)\|_{L^\infty} \mathrm{d}\tau\right),$$

or, computing the $L^p(\mathbb{R}^3)$-Norm for equation (5.13),

$$\|\boldsymbol{\omega}_0\|_{L^p} \exp\left(-\int_0^t \|\nabla\mathbf{u}(\cdot, \tau)\|_{L^\infty} \mathrm{d}\tau\right) \leq a(t)b(t)^{-\frac{1}{p}} \|\boldsymbol{\omega}_0\|_{L^p} \tag{5.14}$$

$$\leq \|\boldsymbol{\omega}_0\|_{L^p} \exp\left(\int_0^t \|\nabla\mathbf{u}(\cdot, \tau)\|_{L^\infty} \mathrm{d}\tau\right).$$

Now $b(t) = 1$, since by assumption $\|\boldsymbol{\omega}_0\|_{L^p}$ remains finite for all $p \in (0, p_1)$ and the flow is smooth for $t \in (0, T)$. This excludes nontrivial globally self-similar blowup solutions for the Euler equations.

As already mentioned in section 4.2.4 for the collapse of vortex line filaments, the scaling restrictions posed by the Euler equations constitute an alternative approach to the interpretation of theorem 2 by Deng et al. [30]: Maintaining a similar geometrical appearance of a critical vortex filament in time, $\lambda(t) = $ const., its length collapses as $(T - t)^B$ and the velocity components $U_\xi$ and $U_n$ blow up as $1/(T - t)^A$, with $A + B = 1$. As soon as $(A + B < 1)$, a finite-time singularity is ruled out.

**Locally self-similar blowup**

It is reasonable to term the previously presented self-similar solutions "global", since the self-similar scaling behavior holds on the entire $\mathbb{R}^3$. This is quite a strict constraint. A weaker form of a self-similarity is to consider scenarios where the self-similar scaling is only valid in a restricted core region, typically shrinking to a point in finite time. Outside this similarity region the solution is assumed to be smooth and need not obey the self-similar scaling of the core. This scenario is especially popular among physicists as a possibility for finite-time blowup for both the Navier-Stokes and the Euler equation, particularly concerning numerical simulations (see e.g. [6, 44, 52, 55, 82]).

Regarding the Navier-Stokes equations, a locally self-similar blowup solution has been excluded under similar conditions as for the global case presented above by Hou and Li [48].

For the Euler equations, analytic results regarding locally self-similar blowup scenarios are scarce. Numerical simulations, especially involving vortex dodecapoles (which will be presented in more detail in section 5.2.4), have repeatedly suggested such behavior (see e.g. [62, 63, 81] for simulations with vortex filaments models, [7] for spectral simulations). Yet, very recently there has been some analytical progress by Chae and Shvydkoy [14] excluding several physically relevant cases.

Section 5.4.4 of this thesis will present numerical evidence against such a scenario for the vortex dodecapole case.

### Cascading self-similar blowup

An even less limiting case of self-similarity is the "cascading self-similarity" (suggested by e.g. [84]). This term is interpreted relatively broad, naming a flow which replicates itself in a periodic or repeating manner.

Consider for example a flow structure of a length scale $\lambda$, which exhibits the formation of an instability of the same form at a fraction of the original length scale, $\frac{1}{n}\lambda$. In such a scenario, a cascading formation of ever smaller (and possibly more violent) structures will evolve, eventually leading to a collapse in finite time. However, such flows are not only difficult to tackle analytically, but also certainly require a complex flow structure to begin with.

A similar case has been proposed [42] for the vortex dodecapole (see section 5.2.4): Vortex tubes with an initially axisymmetric vorticity profile are deformed and flattened severely (termed "pancake"-like) by the strain of their images under rotational symmetry. Yet numerical simulations suggest a roll-up of these vortex sheets at late times, which could possibly result in another vortex dodecapole of a smaller length scale. This scenario is investigated in section 5.3 of this work.

## 5.2. Initial conditions

Along the lines of the above presented scenarios for a finite-time singularity for the Euler equations, a number of numerical simulations have been performed to act as evidence for or against a blowup. Different initial conditions were introduced and subsequently improved or refined to construct flows with prolonged intervals of vorticity-strain coupling. Yet in all cases, the resolution persists as a limiting factor – singular and near-singular behavior remain distinguishable only up to a restricted certainty.

In the following section I will line out the most popular numerical approaches to finite-time self-amplification. I start with a selected overview over the most influential historical attempts up to recently proposed initial conditions. I will

then review the most promising candidates that emerged, notably Kerr's initial conditions and several variants of vortex dodecapoles featuring Pelz's eightfold symmetry.

## 5.2.1. A brief history of initial conditions

The first breakthrough in the numerical simulation of a possible finite-time singularity for the Euler equations was achieved by Morf et al. [76], claiming to have found a finite-time singularity. Their results were obtained by solving the Euler equations as power series using Padé approximants. The Taylor-Green vortex, introduced by Taylor and Green [90] was used as an initial condition. These approximations were later refined by Brachet et al. [8] to a higher order, and shown in comparison to pseudo spectral simulations.

Chorin [19, 20] employed a vortex-segment method to analyze the evolution of a perturbed vortex in a three-dimensional periodic box. Despite limited capability of the method to capture self-induction, the author observes a finite-time blowup of vorticity.

The vortex filament model may be seen as a related numerical method. Introduced by Siggia [89], it allows for variable core sizes but no core deformation and suppresses small-scale instabilities. The author simulates anti-parallel vortex filaments and observes a self-similar collapse in finite time via faster-than-exponential growth of the vortex filament's arc length.

The first notable adaptive mesh simulation of the Euler equations was conducted by Pumir and Siggia [86]. They focused on the evolution of anti-parallel vortex tubes and observed only exponential amplification of vorticity. In more detail, they established that in the critical region the velocity aligns to the eigenvector of the strain matrix corresponding to the intermediate eigenvalue (as discussed in section 5.1.1), which is small in magnitude. However their remeshing and smoothing procedures introduced considerable unphysical energy dissipation.

Bell and Marcus [4] utilized a second-order projection method to simulate the evolution of a perturbed vortex tube up to a resolution of $128^3$. They observe a non-integrable intensification of vorticity and deduce, by fitting the vorticity growth to a BKM-compatible growth, that a blowup is possible with these initial conditions. In late stages, a complex structure ("hairpin-like") develops that does not exhibit vortex flattening but retains its core structure.

The Taylor-Green initial conditions were repeated by Brachet et al. [9] with a pseudo spectral approach that achieved, by using the initial conditions' symmetries, a resolution up to $864^3$ and an amplification of vorticity by a factor of 5. They observe the evolution of "pancake-like" structures that shrink exponentially in time and which fit to a simple self-similar model. They do not exclude a finite-time singularity as an explanation.

Grauer et al. [43] revisited the initial conditions of Bell and Marcus [4] and, using adaptive mesh refinement, achieved an effective resolution of up to $2048^3$ grid points. An amplification of vorticity by a factor of 21 was observed. Again, a "hairpin-like" structure was seen as responsible for the dramatic growth rate. The time evolution of vorticity could be fitted against a finite-time singularity.

Very recently, Bustamante and Brachet [11] redid the calculation for the Taylor-Green initial conditions with a pseudo spectral simulation of $4096^3$ grid points. They analyze the flow by connecting BKM and the analyticity-strip method and observe a change of regime in the flow at the latest stage of the simulation. This disagrees with previous evidence against a finite-time singularity given in [8, 22].

### 5.2.2. Kerr's initial conditions

The above presented list of the last century's numerical hunt for finite-time singularities was, in many cases, inconsistent and the results often were inconclusive or even conflicting. One of the most ambitious and highly contested studies in favor of a finite-time singularity was performed by Kerr [52]. It was widely viewed as the most promising candidate of its time and will therefore be presented briefly in the following paragraphs.
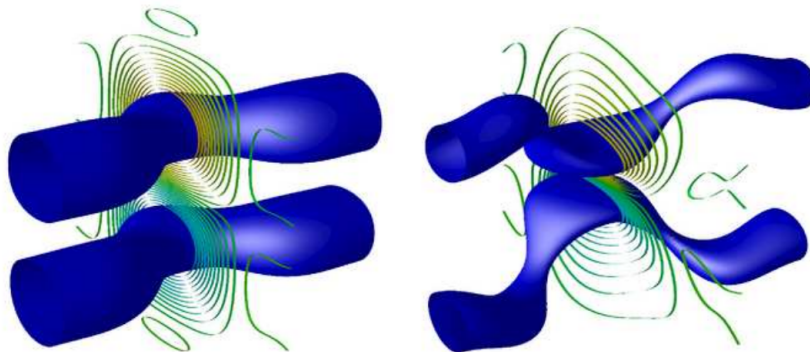


**Figure 5.1.**: Perturbed anti-parallel vortex tubes of Kerr's initial conditions. Depicted is a reconstructed version without the sophisticated spectral filter, **left** at $t = 0$ and **right** at $t = 6$. Source: [47]

Its original form, presented by Melander and Hussain [73] and Kerr and Hussain [58], consists of a compact initial vorticity profile for perturbed antisymmetric vortex tubes (depicted in figure 5.1), smoothed by a high-wave number filter. The improved version [52] features a more complex vorticity profile,

$$\omega(r) = \exp\left(r^2(1 + r^2 + r^4) - \frac{r^2}{1 - r^2}\right) \tag{5.15}$$

with an initial trajectory $(x(s), y, z(s))$ for the perturbed vortex tube of

$$x(s) = x_0 + \delta_x \cos(\pi s/L_x) \tag{5.16}$$

$$z(s) = z_0 + \delta_z \cos(\pi s/L_y) , \tag{5.17}$$

where

$$s(y) = y_2 + L_y \delta_{y1} \sin(\pi y_2/L_y) \tag{5.18}$$

$$y_2 = y + L_y \delta_{y2} \sin(\pi y/L_y) . \tag{5.19}$$

For $\delta_{y1} = \delta_{y2} = 0$, this trajectory is sinusoidal like [58, 73], but with nonzero $\delta_{y1}$ and $\delta_{y2}$ a significantly faster growth of peak vorticity was obtained. These definitions are used to describe the vorticity vector field in the whole domain as

$$\boldsymbol{\omega}_0(\mathbf{x}) = \omega(r)(\omega_x(\mathbf{x}), \omega_y(\mathbf{x}), \omega_z(\mathbf{x})) , \tag{5.20}$$

where $r = |(x, y, z) - (x(s), y, z(s))|/R$ is the rescaled distance to the core trajectory and

$$\omega_x = -\frac{\pi \delta_x}{L_x} \left[ 1 + \pi \delta_{y2} \cos\left(\frac{\pi y}{L_y}\right) \right] \times \left[ 1 + \pi \delta_{y1} \cos\left(\frac{\pi y_2}{L_y}\right) \right] \sin\left(\frac{\pi s(y)}{L_x}\right) , \tag{5.21}$$

$$\omega_y = 1, \tag{5.22}$$

$$\omega_z = -\frac{\pi \delta_z}{L_z} \left[ 1 + \pi \delta_{y2} \cos\left(\frac{\pi y}{L_y}\right) \right] \times \left[ 1 + \pi \delta_{y1} \cos\left(\frac{\pi y_2}{L_y}\right) \right] \sin\left(\frac{\pi s(y)}{L_z}\right) . \tag{5.23}$$

As parameters, $\delta_{y1} = 0.5$, $\delta_{y2} = 0.4$, $\delta_x = -1.6$, $\delta_z = 0$, $z_0 = 1.57$ and $R = 0.75$ where used, and the domain is restricted to $L_x = L_y = 4\pi$, $L_z = 2\pi$ with the "symmetry plane" at $y = 0$ and the "dividing plane" at $z = 0$.

To smooth the rough edges of these initial conditions, a spectral filtering procedure is carried out. This procedure is believed [56, 58] to make the crucial difference between singular and non-singular behavior by inhibiting regions of negative vorticity related to high wave-number fluctuations in the initial spectrum. The filtering was realized in [52] by a rather complex procedure of heavily smoothing with a Fourier code and then remapping to a Chebychew framework. It was claimed [47] that this remapping introduces an asymmetry which renders Kerr's finalized initial conditions hard to reproduce.

In his original simulation, Kerr [52] reached up to $1024 \times 256 \times 128$ degrees of freedom with his Chebychew code. The accumulation of vorticity was reported as being compatible with the Beale-Kato-Majda theorem, with the peak vorticity being located on the symmetry plane. The time dependence of axial strain was also reported to be in agreement with the singular scaling of the peak vorticity. This leads the author to deduce the development of a finite-time

singularity. In addition, backing up these claims, identical rates of collapse in all three directions are observed and indicate a locally self-similar behavior.

In a series of articles [53, 54, 55, 56], various objections, both numerical and analytical in nature, were addressed. Most notably, Hou and Li [47] reconstructed the above initial conditions and redid the simulation using a pseudo spectral code with up to $1536 \times 1024 \times 3072$ grid points. They report, contradicting the above findings, that the maximum vorticity does not grow faster than double exponential in time. They observe a flattening and subsequent roll-up of the vortex tubes.

Very recently [57] a new variation of these initial conditions are in development. They differ in the fact that the perturbation of the vortex tube is locally concentrated to provide more room for surrounding structures to develop.

Even though Kerr's initial conditions are among the most famous candidates for a finite-time blowup and certainly are the most controversial, they will not be examined in this thesis due to the fact that the original initial conditions are unreproducible without details on the smoothing technique applied by Kerr.

It should be noted that there are narrow analytical restrictions on the formation of a finite-time singularity for the scenario of perturbed anti-parallel vortex tubes as considered above. Especially, bounds on the regularity of the direction of vorticity [23, 29] in conjunction with a finite velocity or bounds on the curvature of vortex lines [30, 31] exclude a blowup in finite time. Alternative methods of inducing axial strain without the need of irregular vortex line geometry will be presented in the following section.

### 5.2.3. Reflectional symmetries

It was demonstrated in the previous sections that vorticity-strain coupling (section 5.1.1) is the favored mechanism for a finite-time Euler singularity. Since it is well established that this process is inherently unstable for turbulent flows, it seems natural to search for techniques to artificially keep the coupling existent. One such technique is the introduction of symmetries to the flow. Early examples such as the Taylor-Green vortex or Kerr's initial conditions (section 5.2.2) are already employing such symmetries.

This section is meant to describe the consequences of planes of reflectional symmetry for the process of vorticity-strain coupling. It will also introduce implications of reflectional symmetries on the geometry of vortex lines intersecting the plane of symmetry. This will serve as a motivation for the introduction of high-symmetry initial conditions in section 5.2.4.

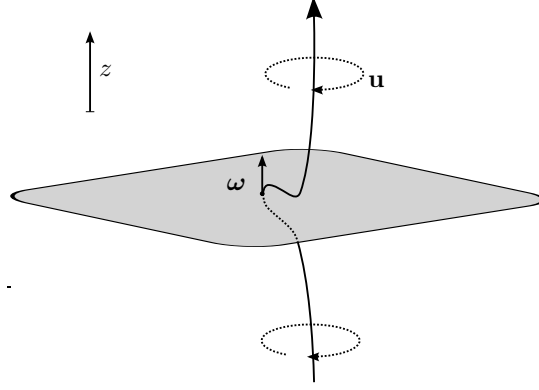Consider the plane $z = 0$ to be a plane of reflectional symmetry, as shown in figure 5.2, defined by

**Figure 5.2.**: Effects of planes of reflectional symmetry on intersecting vortex tubes: In the symmetry plane, the vorticity $\boldsymbol{\omega}$ is normal and the strain tensor possesses a parallel eigenvector with corresponding eigenvalue $S_{zz}$. The curvature $\kappa$ in the symmetry plane has to increase in order to support critical vorticity-strain coupling.

$$
\begin{aligned}
u_x(x, y, z) &= u_x(x, y, -z) \\
u_y(x, y, z) &= u_y(x, y, -z) \\
u_z(x, y, z) &= -u_z(x, y, -z)
\end{aligned}
$$

for the velocity vector field, which leads to $u_z = 0$ in the plane of symmetry. Accordingly, the vorticity obeys

$$
\begin{aligned}
\omega_x(x, y, z) &= -\omega_x(x, y, -z) \\
\omega_y(x, y, z) &= -\omega_y(x, y, -z) \\
\omega_z(x, y, z) &= \omega_z(x, y, -z)
\end{aligned}
$$

and in particular $\omega_x = \omega_y = 0$ or $\boldsymbol{\omega} = \omega_z \hat{e}_z$ in the plane of symmetry. Due to these properties, the strain tensor has $S_{xz} = S_{yz} = S_{zx} = S_{zy} = 0$, or

$$
S = \begin{pmatrix} S_{xx} & S_{xy} & 0 \\ S_{xy} & S_{yy} & 0 \\ 0 & 0 & S_{zz} \end{pmatrix} . \tag{5.24}
$$

It immediately follows that the eigenvector corresponding to the eigenvalue $S_{zz}$ is directed normally to the symmetry plane, and the vorticity vector is aligned to it. Note that this is the sole consequence of the reflectional symmetry and is in no way influenced by the flow. A vortex tube normal to the symmetry plane therefore seems like a natural candidate for critical accumulation of vorticity by means of vorticity-strain coupling: All that is needed is a sufficiently long period of time in which $S_{zz} \sim \omega_z$ at one point of the symmetry plane.

This possibility has been analyzed by Pelz [82] and will be summed up here. As presented in section 2.2.1, the strain can be expressed in terms of the vorticity via the Biot-Savart law (2.26). Taking into account only the $zz$-component, the strain tensor in the plane of symmetry is given by

$$S_{zz} = \frac{3}{4\pi} \int \left( (x - x')\omega_y(\mathbf{x}') - (y - y')\omega_x(\mathbf{x}') \right) \frac{(z - z')}{|\mathbf{x} - \mathbf{x}'|^5} \mathrm{d}\mathbf{x}' \ . \tag{5.25}$$

Equation (5.25) shows that $S_{zz}$ in the plane of symmetry does not scale with $\omega_z$, but does instead depend on $\omega_x$ and $\omega_y$, which are both equal to zero in the $z = 0$ plane. Yet, in close proximity to the plane, $\omega_x$ and $\omega_y$ may grow, depending on the curvature of the vortex line intersecting the symmetry plane.

This may be formalized as follows: As known from section 4.2.4, the curvature of a vortex line fulfills

$$\kappa \mathbf{n} = \boldsymbol{\xi} \cdot \nabla \boldsymbol{\xi} \ . \tag{5.26}$$

Since in the plane of symmetry, it holds $\boldsymbol{\xi} = \hat{e}_z$, we have for each component of the curvature:

$$\begin{aligned}
\kappa \mathbf{n}_i &= (\boldsymbol{\xi} \cdot \nabla \boldsymbol{\xi})_i \\
&= \frac{\partial}{\partial z} \xi_i \\
&= \frac{\partial}{\partial z} \left( \frac{\omega_i}{|\boldsymbol{\omega}|} \right) \\
&= \frac{1}{|\boldsymbol{\omega}|} \frac{\partial}{\partial z} \omega_i - \frac{1}{|\boldsymbol{\omega}|^2} \omega_i \frac{\partial}{\partial z} |\boldsymbol{\omega}| \\
&= \frac{\partial_z \omega_i}{\omega_z} \ ,
\end{aligned}$$

since $\partial_z |\boldsymbol{\omega}| = 0$ in the symmetry plane. With defining $\kappa_i = \kappa \mathbf{n}_i$ we arrive at

$$\kappa_x = \frac{\partial_z \omega_x}{\omega_z} \tag{5.27}$$

$$\kappa_y = \frac{\partial_z \omega_y}{\omega_z} \tag{5.28}$$

$$\kappa_z = 0 \ . \tag{5.29}$$

With this in mind, consider a Taylor-expansion of $\omega_i$, $i \in \{x, y\}$ around $z = 0$ in $z$-direction. Since $\omega_i(z = 0) = 0$,

$$\omega_i = h \left. \frac{\partial \omega_i}{\partial z} \right|_{z=0} \tag{5.30}$$

$$= h \kappa_i \omega_z(z = 0) \tag{5.31}$$

for small $h$ up to first order. Therefore, if the curvature is huge close to the plane of symmetry, $\omega_i$ with $i \in \{x, y\}$ approximately scales like $\omega_z$ and thus $S_{zz}$ may scale with $\omega_z$ too. However, for this to happen, we need $\kappa \approx 1/h$. As a matter of fact, the dimensionless number $\kappa_i h$ plays a similar role as the characteristic geometric number $\lambda(t)$ introduced in section 4.2.3. For $S_{zz}$ to blow up like $\omega_z$, the curvature has to increase in a way to counter the shrinking of the length scale $h$.

On the other hand, the axial strain $S_{zz}$ stretches the vortex tube in $z$-direction. This counteracts any increase in curvature to a certain degree. More precisely, the Lagrangian evolution of the curvature components $\kappa_x$ and $\kappa_y$ can easily be calculated:

$$
\begin{aligned}
\frac{D}{Dt}\kappa_x &= \frac{D}{Dt}\left(\frac{\partial_z \omega_x}{\omega_z}\right) \\
&= \frac{\partial_z D_t \omega_x}{\omega_z} - (\partial_z u_z)\frac{\partial_z \omega_x}{\omega_z} - \frac{\partial_z \omega_x}{\omega_z^2} D_t \omega_z \\
&= \frac{1}{\omega_z}\frac{\partial}{\partial z}\left(\sum_i S_{xi}\omega_i\right) - 2\kappa_x S_{zz} \\
&= \kappa_x S_{xx} + \kappa_y S_{yy} + \partial_z S_{yz} - 2\kappa_x S_{zz} \\
&= (S_{xx} - 2S_{zz})\kappa_x + S_{yy}\kappa_y + \partial_z S_{yz}
\end{aligned}
$$

and similarly

$$
\frac{D}{Dt}\kappa_y = S_{xx}\kappa_x + (S_{yy} - 2S_{zz})\kappa_y + \partial_z S_{xz} \ .
$$

This quantifies the effect of axial stretching on the normal curvatures: The axial strain $S_{zz}$ diminishes the both $\kappa_x$ and $\kappa_y$.

These counteracting processes of vortex line geometry are by no means analytically exact, since all long-range interactions have been ignored. Nevertheless, they constitute an intrinsic resistance of a single vortex line to "self-stretch" in a critical way. The argument may be readily translated to the case of (perturbed) anti-parallel vortex tubes: Since no other components of vorticity are introduced, $S_{zz}$ still only depends on $\omega_x$ and $\omega_y$ which in turn rely on high curvature to scale like $\omega_z$ close to the plane of symmetry.

One way to counter this is to induce the axial strain by neighboring tubes instead of relying on a sufficiently large kink. This will be presented in the following section by introducing additional rotational symmetry.

## 5.2.4. High symmetry initial conditions

In this section, an important class of initial conditions is introduced: The high symmetry initial conditions. As a common property, scenarios of this type tend to maximize the number of symmetries for various reasons:

**Flow Properties:** The initial symmetries are preserved by the flow. It is thus possible to study specific properties that are facilitated by the chosen symmetries. Although flows of this kind often are artificial (i.e. may never occur in reality), they are chosen because the interactions provided by the symmetries are believed to encourage singular behavior.

**Memory consumption:** Both reflectional and rotational symmetries reduce the number of degrees of freedom. This can be used in numerical simulations to reduce the amount of memory needed to store the flow or enables to increase the resolution significantly without exceeding the memory limitations.

**Instructions:** The lower number of degrees of freedom results in less interactions and ultimately leads to a lower number of instructions needed to perform numerical simulations. Typically this effect is even larger than the aforementioned memory savings. Using high symmetry initial conditions enables to perform numerical simulations in a fraction of the original time.

The already mentioned Taylor-Green vortex [90] may be seen as the predecessor of this class of initial conditions, as it already features reflectional symmetries. Kerr's initial conditions go one step further by introducing two planes of reflectional symmetry. In the following section I will present the most successful candidates of the class of initial conditions with even more symmetries implemented.

**Kida-Pelz symmetries**

One notable high-symmetry flow was introduced by Kida [59] and has subsequently been used extensively to probe a possible Euler blowup numerically (Boratav and Pelz [7], Cichowlas and Brachet [22], Pelz [83]) or analytically (e.g. Ng and Bhattacharjee [78]) as well as study the onset of turbulence (e.g. Boratav and Pelz [6]). The Kida-Pelz flow has a three-fold rotational symmetry about the diagonal and a reflectional symmetry about all three Cartesian planes. Flows with these two properties are termed as invariant under the full octahedral group [82]. The Euler (and Navier-Stokes) equations preserve the Kida-Pelz symmetries. In general one can write these initial conditions as

$$v(x,y,z) = \sum_{l,m,n} a_{lmn} \sin(lx) \cos(my) \cos(nz) \qquad (5.32)$$

$$\mathbf{u} = (u_x, u_y, u_z)^T = (v(x,y,z), v(y,z,x), v(z,x,y)) . \qquad (5.33)$$

This means, for a computational domain spanning the interval $[0, \pi]$ in all three dimensions, that the normal component of the velocity field is anti-symmetric

under reflection at the Cartesian planes while the tangential components are symmetric. Combining this with the three-fold rotational symmetry adds up to a total memory saving factor of 1/24.
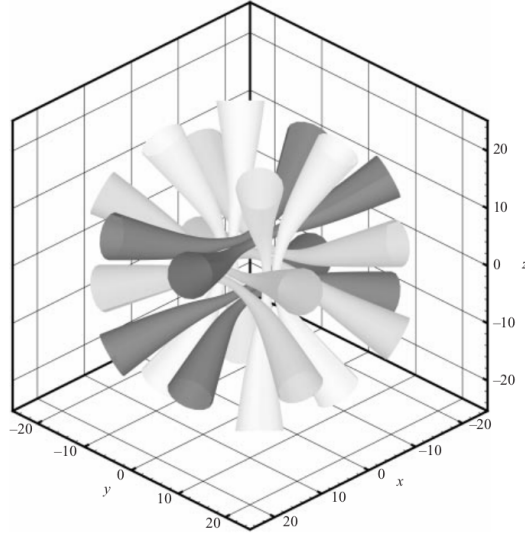


**Figure 5.3.**: A flow that exhibits the Kida-Pelz symmetry: a three-fold rotational symmetry about the domain diagonal as well as a reflectional symmetry about the three Cartesian planes. Source: [82]

On the same time there is reason to hope that these rather artificial symmetries encourage singular behavior if the initial conditions are constructed accordingly. When assuming a localized vortex tube intersecting the symmetry plane normally, as depicted in figure 5.3, its mirror images result in a total of six pairs of anti-parallel vortex tubes. It has been proposed by Pelz [82] that the strain induced by the rotational images of each tube, assuming a velocity field supporting a collapse to the origin, may lead to the desired vorticity-strain coupling described in section 5.1.1 without being subject to the counteraction of strain and curvature in the planes of symmetry. Provided that the vortex dodecapole retains its shape during collapse, this scenario of local self-similarity is exactly the one that was addressed in 5.1.2.

**Original Kida-Pelz initial conditions**

In its original form, the Kida-Pelz initial conditions were proposed by Kida [59], Kida and Murakami [60, 61] and simulated by e.g. Boratav and Pelz [6]. They read

$$u(x, y, z) = \sin(x)\Big(\cos(3y)\cos(z) - \cos(y)\cos(3z)\Big)$$
$$v(x, y, z) = \sin(y)\Big(\cos(3z)\cos(x) - \cos(z)\cos(3x)\Big) \qquad (5.34)$$
$$w(x, y, z) = \sin(z)\Big(\cos(3x)\cos(y) - \cos(x)\cos(3y)\Big)$$

and are clearly of the form of equation (5.32). These initial conditions evolve into a dodecapole (6 vortex dipoles) in short time. Its vortices approach the symmetry planes while simultaneously flattening. A detailed description of the evolution of the original Kida-Pelz initial conditions is given by Boratav and Pelz [7].
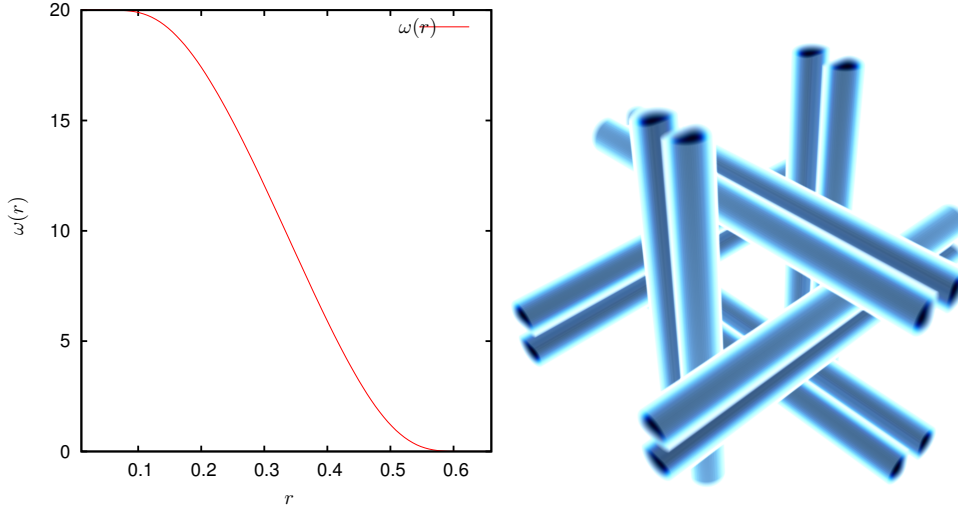
**Grauer initial conditions**



**Figure 5.4.: Left:** Vorticity profile of one tube of the Grauer 12-tube initial condition (with $A = 20$). **Right:** Volume plot of the vorticity for the whole domain.

A refined version of these initial conditions is based on the idea to already start with a dodecapole consisting of vortices of a designated vorticity profile. An example is the Grauer initial condition [41] with a vorticity profile given by

$$\omega(r) = \begin{cases} -A\left[1 - \exp\left(-e^2\log(2)\frac{1}{3r}\exp\left(\frac{1}{\frac{3r}{2} - 1}\right)\right)\right] & \text{for } r < \frac{2}{3} \\ 0 & \text{for } r \geq \frac{2}{3} \end{cases} \qquad (5.35)$$

where $r$ denotes the distance to the tube's center line. The vorticity decreases with increasing distance to the center line and is strictly zero for $r > 2/3$.

Thus, the vortex has compact support in the $r$-$\varphi$-plane while still being smooth. Figure 5.4 (left) displays the vorticity profile given above, figure 5.4 (right) shows the whole dodecapole. Only one octant, i.e. three vortices, are simulated due to symmetry. For the reasons lined out in the previous sections, this kind of dodecapole appears to very promising in terms of developing a finite-time singularity in the origin because of reciprocal strain of the mirror tubes. It is furthermore susceptible to the analysis by the presented geometric blowup criteria. Most of the diagnostics in this thesis are therefore performed on flows which are based on initial conditions of this type.
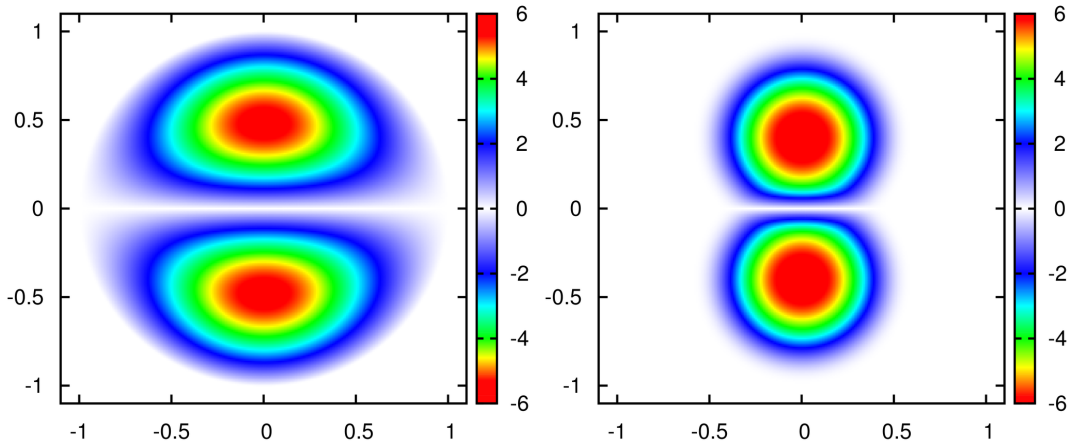
**Lamb-dodecapole**



**Figure 5.5.**: **Left:** Lamb dipole used in the Lamb-dodecapole initial conditions. **Right:** Dipole used in Grauer's initial conditions. Both are scaled to fit in amplitude and size.

For the Euler equations, a single stretch-free axisymmetric vortex may have *arbitrary* radial dependence for the vorticity to remain stationary in time. The same is not true for vortex dipoles: An isolated vortex dipole propagating through the domain does not preserve its shape. This so-called *vortex shedding* is believed [80] to influence and possibly suppress a self-amplifying behavior.

There are exact form-preserving dipole solutions of the 2-dimensional Euler equations which may be used to construct initial conditions that do not exhibit vortex shedding. The most famous is the Lamb-dipole introduced by Lamb [70]. Following Wu et al. [93] it is defined by

$$\omega(r) = \begin{cases} 2Uk\dfrac{J_1(kr)}{J_0(ka)}\sin(\theta) & \text{for } r < a \\ 0 & \text{for } r \geq 0 \end{cases} \tag{5.36}$$

where $k$ is chosen such that $ka$ is the first zero of $J_1$, i.e. $ka \approx 3.8317$. In Figure 5.5 this vorticity distribution is compared to the vorticity profile given in equation (5.35). Note that even though the distribution of vorticity for the Lamb dipole is less sharp than for the Grauer conditions, it is not differentiable at $r = a$, as can be seen in equation (5.36). Because of this, strictly speaking, the Lamb dipole is an improper candidate for the search for finite-time singularities. This issue is usually overcome by smoothing high frequency components in order to smear out the discontinuity in the gradient of the vorticity.

Orlandi and Carnevale [80] where the first to use Lamb dipoles to construct a colliding pair of dipoles, observing a rapid amplification of vorticity for a period of time, with a slowing growth at later times due to either depletion of nonlinearity [37] or lack of resolution.

The Lamb dipole is used in a similar manner in the context of this thesis to form a Lamb dodecapole analogous to Grauer's initial conditions presented above.

## 5.3. Evolution of the flow

In the previous section the vortex dodecapole initial conditions were introduced as a promising candidate for the formation of a finite-time singularity in the Euler equations. A detailed motivation was given to distinguish the vorticity-strain coupling mechanisms in high-symmetry dodecapole flows from similar processes in perturbed vortex tubes or anti-parallel vortex tubes.

This section is devoted to the visible results of the actual simulation of such configurations. For this purpose, the CWENO vector potential formulation presented in section 3.2 is used in conjunction with adaptively refined meshes for simulations with a resolutions of up to $8192^3$ effective grid points, taking into account the increase in resolution due to the high symmetry of the initial conditions. Both the Lamb dodecapole and the Grauer dodecapole introduced in section 5.2 are used as initial conditions. A compilation of the conducted numerical simulations, concerning their resolution and refinement strategy, is given in table 5.1. It should be noted that the highest achieved resolution with $8192^3$ grid points was merely conducted as a proof of concept, due to limited available computing time.

In the following sections, an overview of the basic structure of vortex dodecapole flows is given. This includes the presentation of vortex isosurface plots of the flow evolution, with a focus on the latest stage, where the previously bad resolved roll-up of pancake-like vortex sheets can be observed in full detail. Conclusions are drawn from the visual appearance of the flow, concerning the existence of locally self-similar or cascading self-similar point-wise singular behavior.

|         | initial condition  | effective Resolution | refinement criterion     |
|---------|--------------------|----------------------|--------------------------|
| `lamb`    | Lamb dodecapole    | $1024^3$             | no refinement            |
| `static1` | Grauer dodecapole  | $1024^3$             | no refinement            |
| `static2` | Grauer dodecapole  | $2048^3$             | no refinement            |
| `amr1`    | Grauer dodecapole  | $4096^3$             | AMR, $|\nabla\mathbf{u}|$ |
| `amr2`    | Grauer dodecapole  | $4096^3$             | static refinement        |
| `amr3`    | Grauer dodecapole  | $8192^3$             | static refinement        |

**Table 5.1.**: Overview over properties of all production runs considered in this thesis. Stated are the type of initial condition, the effective resolution at the final time of the simulation (considering symmetries and refined grids) and the refinement criterion.

As will be presented in the following paragraphs, the two considered variants of vortex dodecapoles do not differ significantly in their structure at late times of the simulation. Due to slightly preferable behavior of the Grauer dodecapole, concerning its smoothness in the transition region to the surrounding flow, this initial condition is the favored one in the context of this thesis. All high-resolution production runs are performed using the Grauer dodecapole as well as most of the blowup criteria and diagnostics. Most notably, all geometric results of this thesis refer to that case. Because of the overall similarity of both initial conditions, the obtained results may nevertheless be interpreted as valid for the whole class of vortex dodecapole flows.

### 5.3.1. Grauer dodecapole

The Grauer dodecapole presented in section 5.2.4 was chosen as a prototype for the class of vortex dodecapole initial conditions. Its main features are a smooth vorticity profile with compact support and straight, unperturbed initial vortex tubes.

Pictured in figure 5.6 is the evolution in time for the Grauer dodecapole. Shown are isosurfaces of the absolute vorticity $|\boldsymbol{\omega}(\mathbf{x}, t)|$ at 75% of the peak vorticity for different times. Due to the high symmetry, only one octant of the computational domain is simulated. The figures therefore depict only one half of a vortex tube, with twelve similar tubes in the total domain. The initial phase of the development is depicted in the first two sub-figures: The initially straight tube gets slightly stretched due to interaction with the neighboring tubes. In the third frame, the well-known flattening is in progress. The last three pictures present the final stage of the flow, where the tip of the sheet rolls up and forms a secondary vortex sheet. In the final figure, the secondary sheet exceeds the original sheet in length. Its tip gets drawn out of the collapsing region.
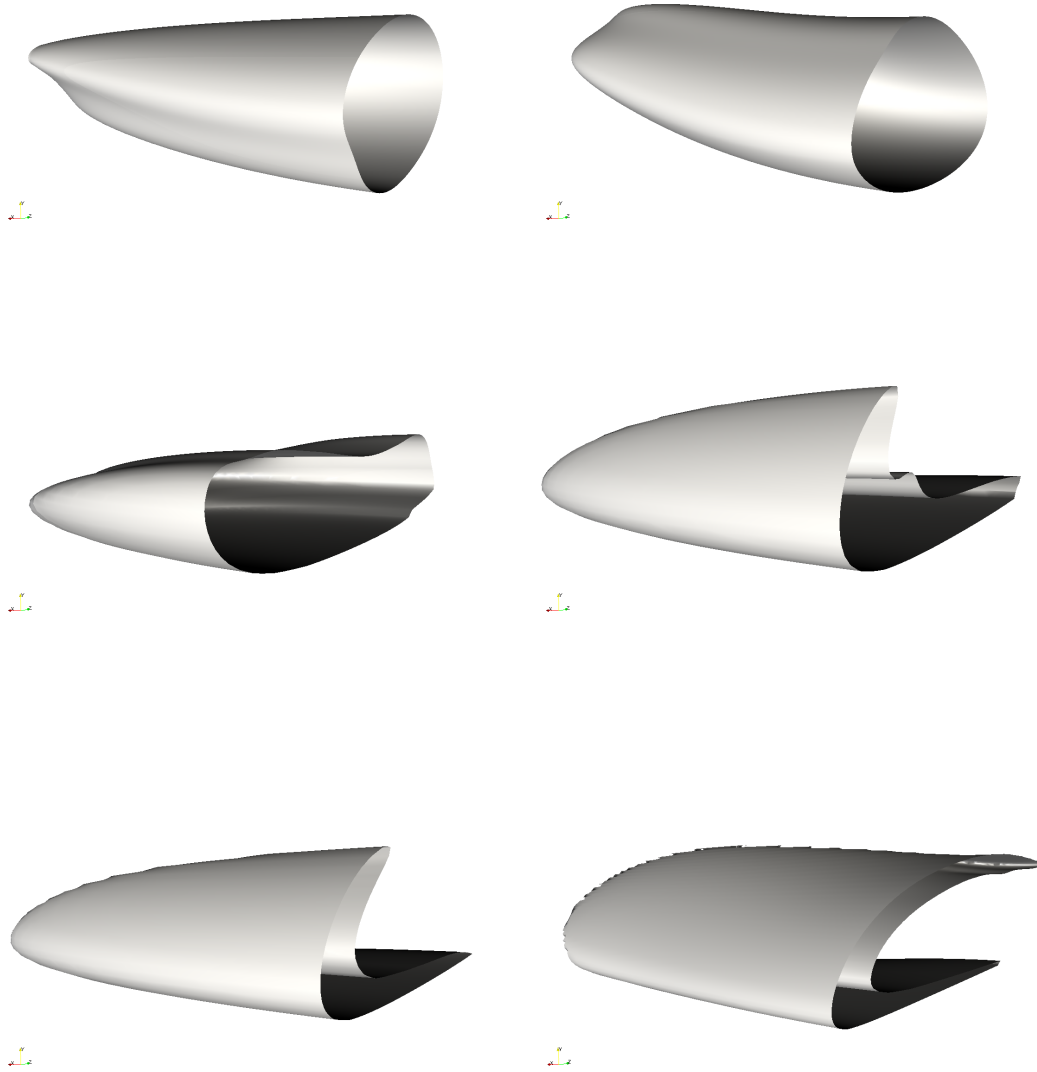
**Figure 5.6.**: Evolution of the Grauer dodecapole. Pictured are isosurfaces of the absolute vorticity, $|\boldsymbol{\omega}(x,t)|$ at 75% of the peak vorticity. Only one of twelve tubes is shown. The flattening of the vortex tube is followed by a roll-up. The developing secondary sheet finally exceeds the original sheet in size. All pictures are from run `amr1`.

The appearance of the roll-up and the secondary vortex sheet are a first evidence against the formation of a point-wise singularity. Especially, the proposed scenario of a locally self-similar amplification and collapse (see section 5.1.2) seems unlikely: The initially round vortex tubes are severely deformed and do not resemble their initial configuration in shape. Additionally, no "cascading" type of self-similarity is observed, at least not on time scales reached by the simulation. The speculation that the formation of a roll-up may lead to the emergence of a tube-like structure which again form a dodecapole arrangement is clearly conflicting the numerical evidence.

Nevertheless, a rapid accumulation of vorticity at the tip of the sheet is observed. This behavior will be analyzed in detail with help of the presented criteria in section 5.4.

### 5.3.2. Lamb dodecapole

The Lamb dodecapole initial conditions, as introduced in section 5.2, are motivated by the fact that each Lamb dipole in itself is an exact and invariant solution to the Euler equations. It was therefore anticipated by Orlandi and Carnevale [80] that a more complex setup consisting of Lamb dipoles will exhibit considerably less core deformation for the vortex tubes. If this assumption would be met, the dodecapole arrangement could lead to the formation of a locally self-similar blowup scenario: The Lamb-dipoles would approach and amplify each other, but, without core deformation, stay in their relative alignment and shape. The ever-decreasing length-scale would result in a point-wise collapse to the origin.

As shown in figure 5.7, this scenario is not observed in the numerical simulation. The initial tubes are deformed severely in the course of the simulation. Vortex core deformation is not prevented. This is hardly surprising, since the vortex dodecapole relies on strain imposed by the rotational images of the tube *by design*, while the Lamb dipole configuration only prevents deformation by the reflectional image. Due to the initially close proximity of all twelve vortex tubes and the short timescale of the evolution, deformation induced by the reflectional partner seems to be negligible, regardless of the actual vorticity profile of the tubes.

Altogether, the evolution of the vortex tubes for the Lamb case resembles the above presented Grauer dodecapole flow: An initial flattening of the tubes is followed by a roll-up. The emerging secondary vortex sheet gets drawn out and finally exceeds the original sheet in length. Due to the overall similarity of both flows it seems safe to deduce that the topological flow evolution only weakly depends on the precise vorticity profile. This may be seen as motivation to transfer the results for just one particular initial condition to the whole class of vortex dodecapole flows.
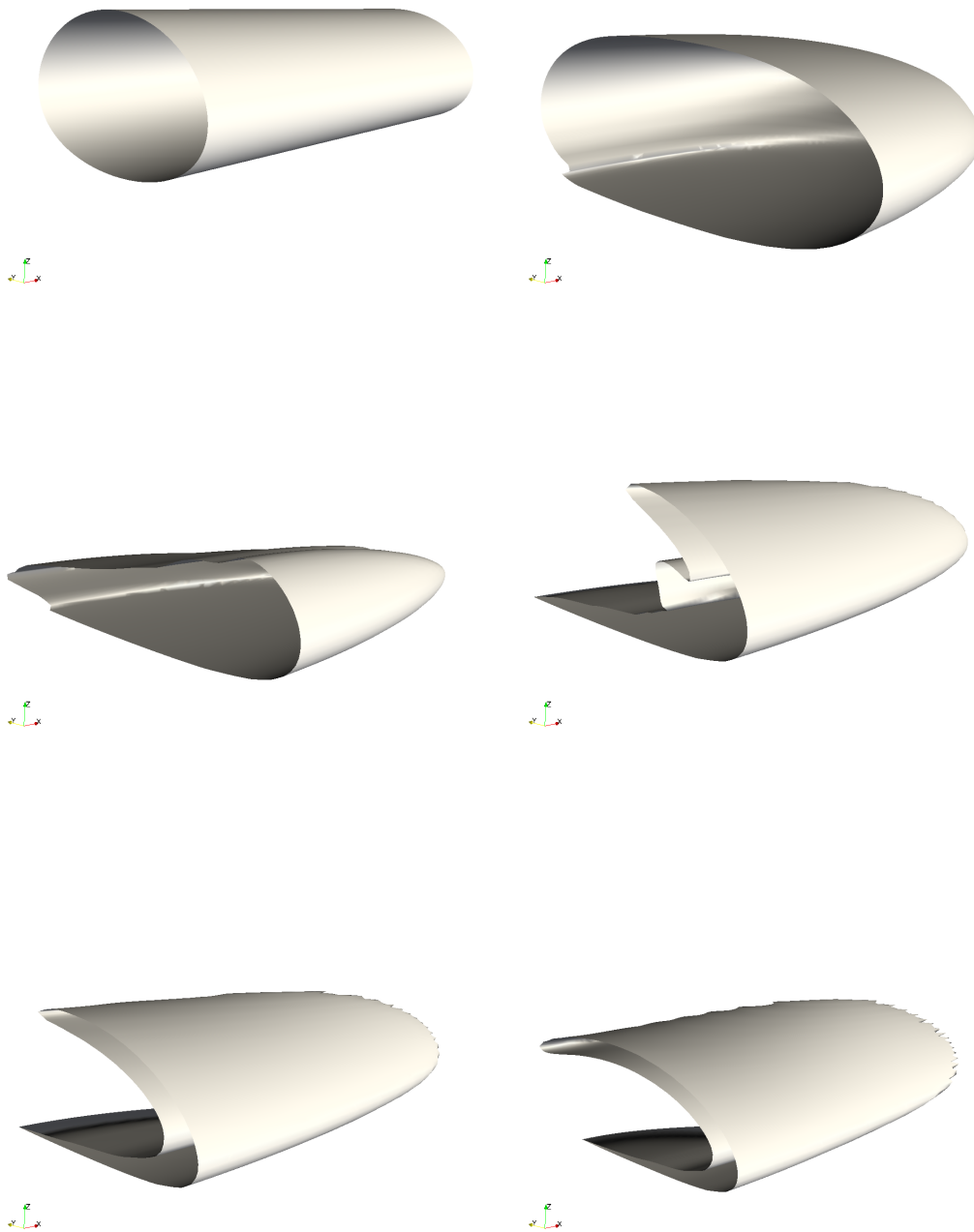
**Figure 5.7.:** Evolution of the Lamb dodecapole. Pictured are isosurfaces of the absolute vorticity, $|\boldsymbol{\omega}(x,t)|$ at 75% of the peak vorticity. Again, only one of twelve tubes is shown. As before, the vortex tube is flattens, followed by a roll-up. A secondary vortex sheet develops and gets drawn out of the center region. All pictures are from run `lamb`.

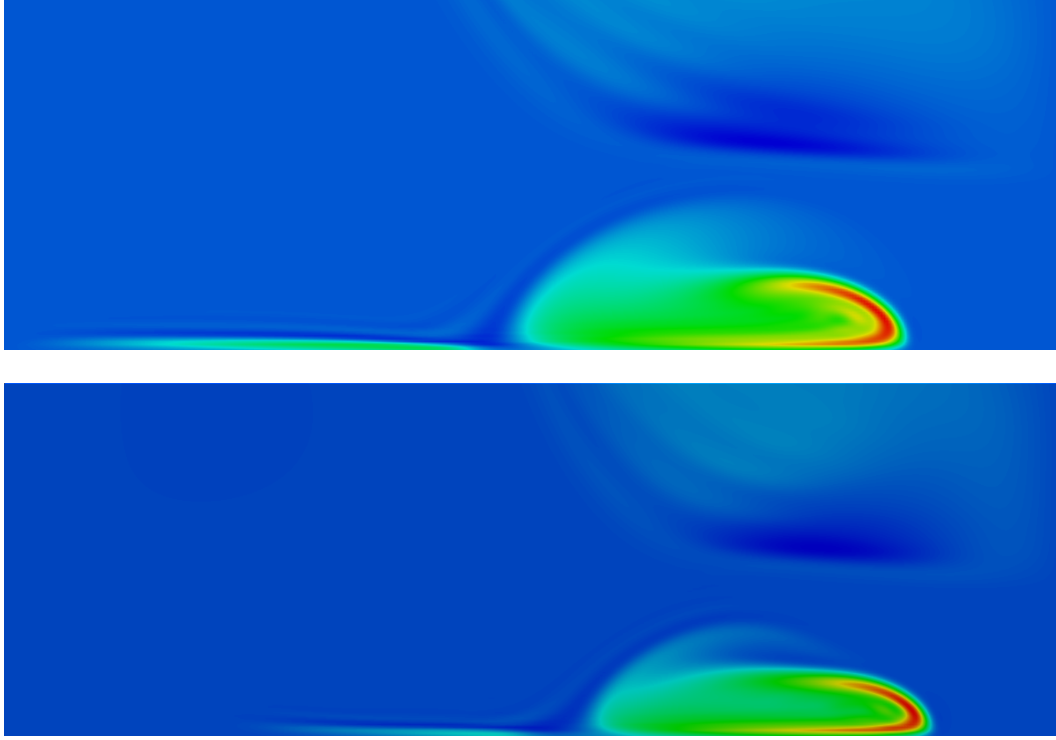### 5.3.3. Comparison and conclusion



**Figure 5.8.**: Direct comparison between the Lamb and the Grauer vorticity profile at late time. The vorticity in a slice near the plane of symmetry, $z = 0.1$, is pictured. The Lamb dodecapole (**top**) exhibits a more pronounced trailing vortex sheet near the symmetry plane. This effect is considerably smaller for the Grauer vorticity profile (**bottom**).

The results of the previous two sections lead to the conclusion that no remarkable differences exist in the overall properties of the flow. In figure 5.8, a direct comparison between low resolution runs ($1024^3$) for the Grauer and the Lamb vorticity profile are shown for a late time to reveal the details of the differences. Most of the large-scale structures are identical for both flows. The initial shape of the Lamb profile is responsible for the formation of a less sharp roll-up of the vortex sheet and the accumulation of secondary vorticity inside the kink. Furthermore, the trailing vortex sheet, which is an artifact of the collapse of the vortex dipoles to the center, is considerably stronger for the Lamb dipoles.

Since, additionally, the core deformation is not effectively prevented in the Lamb case, these arguments were the reason that all high resolution runs and all geometric diagnostics were performed for the Grauer dodecapole initial conditions.

# 5.4. Blow-up Criteria

In chapter 4, criteria have been introduced for the analysis of possible finite-time Euler singularities. The most famous of them, the criterion of Beale et al. [3], has been used to evaluate the accumulation of vorticity in nearly every attempt to numerically probe Euler singularities. As for the Lagrangian and geometric approach to Euler singularities, numerical results are relatively scarce.

In the following sections I will present the numerical measurements for the considered criteria. All obtained data stems from high resolution refined simulations of the Grauer dodecapole. The simulation data will be used to serve as numerical evidence against the formation of a finite-time singularity for the class of vortex dodecapole flows. First, in section 5.4.1, the accumulation of vorticity is quantitatively shown and the classical BKM approach will subsequently be taken in section 5.4.2 to underline the misleading nature of monitoring $\Omega(t)$ alone. In what follows, evidence against a point-wise collapse is presented in section 5.4.4 with the help of geometric properties of the critical vortex line. Finally, uncritical scaling of velocity components is used in section 5.4.5 to serve as numerical evidence against a blowup of vorticity by means of theorem 2 presented in section 4.2.4.

## 5.4.1. Accumulation of vorticity and strain

The vortex dodecapole is designed to be a violent initial condition with rapid accumulation of vorticity. Unlike e.g. the Taylor-Green vortex or Kerr's initial conditions, no sustained phase of flow evolution has to be awaited for the critical structures to form. Thus, vorticity accumulation sets in immediately.

Figure 5.9 shows the evolution of the maximum of vorticity $\Omega(t)$ in time for different resolutions. A higher effective resolution increases the amount of vorticity accumulation until the simulation begins being under-resolved. For all cases, the value of $\Omega(t)$ increases rapidly without showing any sign of deceleration or saturation. The overall vorticity amplification from initially $\Omega(0) = 20$ exceeds a factor of 100 for all resolutions larger than $1024^3$. In all cases, the location of the maximum vorticity follows the *tip* of the vortex sheet presented in section 5.3.1, and is located at the intersection of the vortex sheets when the roll-up begins to form.

The growth of the maximum of the norm of the strain, $\|S(\cdot, t)\|_{L^\infty}$ behaves in a similar manner as the peak vorticity. Figure 5.10 shows the increase in maximum strain, which is about $\|S(\cdot, 0)\|_{L^\infty} \approx 12.4$ initially and grows by two orders of magnitude in the course of the simulation. Position of maximum strain and maximum vorticity are fairly far apart at the beginning of the simulation, but collapse to a point at late stages, with the phase of collapse beginning at about $t = 0.5$. This convergence in the positions of strain and vorticity to
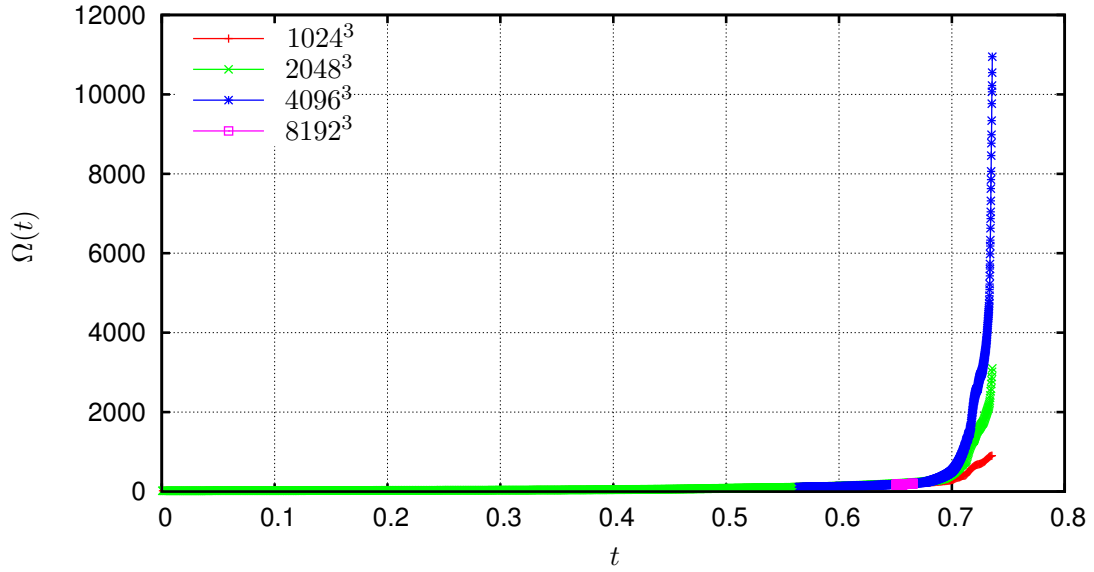
**Figure 5.9.**: Evolution of the maximum vorticity $\Omega(t)$ in time. The initial peak vorticity $\Omega(0) = 20$ is amplified by at least two orders of magnitude, with larger results for higher resolution.
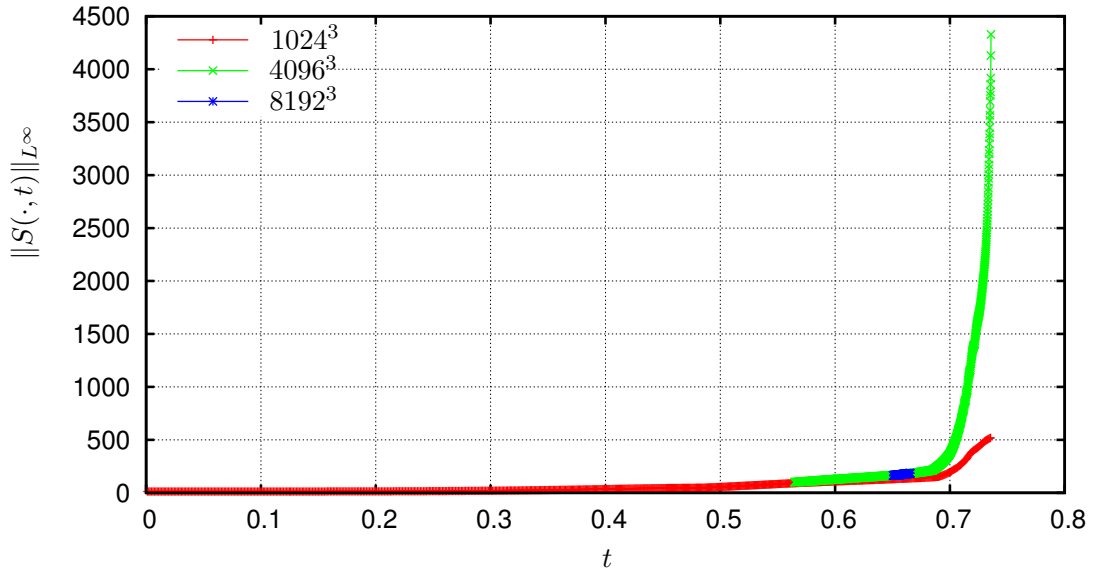


**Figure 5.10.**: Evolution of the norm of the strain tensor $\|S(\cdot, t)\|_{L^\infty}$ in time. The amplification is again by at least two orders of magnitude, starting at $\|S(\cdot, 0)\|_{L^\infty} = 12.4$. Strain was not measured for $2048^3$.

a point was anticipated by Pelz [82] as part of a point-wise singularity. This theory will be further addressed by geometrical means in section 5.4.4.

## 5.4.2. Beale-Kato-Majda

As stated in section 4.1.2, the BKM-criterion states, that no finite-time singularity can occur for the incompressible Euler equations up to time $T$, if

$$\int\limits_{0}^{T} \Omega(t)\mathrm{d}t \leq C\,. \tag{5.37}$$

As a consequence, the growth in time of $\Omega(t)$ has to fulfill $\Omega(t) \approx 1/(T-t)^{\gamma}$ with $\gamma \geq 1$ to be compatible with BKM.
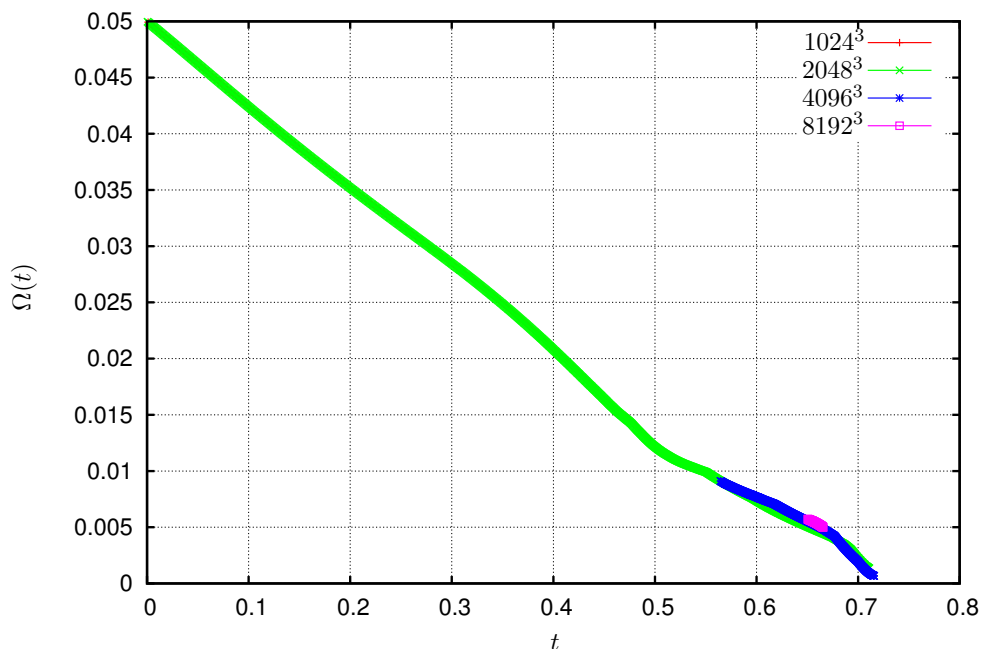


**Figure 5.11.**: Evolution of $1/\Omega(t)$ in time. This mode of plotting suggest a growth of $\Omega(t) \approx 1/(T-t)^{\gamma}$ with $\gamma = 1$ and a blowup time $T \approx 0.72$.

A plot of $1/\Omega(t)$ (by assuming $\gamma = 1$) is pictured in figure 5.11. At small times $t$, this graph looks straight, but the growth rate changes at least twice in the evolution of the flow. This can be explained by competing maxima in $|\boldsymbol{\omega}|$ overtaking the original $\Omega(t)$, thus changing the growth rate at different stages. Nevertheless, at no time the vorticity looks as though saturating, and in the latest stage of development suggests a blowup time of $T \approx 0.72$.

Numerical data of this kind has been interpreted as evidence in favor of the formation of a finite-time singularity before. Yet, even though the plot 5.11

is rather suggestive, the growth may as well be fitted to some fast (double) exponential growth.

### 5.4.3. Lagrangian evolution of pressure Hessian

As a theorem solely suited for flows obeying the Kida-Pelz symmetry, the Lagrangian blowup criterion of Ng and Bhattacharjee [78] was introduced in section 4.2.5. The computational framework developed to conduct the discussed simulations provides tools to monitor the Lagrangian evolution of fluid quantities with the help of passive tracer particles (section 3.4.1). Because of this, even though the criterion is in its nature rather distinct to the geometrical arguments constituting the core of this thesis, it was included as an additional tool to investigate the nature of dodecapole flows.

Summing up, the criterion connects the Lagrangian evolution of the second derivative of the pressure with respect to $x$, $\partial_{xx}p$, for some fluid element on the $x$-axis to the finite-time blowup of $\partial_x u_x$. The course of action, concerning the numerics, is as follows: At the start of the simulation, a number of tracer particles is initialized equally spaced on the $x$-axis. Due to the symmetry, $u_y = u_z = 0$ and the tracers stay on the axis indefinitely. Periodically, the position of all tracer particles, as well as $\partial_x u_x$ and $\partial_{xx}p$ at their position is written to the disk. A subsequent post-processing procedure then searches for particles that maintain stable positivity of $\partial_{xx}p$ as candidates for a blowup of $\partial_x u_x$ on the axis.

The number of particles injected into the flow at the beginning of the simulation is $10^6$, which results in roughly 100 particles per grid-cell on the highest complete grid level in the adaptive runs. Even though this may seem quite a lot, the particles thin out severely around the critical location at later times, which makes such a high particle count necessary.

Plotting $\partial_{xx}p$ and $\partial_x u_x$ at all particle positions at different times helps analyzing the situation. As plotted in figure 5.12, the influence of the vortex tubes on the values of $\partial_{xx}p$ and $\partial_x u_x$ is clearly identifiable and the propagation of the tubes can be observed. At later times, the maximum of $\partial_{xx}p$ increases rapidly, but the corresponding region of positivity collapses accordingly. Figure 5.13 (left) shows the values of $\partial_{xx}p$ at very late time. Even though particles cluster in regions of negative values, there nevertheless is a non-vanishing zone of extreme $\partial_{xx}p$. As visible in 5.13 (right), this has a direct consequence for $\partial_x u_x$. As expected, in the region of high $\partial_{xx}p$, the value for $\partial_x u_x$ does peak locally.

Yet, as derived in section 4.2.5, for $\partial_x u_x$ to blow up on the axis, $\partial_{xx}p$ has to be positive along a Lagrangian trajectory. Thus, it is necessary to identify those particles which maintain a positive value of $\partial_{xx}p$ for long time intervals. The result is depicted in figure 5.14 (left): Particles on the axis travel faster than the vortex tube center-lines, and even get accelerated further when entering the zone of extreme values for $\partial_{xx}p$. Because of that, each observed critical particle
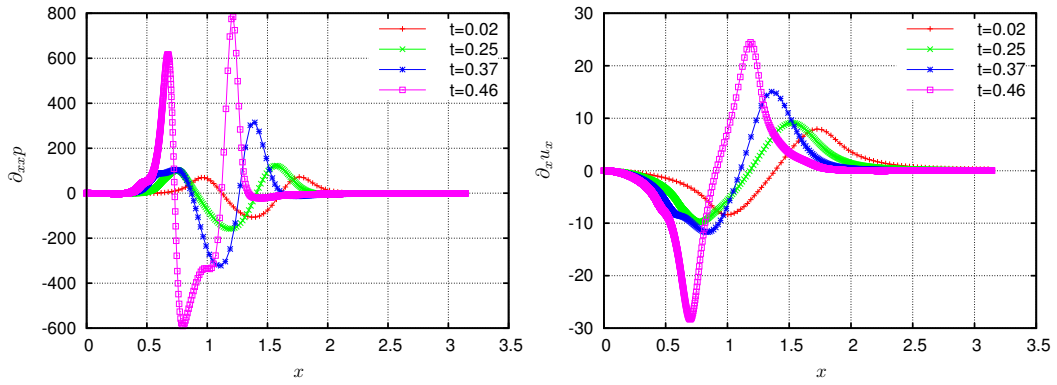
**Figure 5.12.**: Distribution of $\partial_{xx}p$ (**left**) and $\partial_x u_x$ (**right**) along the $x$-axis for different times.
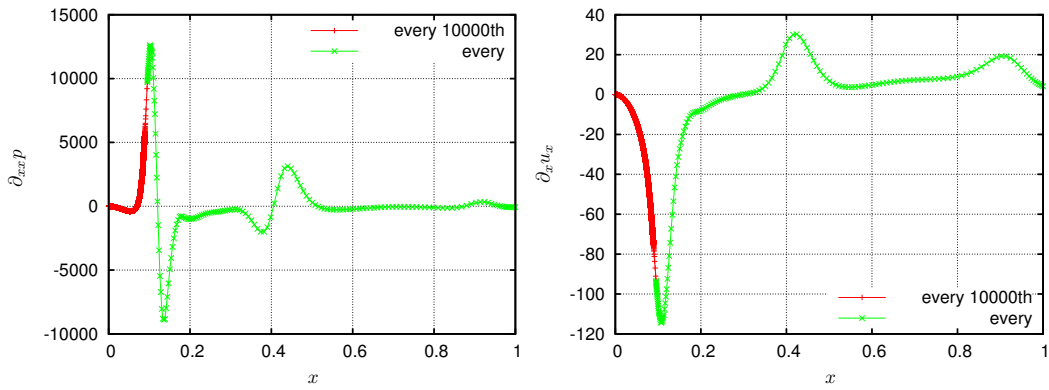


**Figure 5.13.**: Distribution of $\partial_{xx}p$ (**left**) and $\partial_x u_x$ (**right**) along the $x$-axis at very late time ($t = 0.7$).
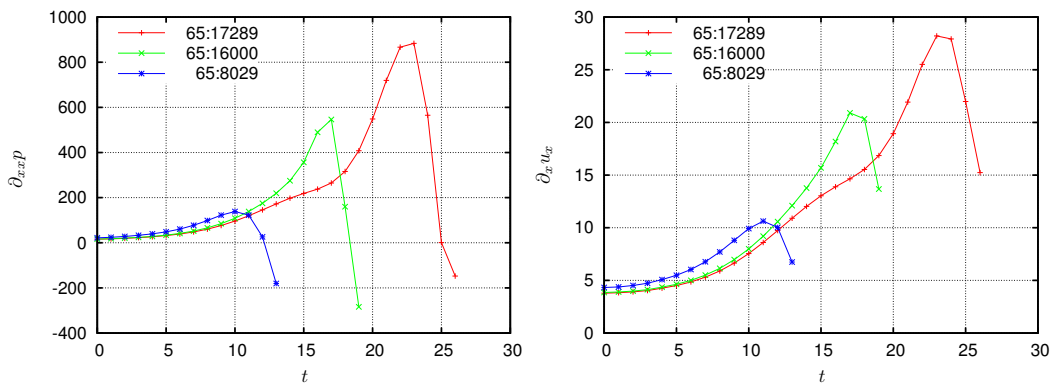


**Figure 5.14.**: Lagrangian evolution of $\partial_{xx}p$ (**left**) and $\partial_x u_x$ (**right**) in time.

leaves the region of positive $\partial_{xx}p$ eventually. Consequently, as depicted in figure 5.14 (right), $\partial_x u_x$ does initially grow, but breaks down as soon as the critical zone is left.

Summing up, even though the number of advected particles was quite high, no particle fulfilling the criterion of Ng and Bhattacharjee [78] could be identified and the existence of a blowup of $\partial_x u_x$ seems unlikely from a numerical point of view. This is hardly surprising, since the vortex dodecapole formation by design favors a possible blowup at the core of the vortex tubes (where the maximum vorticity is attained), instead of on the coordinate axes. Therefore, the informative value of this theorem for the considered case is limited and the results for the geometric criteria presented in the following sections are more conclusive.

## 5.4.4. Geometry of the critical vortex line

In section 4.2.2, the regularity of the vorticity direction field along vortex lines was considered as a relevant indicator for vorticity accumulation. Specifically it was stated by theorem 1 of Deng et al. [30], that a blowup of vorticity in any point $\mathbf{x}$ is impossible as long as for some $\mathbf{y}$ on the same vortex line uncritical growth of vorticity is observed and along the vortex line connecting $\mathbf{x}$ to $\mathbf{y}$ the quantity $\nabla \cdot \boldsymbol{\xi}$ remains bounded.

There is considerable freedom in the choice of $\mathbf{x}(t)$ and $\mathbf{y}(t)$, which has to be narrowed down for the implementation in numerical simulations. An obvious choice for $\mathbf{x}(t)$ is the location of the maximum of vorticity $\Omega(t)$. This allows inferring the global growth from the local behavior of the considered vortex line. For $\mathbf{y}(t)$, any point on the same vortex line sufficiently well separated from the collapsing critical regions seems appropriate. This choice was already considered by the creators of the theorem:

> "Let us take the point $\mathbf{x}(t)$ to be the point inside one tube where the maximum vorticity is attained, and $\mathbf{y}(t)$ to be a point on the same vortex line, but outside the tube. It is easy to check that within this inner region, condition (2.1) [boundedness of $\nabla \cdot \boldsymbol{\xi}$] is satisfied. By Theorem 1 we see that if the maximum vorticity *outside* these small tubes is integrable in time, then there is no blowup inside the tubes. It is likely that the maximum vorticity outside these small tubes has a growth rate smaller than that inside these small regions. This casts doubt on the validity of Pelz's claim..." [30]

In fact, the authors admit that even though it is "likely" for the vorticity outside the innermost region to be well-behaved, a numerical simulation comparing the growth-rates for different points a vortex line is necessary to verify

the assumptions. It is the primary purpose of this section to establish that even though the outer regions, as the plots in section 5.3 suggest, appear to the naked eye to be mild in growth, in fact exhibit identical growth rates as the core region. As a consequence, the situation for the dodecapole initial conditions is not as easy as the quotation from [30] suggests.
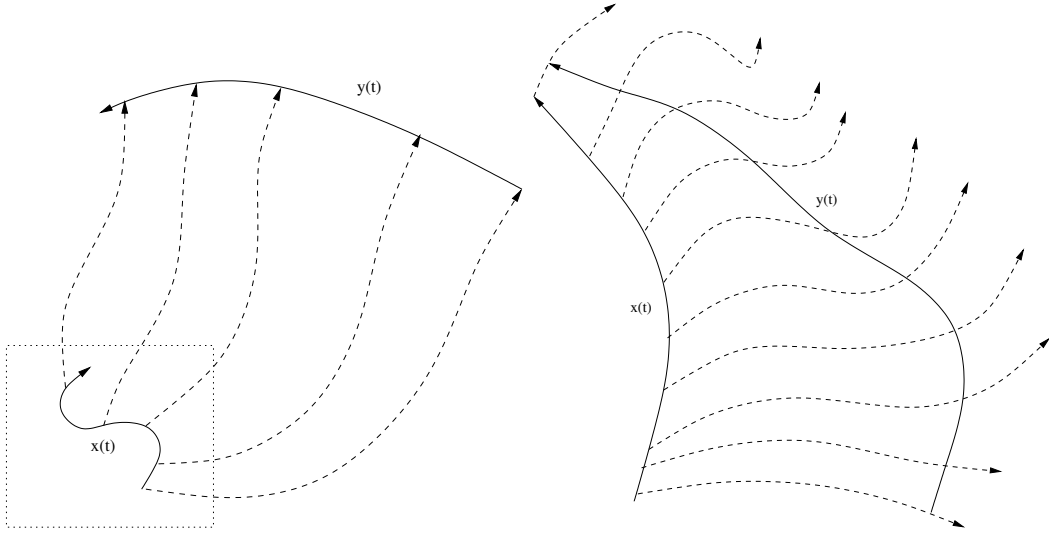


**Figure 5.15.**: Two different ways of making use of theorem 1. **Left:** Critical growth of vorticity in a critical region is connected to mild growth of vorticity far outside. **Right:** Constant convergence along the vortex line segment to distinguish between point-wise collapse and blowup of the complete segment.

The approach to theorem 1 employed in this work is slightly different (compare figure 5.15). Instead of arbitrarily choosing $\mathbf{y}(t)$ somewhere far away from the critical region, define $\mathbf{y}(t)$ via

$$\int\limits_{\mathbf{x}(t)}^{\mathbf{y}(t)} \nabla \cdot \boldsymbol{\xi} \mathrm{d}s = C \tag{5.38}$$

for some constant $C$ independent of the time $t$, where $s$ denotes the arc-length parameter of the curve from $\mathbf{x}(t)$ to $\mathbf{y}(t)$. In words, choose $\mathbf{y}(t)$ on the same vortex line as $\mathbf{x}(t)$ such that the accumulation of tightening of nearby vortex lines is the same for every instance in time. This provides us with the ability to clearly distinguish between to separate cases of supposed blowup:

1. For every constant $C$, $\mathbf{y}(t)$ approaches $\mathbf{x}(t)$ in finite time to collapse to a single point. This would constitute the desired behavior for a point-wise singularity in the origin.

2. If for any constant $C$, $\mathbf{x}(t)$ and $\mathbf{y}(t)$ stay well separated in time and do not collapse to a point, the whole vortex-line from $\mathbf{x}(t)$ to $\mathbf{y}(t)$ has to blow up in order to maintain critical growth in $\mathbf{x}(t)$. This scenario, however unlikely, is not analytically ruled out.

If there is no approach of $\mathbf{y}(t)$ to $\mathbf{x}(t)$ and the growth rate of $|\boldsymbol{\omega}(\mathbf{y}(t),t)|$ is clearly uncritical, a singularity is obviously ruled out by theorem 1.

Numerically, this test was implemented as follows:

- At each timestep, identify the point of maximum vorticity as $\mathbf{x}(t)$.

- Follow the vorticity direction vector field while integrating $\nabla \cdot \boldsymbol{\xi}$ along the path. This is done with a third-order Runge-Kutta integrator in space.

- As soon as the integrated quantity exceeds the threshold $C$, identify the current location on the vortex line as $\mathbf{y}(t)$. To increase precision, the endpoint is found via bisection.

- Geometric properties and diagnostics for the vortex line segment are written to the disc, especially its length and $|\boldsymbol{\omega}(\mathbf{y}(t),t)|$ to distinguish the cases introduced above.

This procedure is carried out for the whole time interval, as long as the simulation is well resolved. The constant $C$ is chosen in a reasonable way to achieve a length of the vortex line segment that fits into the computational domain in the beginning of the simulation, but is still well resolved at the chosen resolution at later times. Hence, the whole vortex line segment is resolved reliably throughout the simulation.

The results for the Grauer dodecapole are presented in figure 5.16 for different constants $C \in \{0.25, 0.5, 1, 2\}$. Initially, the vortex line segments do not accumulate enough $\nabla \cdot \boldsymbol{\xi}$, so that the length is bounded by the size of the computational domain ($\mathbf{x} \in [0, \pi]^3$). At some point, depending on the value of $C$, the threshold is reached and the length of the vortex line segment decreases. Yet, for all considered cases of $C$, the length does not collapse to a point, but saturates at early times without approaching $l(t) = 0$. This behavior appears to be stable up to the latest time of the simulation. The final length of the vortex line segments is at least 0.3 for the smallest case of $C$ ($C = 0.25$), which is still well resolved with at least $200 \, \Delta x$ for the simulation with $4096^3$ grid points. This result, therefore, is a numerical evidence against a point-wise blowup for the vortex dodecapole class of initial conditions. This is in concordance with the estimate by Deng et al. [30].

Yet, monitoring the development of $\boldsymbol{\omega}(\mathbf{y}(t),t)$ yields, as shown in figure 5.16 (right), a similar growth rate for the accumulation of vorticity at the endpoint as for the beginning of the vortex line segment. This is hardly surprising, since by
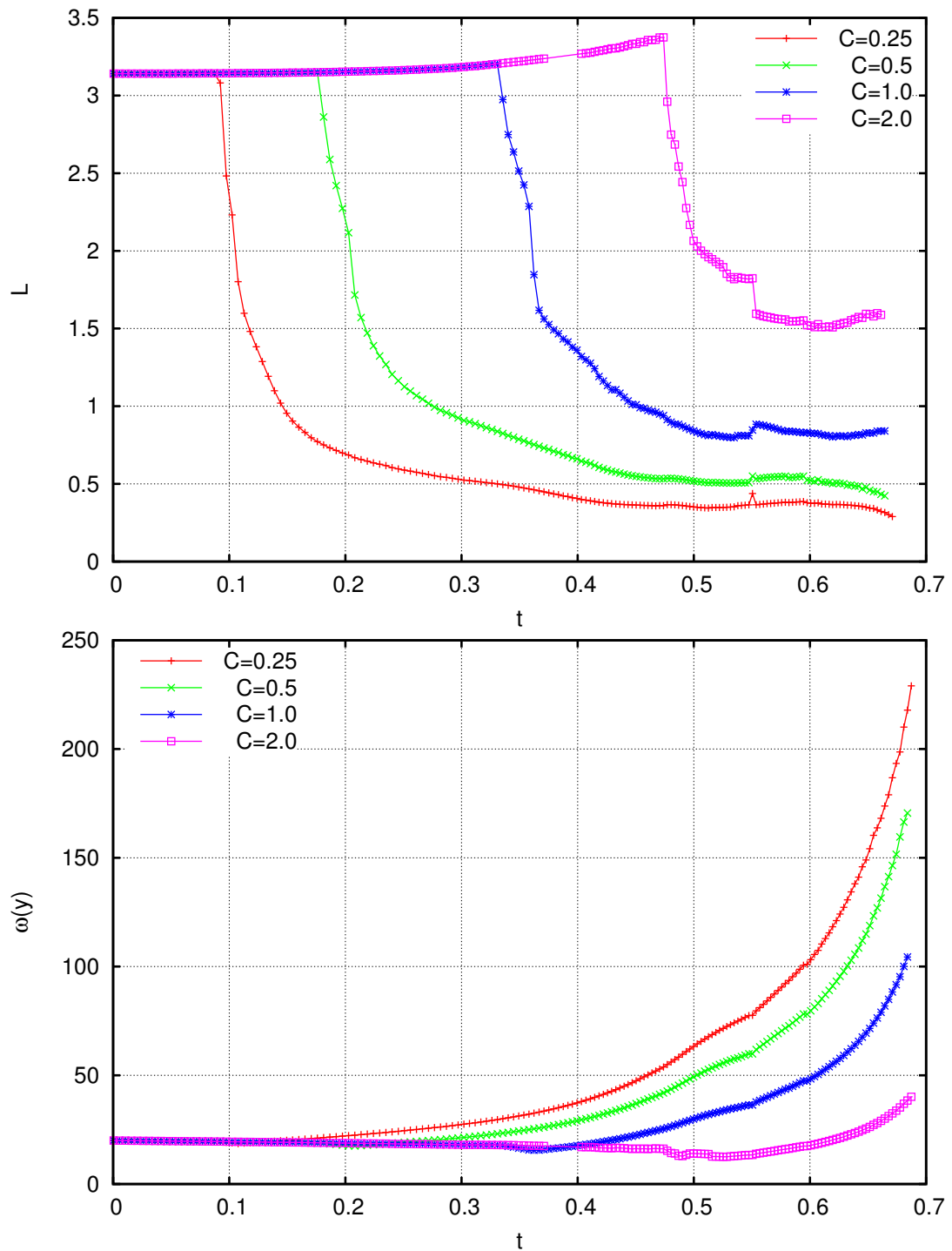
**Figure 5.16.: Top:** Length of the vortex lines starting at position **x** of maximum vorticity for constant $C = \int_x^y \nabla \cdot \xi \mathrm{d}s$. **Bottom:** Vorticity at the endpoint $y$ of these vortex line. Once satiated, the growth rate is the same for all $y$.
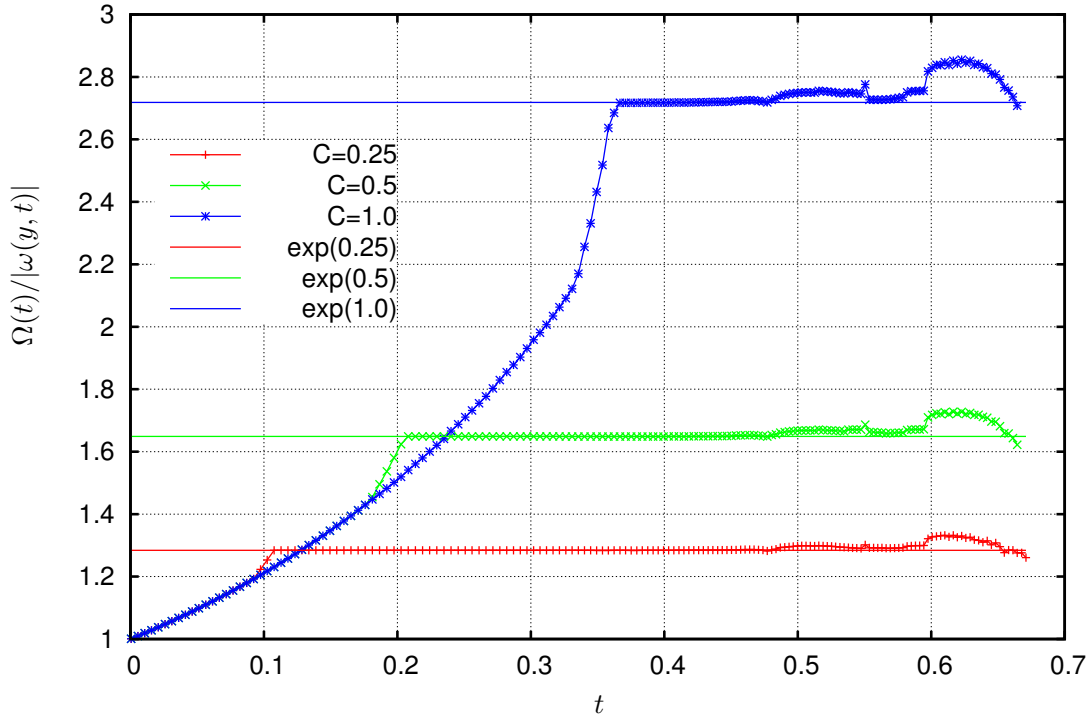
**Figure 5.17.**: Confirmation of connected growth rates along a vortex line. The growth rate relation $|\boldsymbol{\omega}(\mathbf{y}(t),t)|/|\boldsymbol{\omega}(\mathbf{x}(t),t)|$ agrees well with the theoretical value of $\exp(C)$.

construction a constant value for $C$ directly links the growth rates of $|\boldsymbol{\omega}(\mathbf{x}(t),t)|$ to $|\boldsymbol{\omega}(\mathbf{y}(t),t)|$. Nevertheless, a numerical verification of this analytic equality may be seen as a confirmation that the observed growth rate of $|\boldsymbol{\omega}(\mathbf{x}(t),t)|$ is by no means a numerical artifact in an isolated small area, but is reproduced at points far away from the critical region, which appear to be well-behaved at first view. The possibly critical growth in the perspective of BKM is, thus, confirmed by the global flow.

Furthermore, since for a large portion of the simulation the distance $l(t)$ is approximately constant, this can be seen as an evidence for the existence of a non-vanishing vortex line segment that blows up in every point. Thus, contradicting the estimation of Deng et al. [30], the possibility of a blowup of the vortex dodecapole flow is not excluded by theorem 1.

The popular scenario of a collapse to a single point, on the other hand, is clearly conflicting the numerical evidence. Adding to the conclusion of section 5.3 this is a further result against the formation of a locally self-similar scenario as presented in section 5.1.2: The critical region of accumulating vorticity does not collapse in a way compatible with equation (5.9) for reasonably small $h$. To fulfill the scaling requirements of the Euler equation for large $h$, the velocity

field **u** therefore would have to blow up in time as $1/(T - t)$.

The discovery of a possibly critical vortex line segment in the vortex dodecapole flow, however, is afflicted with the blemish, that distinguishing between critical and sub-critical blowup of the whole segment is in no way more conclusive than distinguishing between critical and sub-critical growth of $\Omega(t)$. Thus, learning from the lesson taught by 25 years of numerically testing BKM, this should not be interpreted as clear evidence in favor of a finite-time singularity.

As confirmation of the reliability of the numerics, figure 5.17 shows the relative growth rate of $|\boldsymbol{\omega}(\mathbf{y}(t), t)|$ with respect to $|\boldsymbol{\omega}(\mathbf{x}(t), t)|$. As required by the analytical result,

$$\frac{|\boldsymbol{\omega}(\mathbf{y}(t), t)|}{|\boldsymbol{\omega}(\mathbf{x}(t), t)|} = \exp(C), \tag{5.39}$$

this behavior is well reproduced by the numerics.

## 5.4.5. Lagrangian evolution of the critical vortex line segments

The geometric properties of Lagrangian vortex line segments, especially their curvature $\kappa$ and the tightening of their surroundings $\nabla \cdot \boldsymbol{\xi}$ have been established as essential parameters in understanding the nature of rapid accumulation of vorticity in Euler flows. The theoretical background, as presented in section 4.2.4, leads to the formulation of theorem 2 of Deng et al. [30, 31] as a blowup criterion. The ambition behind this is to utilize these geometric properties, monitored in a numerical simulation, as more reliable means of distinguishing between a finite-time singularity and a mere fast accumulation of vorticity.

Despite high hopes from an analytical point of view that these considerations will shed light on the true nature of vorticity accumulation, numerical results observing geometrical properties of Lagrangian vortex filaments are scarce. This is primarily due to the fact that Eulerian quantities such as $\Omega(t)$ are readily trackable in post-processing, while monitoring the Lagrangian evolution requires additional computational effort. On top of that, the geometry of integral curves at an instance in time, though in principle computable in post-processing, as well as derived quantities such as their convergence and curvature, are quite inaccessible in comparison to simple Eulerian criteria.

This section is devoted to the presentation of results concerning the assumptions of theorem 2 of Deng et al. [30] for vortex dodecapole initial conditions. Quite similar to the previous section, there is considerable freedom in the choice of the involved quantities. Deng et al. [31] recommend following the vortex line on which the maximum vorticity is attained. This is impossible for the considered flow, since the Eulerian maximum of the vorticity is not advected, but changes the vortex line in time. The strategy chosen in the context of this work

therefore is as follows:

- Identify the Lagrangian fluid element $\boldsymbol{\alpha}$, which will contain the maximum of vorticity at the latest time of the simulation, $\Omega(t) \approx |\boldsymbol{\omega}(\mathbf{X}(\boldsymbol{\alpha}, t), t)|$. A vortex line segment $L_t$ starting here will intrinsically be "comparable" to the maximum of vorticity (as in $|\boldsymbol{\omega}(\mathbf{X}(\boldsymbol{\alpha}, t), t)| \gtrsim \Omega(t)$) at late stages of the simulation. The assumptions concerning the segment are therefore automatically met. In the numerics this procedure is implemented by carrying out a precursory identical simulation with a huge number of tracer particles ($\approx 1$ million) randomly distributed across the domain. Particles that accumulate huge amounts of vorticity are selected for the production run.

- At each instance in time, start a vortex line integration at $\mathbf{X}(\boldsymbol{\alpha}, t)$ along the vorticity direction field. Monitor the maximum curvature $\|\kappa\|_{L^\infty(L_t)}$ and the maximum vortex line convergence $\|\nabla \cdot \boldsymbol{\xi}\|_{L^\infty(L_t)}$ during the integration and calculate $\lambda(t)$. Stop the integration, as soon as $\lambda(t)$ reaches a fixed, arbitrary constant $C$. This defines $L_t$. In the numerics this is again implemented with a third-order Runge-Kutta integration and bisectioning to obtain the endpoint of $L_t$.

- For this vortex line segment $L_t$, calculate the length $l(t)$, and the velocity components $U_n$ and $U_\xi$. From the collapse of the length $l(t)$ approximate the exponent $B$. This in turn provides the critical growth exponent $A$ for the velocity variables, $A_{\text{crit}} = 1 - B$.

- Compare the increase in $U_n$ and $U_\xi$ to $1/(T-t)^{A_{\text{crit}}}$ to distinguish between critical and sub-critical growth of velocity.

This can be interpreted rather intuitively. By prescribing an arbitrarily fixed $\lambda(t)$, the vortex line segment is kept relatively geometrically uncritical, as the length-scale is always adjusted accordingly. This process of "zooming in" just enough to retain the geometric "criticalness" prescribes the rate of collapse to a point, at least in the direction of the vortex line. All that is left to check is whether the velocity growth in the immediate surrounding is fast enough to be compatible with a finite-time singularity.

The results of the previous section, concerning a point-wise singularity versus the blowup of a whole vortex segment, already anticipates, that the increase in $\nabla \cdot \boldsymbol{\xi}$ around the critical vortex line is bounded. If the curvature of the vortex line segment remains controllable (which is to be expected from the pictures), then just a mild collapse of $l(t)$ occurs. This leaves much room for $U_n$ and $U_\xi$ to still be distinguishable from a critical growth.

Figure 5.18 shows the results for the Grauer dodecapole initial conditions. Pictured is the length of the vortex line segment for the tracer that is arriving
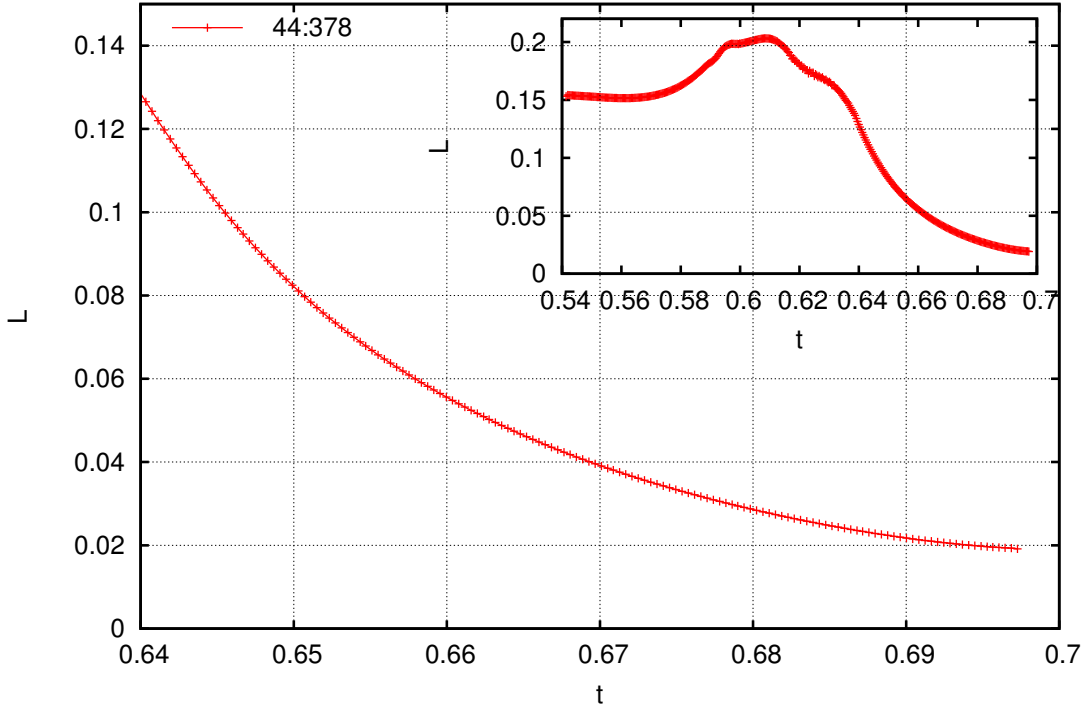
**Figure 5.18.**: Evolution of the length $l(t)$ of the critical vortex filament $L_t$ for different Lagrangian fluid elements. The length does not decrease as $(T-t)^B$ for any $B < 1$, which would be faster than linear. The Lagrangian collapse of the vortex segment is decelerating instead.

at a position of very huge vorticity at late stages of the simulation. The subplot depicts the long-term behavior of the particle entering the critical region, while the final stage of length decrease is magnified. The decrease in length does not agree with a collapse in final time, but instead the shrinkage of the segment decelerates clearly in time. This contradicts a scaling in time proportional to $(T-t)^B$ for any $0 < B \leq 1$, which would be faster than (or, in the limiting case, equal to) linear. It should be noted, that for the observed collapse in length, the vortex segment curvature $\kappa$ is the dominating term in $M(t) = \max(\|\nabla \cdot \boldsymbol{\xi}\|_{L^\infty(L_t)}, \|\kappa\|_{L^\infty(l_t)})$, shadowing the effects of $\nabla \cdot \boldsymbol{\xi}$. This may lead to a change of regime in the rate of collapse, if $\nabla \cdot \boldsymbol{\xi}$ at some point exceeds $\kappa$ in quantity.

It could furthermore be argued that the limit $B \to 0$ is hard to exclude, since the drop in length would be virtually instantaneous in time, with a close to constant scaling before. In this limit, the quantities $U_n$ and $U_\xi$ would have to grow roughly as $1/(T-t)$ to still allow formation of a finite-time singularity.

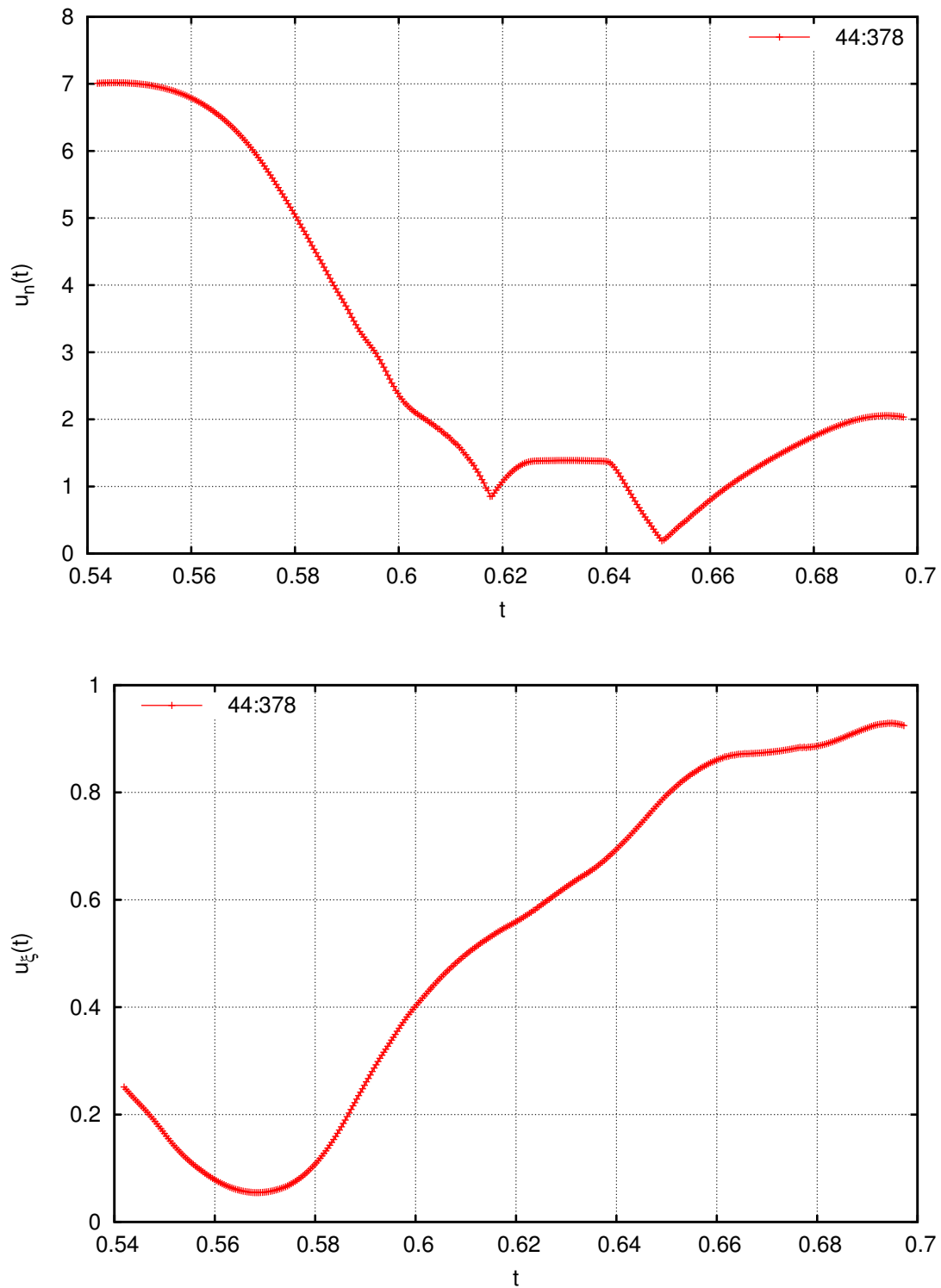The quantities $U_n$ and $U_\xi$ where defined in section 4.2.4 as

**Figure 5.19.**: Evolution of the quantities $U_n$ (**top**) and $U_\xi$ (**bottom**) in time. $U_n$ does not appear to be growing, while $U_\xi$, though increasing in time, does not exhibit a finite-time blowup as $1/(T - t)$.

$$U_\xi(t) = \max_{\mathbf{x},\mathbf{y}\in L_t} |(\mathbf{u}\cdot\boldsymbol{\xi})(\mathbf{x},t) - (\mathbf{u}\cdot\boldsymbol{\xi})(\mathbf{y},t)|$$
$$U_n(t) = \max_{L_t} |\mathbf{u}\cdot\mathbf{n}| \ .$$

$U_\xi$ quantifies the largest difference in axial velocity along the segment. For an isolated collapsing vortex tube, this quantity can be expected to not increase critically, since the tangential velocity is less likely to rapidly change than the radial velocity. However, this initial explanation does not consider the influence of the mirror tubes. $U_n$ on the other hand may be interpreted as the velocity of the vortex tube's core itself. Again, in an isolated setup this velocity is not expected to blow up.

Figure 5.19 shows the observed behavior of $U_n$ and $U_\xi$ in time for the tracer as considered above. $U_n$ stays roughly constant in time, showing no signs of a blowup. $U_\xi$, even though increasing in time, does not fit to critical growth, in particular not like $1/(T-t)$ in time. Thus, the assumptions of theorem 2 are well met. Excluding a change of regime in this late state of the simulation, this therefore poses a strong evidence against a finite-time singularity for the class of vortex dodecapole initial conditions.

# 6. Summary

This work presents numerical evidence against the formation of a finite-time singularity for the vortex dodecapole initial condition. It uses data obtained from high resolution adaptively refined numerical simulations to test the assumptions presented by geometric blowup criteria.

In the course of this work, a numerical framework has been extended to allow the integration of the incompressible three-dimensional Euler equations on adaptively refined grids, which supports the diagnostics of geometrical and Lagrangian criteria and scales close to optimal, as well as outputs with good performance, on massively parallel machines.

The Euler equations for incompressible fluids are known for more than 250 years. Nevertheless, the question of the existence of smooth solutions for smooth initial conditions is not answered. With the advent of scientific computing, analytical results are accompanied by numerical simulations, which are used to gain insight into the evolution of flow structures and the interplay between physical quantities. In recent times, numerical simulations have become an indispensable tool for the assessment of relevance and applicability of numerical theorems to the actual flow. Nevertheless, rigorous proof has to be given in mathematical terms, and numerical results can just be used as evidence and clue, pointing in the general direction to be taken analytically.

Next to classical results such as BKM, recently the geometric analysis of the flow [30, 31] has played a role in distinguishing finite-time singularities from flows that exhibit merely fast accumulation of vorticity. This approach, applied to numerical simulations, may provide clearer insight into the possible formation of the singularity. Most notably, it implies numerical techniques to distinguish between a point-wise blowup and the blowup of a whole vortex line segment: Monitoring a vortex line which maintains a fixed convergence of neighboring lines, $\int \nabla \cdot \boldsymbol{\xi} = 0$, the absence of a collapse must coincide with a blowup of vorticity along the whole segment, if one wants to stick to the formation of a finite-time singularity. Furthermore, as shown in section 4.2.4, if a blowup of curvature and $\nabla \cdot \boldsymbol{\xi}$ is not observed, then components of the velocity have to scale like $1/(T-t)$. Since in numerical simulations, velocity growth is usually far from that, this argument can be used against critical accumulation of vorticity much more clearly than the usual approach via BKM .

Generally, a singularity in the Euler equations is believed to be point-wise and supposedly locally self-similar. Analytical results investigating the bounds

of such scenarios are quite scarce for the Euler equations, yet recently several cases relevant to numerical simulations have been ruled out [13, 14]. By far the most important process in the formation of singularities in finite time is the coupling of vorticity and strain. If the vorticity aligns with the eigenvector of the strain matrix with positive eigenvalue long enough, and if that eigenvalue grows alongside the vorticity, then the accumulation of vorticity may lead to a finite-time blowup compatible with BKM. It is not known to date, whether internal mechanisms render such amplification impossible. Yet, it is known from turbulence research that the mentioned alignment is at least unlikely in a natural context [1]. It is now the mission of the physicists to design initial conditions which exhibit and maintain, despite its inherent instability, a period of vorticity-strain coupling long enough to cause the blowup.

Several such candidates are proposed in the literature [6, 52, 59, 90]. A perturbed vortex tube as well as anti-parallel vortex tubes are afflicted with the inconvenience to require the curvature in the plane to blow up alongside the vorticity [82]. This is due to the fact that an amplification of the strain with the same growth rate as the vorticity can be connected via the Biot-Savart law to the requirement to kink infinitely at the location of maximum vorticity. On the other hand, due to axial stretching of the vortex tube, a growing strain reduces the curvature in the plane of symmetry. These counteracting processes may limit the ability of the aforementioned initial conditions to maintain vorticity-strain coupling over a period of time long enough for the formation of a singularity in finite time.

The class of high-symmetry flows, and most notably among them the vortex dodecapole configuration, does not suffer from the above mentioned disadvantage: Here, the strain imposed on the vortex tubes in the plane of symmetry is induced by the rotational images [82]. Axial strain is not dictated by the curvature and the above canceling does not take place. This renders the vortex dodecapole initial condition to be one of the most promising in terms of singularity formation known today.

This is the reason why this work is concerned with the numerical simulations of vortex dodecapole initial conditions, and more specific with Grauer or Lamb vorticity profiles. Comparison of the simulation shows that different vorticity profiles yield similar visual and geometrical appearance. This serves as an argument that the obtained results may apply to the whole class of vortex dodecapole flows. Monitoring the growth rate of $\Omega(t)$ quantifies the well-known vorticity amplification. Amplification by more than two orders of magnitude was reached for both vorticity and strain, exceeding by far values achieved by previous simulations [41]. Applying this data to BKM would lead to the conclusion that a finite-time singularity at time $T \approx 0.72$ fits via extrapolation. Yet, as the history of Euler simulations has shown, statements obtained by extrapolation are to be handled with care.

Following the argument given in section 5.4.4, a point-wise collapse should coincide with a blowup of $\nabla \cdot \boldsymbol{\xi}$ at the point of maximum vorticity. This statement can be broadened: A finite-time singularity must either lead to a blowup of $\nabla \cdot \boldsymbol{\xi}$ at the point of maximum vorticity, or the whole critical vortex line segment has to blow up. Utilizing the geometric information obtained via vortex line integration from the numerical simulation, it is observed that $\nabla \cdot \boldsymbol{\xi}$ does not grow in a way to be compatible with a point-wise collapse. Yet, measuring the growth-rates on the critical vortex line, high rates of amplification are measured far away from the critical region. Even though it is hard to distinguish, whether this amplification is critical or sub-critical, this might be interpreted as an evidence for the blowup of the complete vortex line segment (even though it suffers exactly the same vulnerabilities as extrapolation in BKM). A point-wise blowup, on the other hand, seems to contradict the numerical results up to the time reached.

Evidence against a blowup of the whole critical vortex line segment is found when looking at the geometric properties of Lagrangian vortex line segments. It was shown by theorem 2 in [30] that a blowup of vorticity is directly connected to the interplay between velocity growth and the collapse of vortex line filaments, when maintaining the overall same shape in geometric means (i.e. the same $\lambda(L_t)$). Since curvature and $\nabla \cdot \boldsymbol{\xi}$ do not increase in order to support a finite-time collapse of the segment, velocity components in the vicinity of the vortex line filament would have to increase as $1/(T-t)$ to support the blowup hypothesis. Up to the time reached, critical growth may be excluded by numerical means. This poses a numerical evidence against the formation of a singularity in finite time for vortex dodecapole configurations.

# A. Grid structure and notation

A numerical problem is defined on a spatial domain $\Omega \subset \mathbb{R}^d$ of dimension $d$ with arbitrary form. The framework is restricted to $d = 3$ and rectangular domains only. The notation will be introduced for two dimensions due to readability, but can readily be extended to three dimensions. With $h \in \mathbb{R}^2$ being the *grid spacing vector* $h = (h_x, h_y)$ we define the *infinite grid*

$$G_h := \{(x_i, y_j) \in \mathbb{R}^2 | x = ih_x, y = jh_y; i, j \in \mathbb{Z}\}$$

and respectively for other dimensions $d$. With $\Omega_h := \Omega \cap G_h$ we denote our discrete computational domain or *grid*. For $h_x = h_y = h$ we call our grid a *square grid*.

Any **discrete function** $f_h : \Omega_h \mapsto \mathbb{R}$ can now be described by the simple notation

$$f_{i,j} := f_h(x_i, y_j) = f_h(ih_x, jh_y).$$

For **discrete operators** $L : \Omega_{h_1} \mapsto \Omega_{h_2}$ operating on a discrete function $f_{h_1}$ on the grid $\Omega_{h_1}$ it is convenient to introduce the *stencil notation* by calling

$$[s_{i,j}] = \begin{bmatrix} & \vdots & \vdots & \vdots & \\ \cdots & s_{-1,1} & s_{0,1} & s_{1,1} & \cdots \\ \cdots & s_{-1,0} & s_{0,0} & s_{1,0} & \cdots \\ \cdots & s_{-1,-1} & s_{0,-1} & s_{1,-1} & \cdots \\ & \vdots & \vdots & \vdots & \end{bmatrix}$$

the *stencil* of $L$, if

$$Lf_{m,n} = \sum_{(i,j)} s_{i,j} f_{m+i,n+j}$$

for any $f : \Omega_{h_1} \mapsto \mathbb{R}$ and $m, n \in \mathbb{Z}$. All these notations are easily generalized to any dimension $d$. It will be used in the following paragraphs for the description of the multigrid algorithm.

# B. Multigrid

In this section, the implementation of the multigrid algorithm to the framework *racoon III* is described. For a broader look on the topic of multigrid algorithms, see, for example, the books by Trottenberg et al. [91] or Briggs et al. [10].

Despite the fact that just the Poisson equation will be treated here, it is convenient to introduce an abstract notation. Consider the system of linear equations

$$Lv = f, \tag{B.1}$$

with a linear operator $L$, the right-hand-side $f$ and the exact and supposedly unique solution $v$. With $u$ being an approximation of the solution, we define the difference to the exact solution, the (algebraic) *error*, by

$$e = v - u \tag{B.2}$$

and the *residual* or *defect* by

$$r = f - Lu. \tag{B.3}$$

From the uniqueness of the exact solution it follows directly that a vanishing error is equivalent to a residual equal to zero. Furthermore it is easy to see that the original problem $Lv = f$ is equivalent to the so called *defect equation* $Le = r$ (which only holds as long as $L$ is linear). As the numerical problem is discrete rather than continuous, the index $h$ on each variable or operator denotes the grid spacing, so the main equation becomes

$$L_h v_h = f_h \qquad \text{or} \qquad L_h e_h = r_h \tag{B.4}$$

on the discrete domain (*grid*) $\Omega_h$. For details on the notation used in this section, see Appendix A.

The multigrid idea is based on combined error smoothing on multiple grids with different grid spacing. Thus, the main principles are *error smoothing* (relaxation) and *coarse grid correction*, which both will shortly be discussed in the following pages. Subsequently it is shown how both parts are interlinked to form a complete multigrid cycle.

## B.1. Smoothers

Consider a square grid $\Omega_h$ with grid spacing $h$. By $u_{i,j}^n$ we denote the current approximation $u$ at $(x_i, y_j) \in \Omega_h$ at iteration step $n$. The discrete *finite difference*

two-dimensional Poisson equation now looks like

$$\frac{1}{h^2}(u_{i-1,j}^n + u_{i+1,j}^n + u_{i,j-1}^n + u_{i,j+1}^n - 4u_{i,j}^n) = f_{i,j} \tag{B.5}$$

and can be solved for $u_{i,j}^n$ to be used iteratively:

$$u_{i,j}^{n+1} = \frac{1}{4}(u_{i-1,j}^n + u_{i+1,j}^n + u_{i,j-1}^n + u_{i,j+1}^n - h^2 f_{i,j}) \tag{B.6}$$

or, in stencil notation:

$$u_{i,j}^{n+1} = \frac{1}{4}\begin{bmatrix} & 1 & \\ 1 & 0 & 1 \\ & 1 & \end{bmatrix} u_{i,j}^n - \frac{h^2}{4}f_{i,j} \tag{B.7}$$

This type of iteration is called the *Jacobi iteration* (JAC). By damping the smoothing by a factor $\omega$,

$$u_{i,j}^{n+1} = \omega(\frac{1}{4}\begin{bmatrix} & 1 & \\ 1 & 0 & 1 \\ & 1 & \end{bmatrix} u_{i,j}^n - \frac{h^2}{4}f_{i,j}) + (1 - \omega)u_{i,j}^n$$

$$= \frac{\omega}{4}\begin{bmatrix} & 1 & \\ 1 & 4(\frac{1}{\omega} - 1) & 1 \\ & 1 & \end{bmatrix} + \frac{h^2\omega}{4}f_{i,j},$$

one obtains the $\omega$-*Jacobi iteration* ($\omega$-JAC). If applied several times, like shown in figure B.1, the error of the approximation becomes *smooth*. It takes quite a lot of steps for the error to become small, but after very few steps (just one or two) the high frequency noise of the error is already damped. This key observation will be used later on. Of course for the case $\omega = 1$ $\omega$-JAC is equivalent to plain JAC-iteration. In practice, however, a choice of $\omega = 0.8$ yields the best results regarding convergence rates, slightly depending on the problem and initial conditions. A detailed mathematical analysis of the smoothing properties of $\omega$-JAC can be found in section 2.1.2 of [91].

There are several smoothers, differing in properties like convergence rate, stability and scaling behavior. I will very briefly introduce three of them, all of which were successfully implemented into the program.

### B.1.1. Gauss-Seidel-type iterations

Easier to implement, superior in convergence rate (or more importantly *smoothing properties*) and memory usage, but more difficult to handle mathematically are the so called *Gauss-Seidel-type relaxation methods*. While in JAC-type iterations the whole field is updated at once, here the smoothing occurs in a
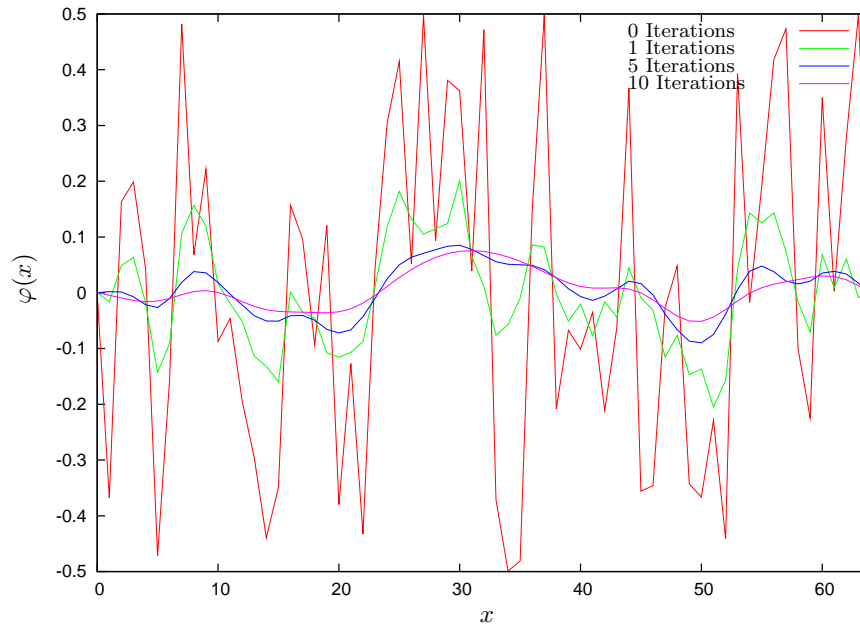
**Figure B.1.**: Smoothing behavior for a random function with $\omega$-JAC. High frequency modes are damped fast, large-scale fluctuations deplete very slow.

determined ordering. Because of this, the already updated values are reused and there is no need to store the field twice. The most natural way to sweep through an array of values is lexicographic, which leads to the *Gauss-Seidel Lexicographic* smoother (GS-Lex):

$$u_{i,j}^{n+1} = \frac{1}{4}(u_{i-1,j}^{n+1} + u_{i+1,j}^{n} + u_{i,j-1}^{n+1} + u_{i,j+1}^{n} - h^2 f_{i,j}), \qquad \text{(B.8)}$$

which is outlined in figure B.2 (left). GS-Lex in general shows higher convergence rates than any JAC-type iteration, but breaks the symmetry of the problem, as the lexicographic sweep through the field is itself asymmetric.

The *Gauss-Seidel Red/Black* (GS-RB) smoother takes this idea one step further. The computational domain is divided into *odd* and *even* grid points, shown in figure B.2 (right) (which resemble the black and red fields of a checkerboard, hence the name) and each group of cells is updated as a whole. Thus all four grid points accessed in the black sweep have already been updated in the red sweep right before. In practice, GS-RB shows the highest convergence rate, but because of the double sweep, it also requires more computation time (in a massively parallel environment it requires twice as much communication, see section 3.5.4).

Technically, equipped with just a smoother the Poisson equation could be solved in several thousand iteration steps, depending on the resolution. The
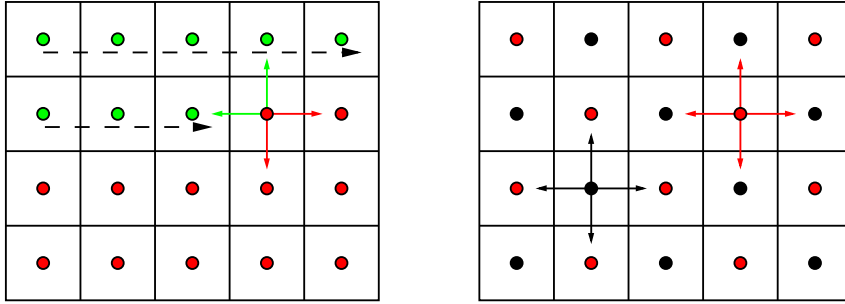
**Figure B.2.**: **Left:** Lexicographic sweep through the fields with GS-Lex. Updated cells are colored green, old cells are red. **Right:** Grid distribution for Gauss-Seidel Red/Black. The black points are calculated after all red points have been updated.

problem obviously lies in the slow decay of large-scale errors. Because of this it seems plausible to take a closer look at the possible advantages in the use of different (coarser and finer) grids.

## B.2. Multiple grids and inter-grid communication

As already mentioned, one of the main ideas for multigrid is the use of several grids $\Omega_h$ with different grid spacing $h$. It is, therefore, inevitable to define a set of *transfer operators* $(I)_{h2}^{h1}$ to transmit information from the grid $\Omega_{h1}$ to the grid $\Omega_{h2}$. While arbitrary grids could be chosen in theory, it is more practical both from a mathematical and numerical viewpoint to limit the choice to the so called *standard coarsening* $\Omega_{2h}$ with double mesh size in each direction as shown in figure B.3.
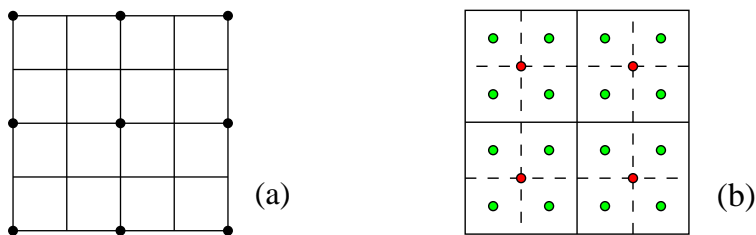


**Figure B.3.**: The choice of the coarsened grid: **(a)** Standard coarsening for vertex centered grids. The coarse grid $\Omega_{2h}$ is denoted by black points, the fine grid $\Omega_h$ by intersections. **(b)** Standard coarsening for cell centered grid. Red points correspond to $\Omega_{2h}$, green points to $\Omega_h$.

Most of the literature (e.g. [10] or [91]) mainly focus on vertex centered grids as shown in figure B.3 (a), while the adaptive mesh refinement formulation with flux conservation along cell interfaces suggests a cell centered potential (figure B.3 (b)). Only the staggered vector potential formulation (3.2.1) differs in the choice of placement, since each component of the vector potential is located on cell edges. Since this placement requires a huge number of complex special cases of control volumes for arbitrary refined grids, this case is not realized in *racoon III*.

The choice of the transfer operators has radical influence on the overall performance of the multigrid method. As a detailed discussion of all these aspects exceeds the focus of this thesis, I will just summarize the implemented methods.

## B.2.1. Prolongation

The *prolongation operator* for standard coarsening or *interpolation operator* $(I)_h^{2h} : \Omega_{2h} \mapsto \Omega_h$ maps coarse grid functions $u_{2h}$ to fine grid functions $u_h$. Two different prolongation operators were implemented, each with its own advantages and disadvantages.
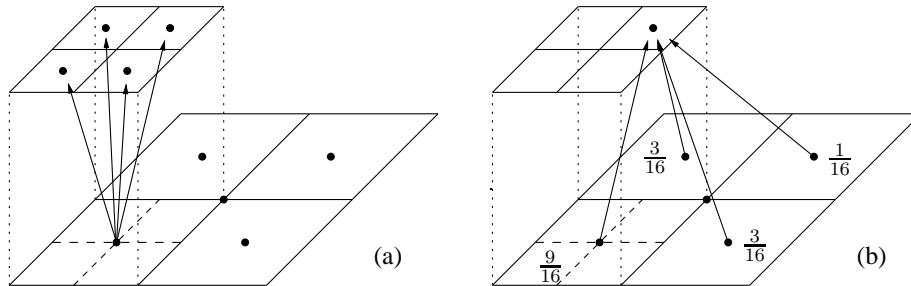


**Figure B.4.**: Two different prolongation operators for cell-centered grids: **(a)** Simple copy of the coarse grid value. **(b)** Linear interpolation: All four surrounding coarse grid values have influence on the fine cell.

**"Interpolation" by copying:** The easiest possible way to interpolate is just to copy the values from coarse to fine grid (see figure B.4 (a)). All four fine grid cells are set to the exact value of the corresponding coarse grid cell. This leads to the stencil:

$$(C)_h^{2h} = \left[ \begin{array}{cc} 0 & 0 \\ \boxed{1} & 0 \end{array} \right] \begin{array}{c} 2h \\ \\ h \end{array}$$

where the boxed field represents the $[s_{0,0}]$ position. While obviously this "interpolation" is of poor order (with a $1^{st}$ order error), it requires less

computational time and, more importantly, no expensive boundary transfers in a parallel environment. It should be noted, that the order of the intergrid interpolation has no consequence on the order of the solution, but just on the rate of convergence.

**Linear interpolation:** The second implemented stencil for prolongation reads

$$(L)_h^{2h} = \frac{1}{16} \begin{bmatrix} 3 & 1 \\ \boxed{9} & 3 \end{bmatrix}_h^{2h} .$$

It weighs the four surrounding coarse grid cells with respect to their proximity to the fine grid point. While exact up to second order it also requires diagonal communication when parallelized, which has a noticeable impact on the wall-clock performance.

For multiple reasons it is reasonable to employ higher order prolongation operators, which require larger stencils and even more communication, but provide more precise results. Though implemented and tested, they are not discussed here.

## B.2.2. Restriction

*Restriction operators* $(I)_{2h}^h$ map fine grid function $u_h$ on $\Omega_h$ to the coarse grid $\Omega_{2h}$. I will only commit myself to the straightforward choice of linear interpolation here. All surrounding fine grid values are weighed equally with $\frac{1}{4}$:

$$(F)_h^{2h} = \frac{1}{4} \begin{bmatrix} 1 & 1 \\ 1 & 1 \end{bmatrix}_{2h}^h .$$

This is a second order interpolation. While higher orders are implemented, they are not used in the context of multigrid in *racoon III*.

# B.3. Complete multigrid cycle

Now, as the tools are thoroughly laid out, it is time to finally merge them all into the complete multigrid algorithm. The ultimate aim is to solve the discrete Poisson equation on some square grid $\Omega_h$. The first step towards multigrid is the introduction of the *two grid cycle*:

- Choose an initial guess $u_h$ on $\Omega_h$. This choice is quite arbitrary and $u_h = 0$ works sufficiently well for Poisson-like problems. Preconditioning methods for finding better first approximations are not covered here.

- Relax $\nu_{\text{pre}}$ times on $\Omega_h$ (Pre-smoothing). Now, only large-scale components of the error should remain.

- Compute the residual $r_h = f_h - L_h u_h$ on $\Omega_h$.

- Restrict the residual to $\Omega_{2h}$: $r_{2h} = (I)_{2h}^h r_h$.

- Solve the defect equation (B.4) on $\Omega_{2h}$: $L_{2h} e_{2h} = r_{2h}$.

- Prolong the coarse grid error back to $\Omega_h$: $e_h = (I)_h^{2h} e_{2h}$.

- Correct the approximation $u_h$ on $\Omega_h$ with the error obtained above: $u_h^{n+1} = u_h^n + e_h$.

- Relax $\nu_{\text{post}}$ times on $\Omega_h$ (Post-smoothing).

All these points are well defined and outlined above, except one that may surprise: The original problem on $\Omega_h$ is reduced to a similar problem on $\Omega_{2h}$. This may at first seem futile and inconveniently self-referring. Of course, a problem on $\Omega_{2h}$ is simpler in a sense that it consists of less unknowns and, if solved accurately, works very well for the fine grid, since the oscillatory components of the error are eliminated by the relaxation.
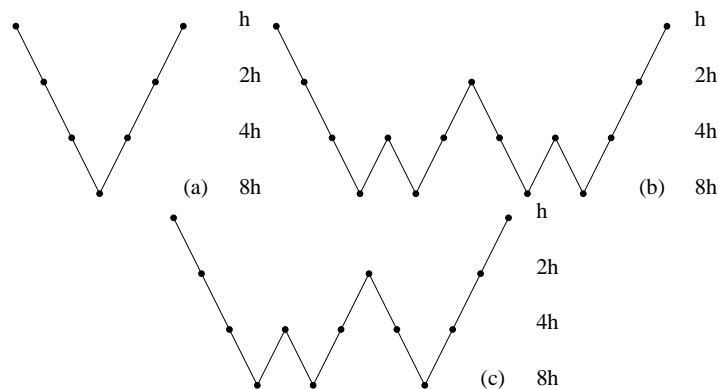


**Figure B.5.**: Multigrid cycles: **(a)** V-Cycle, **(b)** W-Cycle, **(c)** F-Cycle

The *complete multigrid cycle* is just one step ahead: As the coarse grid problem resembles the original problem, it can itself be solved by a two grid cycle. If this process is repeated on successively coarser grids $\Omega_{4h}$, $\Omega_{8h}$, etc., the whole problem reduces to a Poisson equation on a coarsest grid with ideally just one free grid point (or very few grid points, the amount depending on the grid structure and domain boundaries), where it can be solved exactly or by an adequate number of smoothing steps. This idea of recursively solving the original problem

on successively coarser grids, interpolating the correction back to the fine grids and then smoothing the error is the whole gist of multigrid.

The multigrid cycle presented above, for reasons apparent in figure B.5, is called *V-Cycle*. More complicated paths through the multiple grids, like the *W-Cycle* or *F-Cycle*, are not only imaginable but also reasonable, because the accuracy of the coarse grid approximation has a large effect on the finer grids.

The final choice of all components (Smoother, Pre- and Post-smoothing, Relaxation, Prolongation, Cycle type) has to be balanced under aspects like convergence rate, stability, computational effort and communication overhead.

# Bibliography

[1] W. T. Ashurst, A. R. Kerstein, R. M. Kerr, and C. H. Gibson. Alignment of vorticity and scalar gradient with strain rate in simulated Navier–Stokes turbulence. *Phys. Fluids*, 30:2343, 1987.

[2] G. K. Batchelor. *An Introduction to Fluid Dynamics*. Cambridge University Press, London, 1974.

[3] J. T. Beale, T. Kato, and A. Majda. Remarks on the breakdown of smooth solutions for the 3-D Euler equations. *Commun. Math. Phys.*, 94:61–66, 1984.

[4] J. B. Bell and D. L. Marcus. Vorticity intensification and transition to turbulence in three-dimensional Euler equations. *Commun. Math. Phys.*, 147:371–394, 1992.

[5] J. B. Bell, P. Colella, and H. M. Glaz. A second order projection method for the incompressible Navier-Stokes equations. *Jour. Comp. Phys.*, 85: 257–283, 1989.

[6] O. N. Boratav and R. B. Pelz. Direct numerical simulation of transition to turbulence from a high-symmetry initial condition. *Phys. Fluids*, 6(8): 2757–2784, March 1994.

[7] O. N. Boratav and R. B. Pelz. Evidence for a real-time singularity in hydrodynamics from time series analysis. *Phys. Rev. Lett.*, 79:4998–5001, 1994.

[8] M. E. Brachet, D. I. Meiron, S. A. Orszag, B. G. Nickel, R. H. Morf, and U. Frisch. Small-scale structure of the Taylor-Green vortex. *J. Fluid Mech.*, 130:411–452, 1983.

[9] M. E. Brachet, M. Meneguzzi, A. Vincent, H. Politano, and P. L. Sulem. Numerical evidence of smooth self-similar dynamics and possibility of subsequent collapse for three-dimensional ideal flows. *Phys. Fluids*, 4(12): 2845–2854, 1992.

[10] W. L. Briggs, Van Emden Henson, and S. F. McCormick. *A Multigrid Tutorial, Second Edition*. Siam, 2000.

[11] M. D. Bustamante and M. Brachet. On the interplay between the BKM theorem and the analyticity-strip method to investigate numerically the incompressible Euler singularity problem. Published online, `http://arxiv.org/abs/1112.1571`, 2011.

[12] L. Caffarelli, R. Kohn, and L. Nirenberg. Partial regularity of suitable weak solutions of the Navier-Stokes equations. *Comm. Appl. Math.*, 35:771–831, 1982.

[13] D. Chae. Nonexistence of self-similar singularities for the 3D incompressible Euler equations. *Commun. Math. Phys.*, 273:203–215, 2007.

[14] D. Chae and R. Shvydkoy. On formation of a locally self-similar collapse in the incompressible Euler equations. 2012. Published online: `http://homepages.math.uic.edu/~shvydkoy/publications.html`.

[15] A. Cheskidov, P. Constantin, S. Friedlander, and R. Shvydkoy. Energy conservation and Onsager's conjecture for the Euler equations. *Nonlinearity*, 21(6):1233, 2008.

[16] L. Chevillard and C. Meneveau. Lagrangian time correlations of vorticity alignments in isotropic turbulence: Observations and model predictions. *Phys. Fluids*, 23, 2011.

[17] A. J. Chorin. The numerical solution of the Navier-Stokes equations for an incompressible fluid. *Bull. Amer. Math. Soc.*, 73:928–931, 1967.

[18] A. J. Chorin. On the convergence of discrete approximations for the Navier-Stokes equations. *Math. Comput.*, 23:341–353, 1969.

[19] A. J. Chorin. Estimates of intermittency, spectra, and blow-up in developed turbulence. *Communications on Pure and Applied Mathematics*, 34(6):853–866, 1981.

[20] A. J. Chorin. The evolution of a turbulent vortex. *Commun. Math. Phys.*, 83:517–535, 1982.

[21] A. J. Chorin and J. E. Marsden. *A Mathematical Introduction to Fluid Mechanics.* Springer-Verlag Publishing Company, Inc., New York, 1993.

[22] C. Cichowlas and M. Brachet. Evolution of complex singularities in Kida-Pelz and Taylor-Green inviscid flows. *Fluid Dyn. Research*, 36:239–248, 2005.

[23] P. Constantin. Geometric statistics in turbulence. *SIAM Rev.*, 36, 1994.

[24] P. Constantin. An Eulerian-Lagrangian approach for incompressible fluids: local theory. *J. Amer. Math. Soc.*, 15(2):263–278, 2000.

[25] P. Constantin. On the Euler equations of incompressible fluids. *Bulletin Amer. Math. Soc.*, 44(4):603–621, 2007.

[26] P. Constantin and C. Foias. *Navier-Stokes Equations*. The University of Chicago Press, Chicago and London, 1988.

[27] P. Constantin, W. E, and E. S. Titi. Onsager's conjecture on the energy conservation for solutions of Euler's equation. *Commun. Math. Phys.*, 165: 207–209, 1994.

[28] P. Constantin, C. Fefferman, and A. Majda. Geometric constraints on potentially singular solutions for the 3D Euler equations. *Commun. Part. Diff. Eq.*, 21:559–571, 1996.

[29] D. Cordoba and C. Fefferman. On the collapse of tubes carried by 3D incompressible flows. *Commun. Math. Phys.*, 222:293–298, 2001.

[30] J. Deng, T. Y. Hou, and X. Yu. Geometric properties and nonblowup of 3D incompressible Euler flow. *Commun. Part. Diff. Eq.*, 30(1-2):225–243, 2005.

[31] J. Deng, T. Y. Hou, and X. Yu. Improved geometric conditions for non-blowup of the 3D incompressible Euler equation. *Commun. Part. Diff. Eq.*, 31(2):293–306, 2006.

[32] C. R. Doering. The 3D Navier-Stokes problem. *Annual Review of Fluid Mechanics*, 41:109–128, 2009.

[33] J. Dreher and R. Grauer. Racoon: A parallel mesh-adaptive framework for hyperbolic conservation laws. *Parallel Computing*, pages 913–932, 2005.

[34] D. G. Ebin and J. Marsden. Groups of diffeomorphisms and the motion of an incompressible fluid. *The Annals of Mathematics*, 92(1):102–163, 1970.

[35] C. Fefferman. Existence and smoothness of the Navier-Stokes equation. Published online:
`http://www.claymath.org/millennium/Navier-Stokes_Equations/navierstokes.pdf`, 2000.

[36] U. Frisch. *Turbulence*. Cambridge University Press, Cambridge, 1995.

[37] U. Frisch, T. Matsumoto, and J. Bec. Singularities of Euler flow? Not out of the blue! *J. Stat. Phys.*, 113:761–781, 2003.

[38] J. D. Gibbon. A quaternionic structure in the three-dimensional Euler and ideal magneto-hydrodynamics equation. *Physica D: Nonlinear Phenomena*, 166(17), 2002.

[39] J. D. Gibbon. The three-dimensional Euler equations: Where do we stand? *Physica D: Nonlinear Phenomena*, 237:1894–1904, 2008.

[40] J. D. Gibbon, D. D. Holm, R. M. Kerr, and I. Roulstone. Quaternions and particle dynamics in Euler fluid flow. *Nonlinearity*, 19(1969), 2006.

[41] T. Grafke, H. Homann, J. Dreher, and R. Grauer. Numercial simulations of possible finite time singularities in the incompressible Euler equations: comparison of numerical methods. *Physica D: Nonlinear Phenomena*, 237: 1932–1936, 2008.

[42] R. Grauer, 2011. private communication.

[43] R. Grauer, C. Marliani, and K. Germaschewski. Adaptive mesh refinement for singular solutions of the incompressible Euler equations. *Physical Review Letters*, 80(19):4177–4180, 1999.

[44] J. M. Greene and R. B. Pelz. Stability of postulated, self-similar, hydrodynamic blowup solutions. *Phys. Review E*, 62(6), 2000.

[45] P. E. Hamlington, J. Schumacher, and W. J. A. Dahm. Direct assessment of vorticity alignment with local and nonlocal strain rates in turbulent flows. *Phys. Fluids*, 20, 2011.

[46] F. H. Harlow and J. E. Welch. Numerical calculation of time-dependent viscous incompressible flow of fluid with free surface. *Phys. Fluids*, 8(12), 1965.

[47] T. Y. Hou and R. Li. Dynamic depletion of vortex stretching and non-blowup of the 3-D incompressible Euler equations. *Journal of Nonlinear Science*, 16:639–664, 2006.

[48] T. Y. Hou and R. Li. Nonexistence of locally self-similar blow-up for the 3D incompressible Navier-Stokes equations. *Discrete and Continuous Dynamical Systems*, 18(4):637–642, 2007.

[49] V. I. Judovič. Non-stationary flows of an ideal incompressible fluid. *Vyčisl. Mat. i Fiz.*, 3:1032–1066, 1963. [Russian].

[50] T. Kato. On classical solutions of the two-dimensional non-stationary Euler equation. *Archive for Rational Mechanics and Analysis*, 25:188–200, 1967.

[51] T. Kato. Non-stationary flows of viscous and ideal fluids in $\mathbb{R}^3$. *J. Functional Analysis*, 9:296–305, 1972.

[52] R. M. Kerr. Evidence for a singularity of the three-dimensional, incompressible Euler equations. *Phys. Fluids A*, 5(7):1725–1746, July 1993.

[53] R. M. Kerr. Euler singularities and turbulence. In T. Tatsumi, E. Watanabe, and T. Kambe, editors, *19th ICTAM Kyoto '96*, pages 57–70, 1997.

[54] R. M. Kerr. *Fundamental problematic issues in turbulence*, chapter The outer regions of singular Euler. Birkhäuser, 1999.

[55] R. M. Kerr. Velocity and scaling of collapsing Euler vortices. *Phys. Fluids*, 17, 2005.

[56] R. M. Kerr. Computational Euler history. Published online, `http://arxiv.org/abs/physics/0607148`, 2006.

[57] R. M. Kerr, 2012. private communication.

[58] R. M. Kerr and F. Hussain. Simulation of vortex reconnection. *Physica D: Nonlinear Phenomena*, 37:474, 1989.

[59] S. Kida. Three-dimensional periodic flows with high symmetry. *J. Phys. Soc. Jpn.*, 54:2132–2136, 1985.

[60] S. Kida and Y. Murakami. Kolmogorov's spectrum in a freely decaying turbulence. *J. Phys. Soc. Jpn.*, 55, 1986.

[61] S. Kida and Y. Murakami. Kolmogorov similarity in freely decaying turbulence. *Phys. Fluids*, 30, 1987.

[62] Y. Kimura. Self-similar collapse of a 3D straight vortex filament model. *Geophysical and Astrophysical Fluid Dynamics*, 103(2-3):135–142, 2009.

[63] Y. Kimura. Self-similar collapse of 2D and 3D vortex filament models. *Theoretical and Computational Fluid Dynamics*, 24(1–4):389–394, 2010.

[64] A. N. Kolmogorov. Local structure of turbulence in an incompressible fluid at very high Reynolds numbers. *Dokl. Akad. Nauk SSSR*, 30:299–303, 1941.

[65] A. N. Kolmogorov. Energy dissipation in locally isotropic turbulence. *Dokl. Akad. Nauk SSSR*, 32:19–21, 1941.

[66] A. N. Kolmogorov. A refinement of previous hypotheses concerning the local structure of turbulence in a viscous incompressible fluid at high Reynolds numbers. *J. Fluid Mech.*, 13:82–85, 1962.

[67] A. Kurganov and D. Levy. A third-order semidiscrete central scheme for conservation laws and convection-diffusion equation. *Jour. Sci. Comp.*, 22 (4):1461–1488, 2000.

[68] A. Kurganov and E. Tadmor. New high-resolution central schemes for nonlinear conservation laws and convection-diffusion equations. *Jour. Comp. Phys.*, 160:241–282, 2000.

[69] O. A. Ladyzhenskaya. Sixth problem of the millenium: Navier-Stokes equations, existence and smoothness. *Russian Math. Surveys*, 58:251–286, 2001.

[70] H. Lamb. *Hydrodynamics*. Cambridge University Press, 1932.

[71] J. Leray. Sur le mouvement d'un liquide visqeux emplissant l'espace. *Acta Math.*, 63:193–248, 1934.

[72] A. J. Majda and A. L. Bertozzi. *Vorticity and Incompressible Flow*. Cambridge University Press, New York, 2002.

[73] M. V. Melander and F. Hussain. Cross-linking of two antiparallel vortex tubes. *Phys. Fluids A*, 1:633, 1989.

[74] C. Meneveau. Lagrangian dynamics and models of the velocity gradient tensor in turbulent flows. *Annual Review of Fluid Mechanics*, 43:219–245, 2011.

[75] M. Minion. A projection method for locally refined grids. *Jour. Comp. Phys.*, 127:158–178, 1996.

[76] R. H. Morf, S. A. Orszag, and U. Frisch. Spontaneous singularity in three-dimensional, inviscid, incompressible flow. *Physical Review Letters*, 44(9): 572–575, March 1980.

[77] J. Nečas, M. Ružička, and V. Šverák. On Leray's self-similar solutions of the Navier-Stokes equations. *Acta Math.*, 176:283–294, 1996.

[78] C. S. Ng and A. Bhattacharjee. Sufficient condition for a finite-time singularity in a high-symmetry Euler flow: Analysis and statistics. *Phys. Rev. E*, 54:1530–1534, Aug 1996.

[79] L. Onsager. Statistical hydrodynamics. *Nuovo Cimento (Supplemento)*, 6: 279–287, 1949.

[80] P. Orlandi and G. F. Carnevale. Nonlinear amplification of vorticity in inviscid interaction of orthogonal Lamb dipoles. *Phys. Fluids*, 19, 2007.

[81] R. B. Pelz. Locally self-similar, finite-time collapse in a high-symmetry vortex filament model. *Phys. Rev. E*, 55:1617–1626, 1997.

[82] R. B. Pelz. Symmetry and the hydrodynamic blow-up problem. *J. Fluid Mech.*, 444:299–320, January 2001.

[83] R. B. Pelz. Extended series analysis of full octahedral flow: numerical evidence for hydrodynamic blowup. *Fluid Dyn. Research*, 33:207–221, 2003.

[84] Y. Pomeaua and D. Sciamarella. An unfinished tale of nonlinear PDEs: Do solutions of 3D incompressible Euler equations blow-up in finite time? *Physica D: Nonlinear Phenomena*, 205:215–221, 2005.

[85] G. Ponce. Remarks on a paper by J. T. Beale, T. Kato and A. Majda. *Commun. Math. Phys.*, 98:349–353, 1985.

[86] A. Pumir and E. Siggia. Collapsing solutions to the 3-D Euler equations. *Phys. Fluids A*, 2(2):220–241, February 1990.

[87] Z. She and E. Lévêque. Universal scaling laws in fully developed turbulence. *Physical Review Letters*, 72(3):336–339, January 1994.

[88] C. Shu and S. Osher. Efficient implementation of essentially non-oscillatory shock-capturing schemes. *Journal of Computational Physics*, 77:439–471, 1988.

[89] E. D. Siggia. Collapse and amplification of a vortex filament. *Phys. Fluids*, 28:794–805, 1985.

[90] G. I. Taylor and A. E. Green. Mechanism of the production of small eddies from large ones. *Proc. R. Soc. Lond. A*, 158:499–521, 1937.

[91] U. Trottenberg, C. Oosterlee, and A. Schueller. *Multigrid*. Academic Press, London, 2001.

[92] T.-P. Tsai. On Leray's self-similar solutions of the Navier-Stokes equations satisfying local energy estimates. *Arch. Rat. Mech. Anal.*, 143(1):29–51, 1998.

[93] J.-Z. Wu, H.-Y. Ma, and M.-D. Zhou. *Vorticity and Vortex Dynamics*. Springer, 2006.